ELEVATED TEMPERATURE DEFORMATION OF TD-NICKEL BASE ALLOYS

by

J. J. Petrovic, R. D. Kane and L. J. Ebert

ANNUAL STATUS REPORT
August 1972

Prepared for

NATIONAL AERONAUTICS AND SPACE ADMINISTRATION

Grant NGR 36-003-094

School of Engineering
Division of Metallurgy and Materials Science
Case Western Reserve University
Cleveland, Ohio

ELEVATED TEMPERATURE DEFORMATION OF TD-NICKEL BASE ALLOYS

NGR 36-003-094

Annual Status Report
August 1972

Prepared by J.J. Petrovic, R.D. Kane
and L.J. Ebert

Submitted to:

Office of Grants and Research Grants

Attention Code SC

National Aeronautics and Space Administration
Washington, D.C. 20546

School of Engineering
Division of Metallurgy and Materials Science
Case Western Reserve University
Cleveland, Ohio

ELEVATED TEMPERATURE DEFORMATION OF TD-NICKEL BASE ALLOYS

Abstract

Sensitivity of the elevated temperature (above 1/2 T_m) deformation of TD-nickel to grain size and shape was examined in both tension and creep. Elevated temperature strength increased with increasing grain diameter and increasing L/D ratio. Measured activation enthalpies in tension and creep were not the same. In tension, the internal stress was not proportional to the shear modulus. Creep activation enthalpies increased with increasing L/D ratio and increasing grain diameter, to high values compared with that of the self diffusion enthalpy.

It has been postulated that two concurrent processes contribute to the elevated temperature deformation of polycrystalline TD-nickel: diffusion controlled grain boundary sliding, and dislocation motion. The contribution of dislocation motion increases with increasing L/D ratio and increasing grain diameter. Dislocation motion is strongly influenced by dislocation-dispersed particle interactions arising from surface tension effects. The high apparent activation enthalpies and stress sensitivities observed in TD-nickel are a result of these dislocation-particle interactions.

The deformation and annealing response of TD-Nickel-Chromium (TD-NiCr) was examined. TD-NiCr 0.1 inch thick sheet was longitudinally and transversely rolled in both the as-received unannealed and annealed conditions. Grain size was found to decrease with increased rolling strain and increasing annealing temperature for all material states tested.

High temperature tensile tests between 1100°F and 2000°F were

conducted on TD-NiCr of various grains sizes in the range 0.0037 mm to 0.0515 mm. Yield and tensile strength was found to decrease with increasing temperature and decreasing grain size. Ductility as measured by percent elongation was shown to be very dependent on grain size especially between 1500°F and 2000°F. Ductility increased dramatically with decreasing grain size over this temperature range.

Limited investigations were conducted by division undergraduates in the areas of intermediate temperature stress-rupture of TD-Nickel and texture determinations of TD-Nickel and TD-NiCr. Stress-rupture properties of TD-Nickel were determined at 1089°K (1500°F) as a function of grain size. The textures of TD-Nickel bar material and TD-NiCr sheet were also determined as a function of grain size and of the deformation and annealing treatments used to produce the various grain sizes.

TABLE OF CONTENTS

LIST OF FIGURES

LIST OF TABLES

SECTION I

ELEVATED TEMPERATURE DEFORMATION OF TD-NICKEL

by John Joseph Petrovic

Submitted in partial fulfillment of the
requirements for the Degree of Doctor of Philosophy

Thesis Advisor: Dr. L.J. Ebert

INTRODUCTION

A. Foreword

Dispersion hardened materials were developed in order to meet the increasing demands of elevated temperature applications. Of this genus of materials, TD-nickel, which contains thorium dioxide (ThO_2) particles as the inert dispersed second phase in a nickel matrix, is among the most well-known. The dispersion in this material is produced mechanically by powder metallurgy techniques, and suitable thermo-mechanical working operations. Fabricated sub-structures are produced which are stable above 0.9 of the absolute melting temperature of the matrix. This substructural stability is a contributing factor to the excellent elevated temperature mechanical properties of TD-nickel, which has useful engineering characteristics as high as 1589°K (2400°F).

While extensive effort has been directed towards the development and refinement of fabrication techniques for TD-nickel, relatively few investigations have been concerned with determination of the basic factors which produce and control the

elevated temperature mechanical properties of this material. As a result, these factors have not been well understood.

B. Literature Survey

The literature is best reviewed by a discussion of two general topics : 1) properties of TD-nickel; 2) deformation theories for dispersion hardened materials. All investigations to be cited are concerned with behavior above one-half the absolute melting temperature of the material.

1. Properties of TD-nickel

a. Tensile Properties

Elevated temperature tensile strength levels in TD-nickel have been found to be sensitive to the following factors: 1) grain size, 2) grain shape, and 3) nature of the thoria particle dispersion. The yield strength increases with increasing grain size (1,2)*, increasing grain elongation (1,2,3), and increasing volume fraction of the dispersed phase (3). Effects of grain shape have been restricted

*Numbers in parentheses indicate references listed in the Bibliography, Section VI.

to shapes of roughly ellipsoidal geometry, with the shape index being the Length-to-Diameter, or L/D, ratio. Strength is reported to increase linearly (2,3) with increasing L/D ratio, until it becomes independent of L/D ratio at high values of this quantity (3).

Fraser and Evans (3) noted that the elevated temperature tensile strength increased with increasing volume fraction of dispersed phase. A dependence on $f^{\frac{1}{2}}$, where f = volume fraction, was found. No examination has been made of the effect of particle radius, R_o, on elevated temperature strength levels.

Ductility varies inversely as strength with respect to changes in grain size and shape. Equiaxed, fine grained material (L/D = 1, 0.001 mm average grain diameter) possesses maximum ductility, but minimum strength. Generally, the ductility decreases with increasing grain size and L/D ratio. For all ranges of grain size and shape, both ductility and strength increase with increasing tensile strain rate (1).

Anisotropy of both strength and ductility results from the elongated grain structures in TD-nickel (1). Strength levels decrease and ductility increases as

the test direction departs from the direction of grain elongation. An exception to this behavior occurs in extremely large grained material (0.5 mm average grain diameter, L/D ≃ 3), where strength and ductility are both maximum for tests parallel to the grain elongation.

Activation enthalpy measurements made in tensile tests on TD-nickel have generally yielded high values as compared to the self-diffusion enthalpy (4) of nickel (3 ev). Doble (1) obtained values of 7-14 ev at 1366°K (2000°F) for a wide range of grain sizes and shapes. No distinct trends in the activation enthalpy with grain size and shape were discernible. Lasalmonie and Sindzingre (5) found the activation enthalpy to increase abruptly with temperature, from values near 3 ev below 1023°K (1382°F) to a value of 12 ev at 1073°K (1472°F). There was no indication that the measured activation enthalpy would level off at higher temperatures.

b. Creep Properties

TD-nickel exhibits creep behavior of the classic kind. Creep begins with a primary stage of decreasing creep rate, followed by a steady state region of constant creep rate. Tertiary creep occurs only to a

limited extent in the material. The steady state creep rate increases with increasing stress and temperature. Total creep elongation usually increases with increasing stress and temperature, but its dependence on these variables is not as rigid as that of the steady state creep rate.

The creep behavior of TD-nickel is influenced markedly by grain structure variables (i.e. grain size and shape). In an examination of 1.27 cm (½ inch) commercial bar (0.001 mm average grain diameter, L/D = 15-20), Wilcox and Clauer (6) found the steady state creep rate to be of the form:

$$\dot{\varepsilon}_s = A \sigma^N e^{-Q/kT} \qquad (1)$$

where $\dot{\varepsilon}_s$ = uniaxial strain rate, A = a constant, σ = uniaxial true stress, N = stress exponent, Q = activation enthalpy, k = Boltzman constant, and T = absolute temperature. The stress exponent N had a value of 40, and the activation enthalpy Q was 8.25 ev. The activation enthalpy was reported as stress independent, although measurements were made by changing the stress and temperature simultaneously, rather than varying stress at constant temperature. Effects

of L/D ratio on the stress exponent N were noted by Wilcox, Clauer and Hutchinson (2). N increased from a value of 6.7 at L/D = 2.9 to a value of 26.1 at L/D = 7.8.

In TD-nickel experimental alloys of larger grain size (∿0.05 mm average grain diameter) and equiaxed grain shape (L/D∿1), Clauer and Wilcox (7) observed the steady state creep rate to be described by:

$$\dot{\varepsilon}_s = \frac{A}{T} \sigma^N e^{-Q/kT} \qquad (2)$$

For these alloys, N had a value of 7 and Q a value of 2.78 ev. The alloys were of variable thoria particle radius and interparticle spacing. Both N and Q were independent of these parameters.

The creep behavior of TD-nickel is significantly different from that of pure nickel. The steady state creep rate of pure nickel is described by Equation 1. Reported values of N and Q range from 4.6 - 7.0 and 2.82 to 2.89 ev respectively (8-11). The creep activation enthalpy has been observed to be independent of grain size and stress. No high activation enthalpies or stress dependencies have been noted in pure nickel.

c. Deformation Substructures

The microstructures characteristic of elevated temperature deformation in TD-nickel show two phenomena: 1) grain boundary sliding, and 2) intergranular cracking. Evidences of grain boundary sliding have been reported by Doble (1) and Fraser and Evans (3) in tension, and Wilcox and Clauer (6) in creep. Intergranular cracking is seen in tension (1) and creep (6,12), and appears associated with the fracture mode. Intergranular cracks are observed at grain boundaries perpendicular to the applied stress.

Little substructural change occurs as a result of creep deformation. Wilcox and Clauer (6,7) have reported only small increases in dislocation density above that of the uncrept state. Dislocation tangles or cells are not formed to a large extent. The most prominent dislocation features noted have been grain boundary dislocation sources and parallel dislocation arrays. In both crept and uncrept substructures, individual dislocations are described as being "pinned" to thoria particles (6,7).

2. Deformation Theories for Dispersion Hardened Materials

a. Dislocation Models

Ansell and Weertman (13) were the first to

propose a dislocation model for steady state creep in a dispersion hardened material. Climb of dislocations over second phase particles is assumed to be the rate controlling process. At low stresses, the steady state creep rate is given by :

$$\dot{\gamma}_s = \frac{A\,\tau}{R_o^2}\, e^{-\Delta H_{SD}/kT} \qquad (3)$$

where $\dot{\gamma}_s$ = shear strain rate, A = a constant, τ = shear stress, R_o = particle radius, ΔH_{SD} = self diffusion enthalpy, k = Boltzman constant, and T = absolute temperature. In polycrystalline materials $\dot{\gamma}_s = \sqrt{2}\,\dot{\varepsilon}_s$ and $\tau = \sigma/2$, where $\dot{\varepsilon}_s$ and σ are the uniaxial strain rate and stress, respectively. At intermediate stresses, the derived creep rate expression is:

$$\dot{\gamma}_s = \frac{A\,\tau^4\,d^2}{R_o \mu^3\, T}\, e^{-\Delta H_{SD}/kT} \qquad (4)$$

where d = interparticle spacing and μ = shear modulus.

A dislocation climb model similar to that of Ansell and Weertman was suggested by Wilcox and Clauer (14). This model differs in that the density of mobile dislocations is assumed to be stress dependent. The expression obtained is:

$$\dot{\gamma}_s = \frac{A\,\tau^{*(\beta+1)}\,d^2}{R_o\, T}\, e^{-\Delta H_{SD}/kT} \qquad (5)$$

where β is a stress exponent describing the effect of stress on mobile dislocation density in the expression $\rho = \rho_o \tau^{\beta}$. τ^* is taken as the effective stress, that is, $\tau^* = \tau - \tau_i$, where τ_i is the internal stress affecting dislocation motion. Wilcox and Clauer deduced a value of 4 for β

The thermally activated dissolution of certain types of dislocation junction reactions, with subsequent slip of glide dislocations to produce creep strain, has been proposed by Guyot (15) to explain high activation enthalpies in dispersion hardened materials. This model, however, requires a rather specialized form of dislocation substructure which does not appear to develop to the extent required to be a significant factor in the total creep strain.

High activation enthalpies attributable to a dislocation mechanism might more reasonably be obtained following the arguments of Friedel (16). The thermally activated bypassing of dislocations past second phase particles by Orowan bowing was considered. This process has an activation enthalpy of the form:

$$\Delta H \simeq 2dL\{1 - \frac{\tau}{\tau_c}\}^{3/2} \qquad (6)$$

where ΔH = activation enthalpy, L = dislocation line tension, and τ_c = theoretical Orowan stress at $0^{\circ}K$. The activation enthalpy is highly stress dependent, and becomes prohibitively high unless $\tau \simeq \tau_c$ within about 1% for $d > 10^2 b$, where b is the dislocation Burgers vector. Thus, Friedel's model implies a very high internal stress. In addition, it is assumed that the dislocations cannot circumvent the particles by easier means, such as dislocation climb, which should occur readily at elevated temperatures.

Lagneborg (17) has examined the steady state creep of dispersion hardened materials from the strain hardening - recovery balance viewpoint. In this approach, steady state creep commences when the rates of strain hardening and recovery become equal. The rate controlling process is considered to be that of recovery. Lagneborg assumes that the presence of the dispersed phase reduces the recovery rate by impeding the growth of dislocation networks. After Hillert (18), a retarding force $\tau \cdot Z$ is postulated, where Z depends on the size and distribution of the dispersed phase. This leads to an expression for the creep rate of:

$$\dot{\gamma} = A\tau^3\left\{\frac{\tau}{\alpha\mu b} - Z\right\}^2 \qquad (7)$$

where α = a constant. No suggestion was given as to the exact manner in which the dispersed phase might produce a dislocation retarding force. For a recovery process, the retarding force would be expected to influence dislocation climb.

Tien et. al. (19) have proposed that the high activation enthalpies observed in dispersion hardened materials may be associated with interstitial (rather than vacancy) formation and migration as the rate controlling factors in a dislocation creep process. In their model, jogs on screw dislocations are assumed to move by the thermally activated absorption or emission of interstitials. This is predicted to occur when the density of jogs is high, so that jog motion will quickly exhaust the local vacancy concentration. The interstitial mechanism controls when the dislocation network structure is "fine mesh" (this is assumed to be the case for dispersion hardened materials). Tien et. al. predict that when the dislocation network is "coarse mesh", dislocation creep will revert to vacancy controlled mechanisms, and activation enthalpies will be lower. No explanation is given as to why second phase particles should promote a "fine mesh" dislocation network.

b. Grain Boundary Sliding Models

Fraser and Evans (3) were the first to propose a model for dispersion hardened materials incorporating grain boundary effects. Their "fiber composite" model considers each grain as a fiber strengthened by the dispersed phase. Loads must be transferred across the grain boundaries. Thus, the total strength of the "composite" depends on both the inherent strength of each grain and the strength of the grain boundaries. If the grain boundaries are stronger than the grains (i.e. at temperatures below the "equi-cohesive" point), then the inherent grain strength will control the total strength. However, if the grains are stronger than the grain boundaries (i.e. at temperatures above the "equi-cohesive" point), grain boundary effects will determine the total strength.

Introduction of the second phase into the grain matrix increases its load carrying ability with respect to that of the grain boundary surface area, because of the hindrance of dislocation motion. The material will tend to deform by grain boundary sliding unless the grain boundary surface area is increased to the extent that its load carrying ability is greater than that of the grain interior. Fraser and Evans propose that this

can be achieved by producing a highly elongated, "fibrous" grain shape. By this means (i.e. increasing the grain elongation), they predict that the strength of the "composite" will be increased, with the upper limit being the inherent strength of the dispersion hardened grain interior.

A theoretical description of grain boundary sliding with diffusional accommodation has been developed by Raj and Ashby (20). This type of deformation might be expected to occur at high temperatures (above the "equi-cohesive" point) and low stresses. The shape of the grain boundary sliding path is assumed to control the sliding process, by dictating the conditions under which accommodative diffusion must occur to preserve integrity in the material. Using a continuum mechanics approach, the expression for the creep rate in a polycrystalline material of equiaxed grain shape is:

$$\dot{\gamma}_s = \frac{A\tau}{g^2 T} e^{-\Delta H_{SD}/kT} \qquad (8)$$

where g = grain diameter. Equation 8 applies when volume diffusion is predominant. When grain boundary diffusion is predominant, the grain size dependence becomes cubic

and ΔH_{SD} is replaced by the activation enthalpy for grain boundary diffusion.

Effects of grain shape on the sliding process were examined. For L/D ratios much greater than 1 (elongated grains), the creep rate is proportional to $(L/D)^{-1}$ for volume diffusion controlling, and proportional to $(L/D)^{-\frac{1}{2}}$ for boundary diffusion controlling.

The influence of a dispersed second phase was also considered. The presence of such particles is predicted to reduce the grain boundary sliding rate only slightly, with large particles more effective inhibitors than the same volume fraction of smaller particles. However, Ashby has postulated (21) that the presence of second phase particles at the grain boundary may restrict the ability of the boundary to emit or absorb vacancies (Equation 8 assumes that the boundaries are perfect sources or sinks for vacancies). This effect can lead to the introduction of a threshold stress, below which no grain boundary sliding will occur.

C. Purpose of the Present Investigation

No theoretical description of the elevated tempera-

ture behavior of dispersion hardened materials, which is of suitable generality to explain the behavioral characteristics of TD-nickel, is currently available. Dislocation models cannot account for the grain size and shape sensitivity which this material possesses. Grain boundary sliding models do not predict the role of the dispersed phase in the improvement of elevated temperature properties. Neither class of models can satisfactorily cope with the high activation enthalpies and stress sensitivities measured in TD-nickel.

The purpose of the present investigation was one of gaining an insight into the basic deformation mechanisms operative in TD-nickel--and in dispersion hardened materials in general--by examining the effects of grain size and shape variables on tensile and creep properties. The main focus was placed on the thermodynamic parameters describing the deformation process. Efforts were made to correlate thermodynamic measurements with substructural features observed by electron microscopy.

MATERIALS AND PROCEDURE

A. Material

TD-nickel as-extruded 7.62 cm (3 inch) bar supplied by the Fansteel Corporation was the starting material for the investigation. Its fabrication history is as follows: thoria containing nickel powder is compacted, sintered, and consolidated to 100% density by hot extrusion, with an 86% reduction in billet area at temperatures of 1255-1366°K (1800-2000°F). In the production of TD-nickel products, as-extruded material represents a state of minimal fabrication processing.

Two different lots of as-extruded bar (both fabricated by the same procedure) were used in the investigation. The lots were coded as #3014 and #3555. Both lots were similar in chemical composition. The vendor's chemical analysis of Lot 3555 is given in Table 1.

Grains in the as-extruded material were equiaxed, with an average grain diameter of approximately 0.001 mm. For 0.89-1.02 cm (0.35-0.40 inch) TD-nickel as-extruded bar produced by the Fansteel Corporation, Wilcox

et. al. (2) have measured values of 100 x 10^{-10} M for the average thoria particle radius and 1505 x 10^{-10} M for the interparticle spacing.

B. Grain Size and Shape Control

Grain size and shape were systematically controlled by following guidelines for thermomechanical processing established in a previous investigation (22,23). Material from TD-nickel Lot 3014 was used exclusively for the production of different grain sizes. Only material from Lot 3555 was used for grain shape control. Grain size was varied at constant grain shape (equiaxed, L/D $\sim$ 1) as far as possible, while grain shape was varied at constant grain size ($\sim$0.001 mm average grain diameter).

1. Grain Size Control

The grain size of the as-extruded bar was employed as a small grain size ($\sim$0.001 mm average grain diameter, L/D$\sim$1). This as-extruded material was given a standardization anneal for one hour at 1589°K (2400°F) in argon in order to match the annealing conditions of other grain sizes. The anneal had no apparent effect on as-extruded grain size or shape.

A large grain size ($\sim$0.4 mm average grain diameter,

L/D$\sim$3) was produced from the as-extruded state by cold rolling transversely to the extrusion axis (transverse rolling) and annealing. The rolling reduction was 33% in thickness, with an 11% reduction per pass. Splitting of the rolling slab (i.e. "alligatoring") occurred for reductions in thickness greater than 33%. Rolled samples were annealed for one hour at 1589°K (2400°F) in argon. Lower annealing temperatures resulted in material which was not fully large grained. This procedure produced material whose volume was 100% large grained. Development of these large grains was the result of abnormal grain growth (22,23).

A previous investigation (22,23) had suggested that an intermediate grain size could be produced by deformation and annealing, if the starting material was large grained. This proved to be true. The 100% large grained material was cold rolled to a 70% reduction in thickness at a 10% reduction per pass. The rolling direction was the same as used in the production of the large grained state (transverse to the original as-extruded axis). For this rolling operation, no slab splitting problems were encountered. Following rolling, samples were annealed for one hour

at 1366°K (2000°F) in vacuum to produce an intermediate grain size (∿0.02 mm average grain diameter, L/D∿1), and then for one hour at 1589°K (2400°F) in argon.

The intermediate grain size was established after the 1366°K (2000°F) anneal. This anneal was employed in order to rapidly heat rolled samples to temperature (by room temperature insertion into the hot zone). Slower heat-up rates promoted the formation of a recovered structure, rather than a distinct intermediate grain structure (no effect of heat-up rate was noted in the production of the large grain size). The final 1589°K (2400°F) anneal was employed for standardization purposes, and samples were heated with the furnace. This higher temperature anneal had no influence on the intermediate grain size produced by the 1366°K (2000°F) anneal.

2. Grain Shape Control

Grain shape control was achieved by swaging and annealing operations. Swaging changes an equiaxed grain shape to one which is approximately that of an ellipsoid. Thus, the grains increase in length and decrease in width with increasing swaging reductions (i.e. they become elongated). Results of a previous

investigation (22,23) indicated that Length-to-Diameter (L/D) ratio changes produced on swaging would not be significantly altered by subsequent annealing. Furthermore, the grain shape could be altered without large changes in grain size occurring on annealing.

As-extruded material was cold swaged (parallel to the extrusion axis) to reductions in area of 78% and 90%, using facilities at NASA*. Reductions were approximately 10% per swaging pass. All swaged samples were annealed for one hour at 1589°K (2400°F). A one hour anneal at 1589°K (2400°F) of the as-extruded state served as the equiaxed grain shape (L/D$\sim$1). The 78% swaging reduction produced an L/D ratio of about 5, while the L/D ratio after the 90% reduction was approximately 11. The grain size for all grain shape samples was approximately 0.001 mm. No intermediate annealing was done between swaging passes.

C. Metallography

In order to describe accurately the various grain sizes and shapes produced, it was necessary to employ

---

*Lewis Research Center, Cleveland, Ohio under the direction of Mr. Charles Blankenship

the methods of quantitative microscopy. This required adequate grain boundary delineation. No single grain boundary delineation technique was suitable for use over the wide range of grain sizes used in the investigation. For the intermediate (∿0.02 mm) and large (∿0.4mm) grain sizes, light optical methods were employed. Electron microscopy procedures were required for the small (∿0.001 mm) grain sizes.

Polishing and etching techniques for light optical microscopy were surveyed (24) to determine optimum procedures for grain boundary delineation in intermediate and large grained TD-nickel. Mechanical polishing by the standard abrasive methods was followed by electropolishing. Two electropolishes gave good results for TD-nickel. These were: 1) 35% H_2SO_4, 40% H_3PO_4, 25% H_2O at 5-6 volts; 2) 6 parts ethanol, 1 part H_2SO_4 at 20 volts.

Grain boundary etching of TD-nickel proved to be very difficult. Differences in etching behavior were noted as a function of sample orientation (with respect to the rolling direction), as well as of grain size. No chemical or electrochemical etchant surveyed was found suitable for etching both the intermediate

and large grain sizes. The intermediate grain size was particularly difficult to etch satisfactorily, as etchants which were suitable for the large grained condition did not give satisfactory results for the intermediate grain size.

Thermal etching gave grain boundary delineation adequate for quantitative measurements in both the intermediate and large grain sizes. Etching occurs as a result of grain boundary grooving, which resulted from surface tension effects. Specimens whose surfaces had been mechanically polished and electropolished were annealed for one hour at 1589^{o}K (2400^{o}F) in a vacuum of 0.133 N M^{-2}(10^{-3}torr) to produce the thermal etch. Thermal etching did not exhibit sensitivity to orientation or grain size, nor did it appear to alter the innate grain size.

Transmission electron microscopy was used to delineate small grain structures. Scanning electron microscopy for this purpose was not suitable, because of etching difficulties and limited contrast in the scanning microscope. Thin foils for transmission were prepared by the jet-dimple technique (25). The electropolish used in most cases for both stages of the of the procedure was 35% H_2SO_4, 40% H_3PO_4, 25% H_2O at

5-6 volts. Some conditions of material were prone toward severe pitting, and for these cases the 6 parts ethanol, 1 part H_2SO_4 electropolish (20 volts) was best for minimizing the pitting problem.

D. Quantitative Grain Structure Measurements

By measurements of L, the linear grain dimension, in three orthogonal directions, it was possible to estimate an average grain diameter, as well as determine L/D ratios (25). The grain dimension L is the inverse of N_L, the number of grain boundary intersections per unit length of a traverse line.

For rolled specimens, the orthogonal measurement directions were the following: 1) Direction 1 - rolling direction; 2) Direction 2 - transverse direction; 3) Direction 3 - thickness direction. Measurement directions in swaged specimens were: 1) Direction 1 - swaging direction; 2) Direction 2 - perpendicular to swaging direction; 3) Direction 3 - perpendicular to swaging direction and Direction 2. The measurement directions for those specimens which did not receive mechanical working were the same as for their mechanically worked counterparts.

In most cases, an average value for the linear

grain dimension ($\bar{L}$) was obtained as a result of 30 or more sets of independent measurements. However, physical limitations with the transmission electron microscopy technique limited the number of measurements in the long direction of elongated small grains to under 10.

The average grain diameter was calculated from measurements using the following expression (25):

$$\bar{L}_{av} = 0.844(\bar{L}_1\bar{L}_2\bar{L}_3)^{1/3} \qquad (9)$$

where $\bar{L}_{av}$ = average grain diameter, $\bar{L}_1$, $\bar{L}_2$, $\bar{L}_3$ are average grain dimensions in the 1, 2 and 3 Directions, respectively. For grain shape specimens, the L/D ratio was defined as $2\bar{L}_1/(\bar{L}_2 + \bar{L}_3)$. The L/D ratio for rolled specimens was taken as $(\bar{L}_1 + \bar{L}_2)/2\bar{L}_3$.

Grain size and shape measurements for the various grain conditions used in the investigation are given in Table 2. Table 2 also introduces a condition code (A-F), which will be used from this point forward in identifying the various grain structures. The variability in values presented is for a 95% confidence level of the mean value.

The data in Table 2 show that grain size remains

constant for changes in L/D ratio (D,E,F). Grains are reasonably equiaxed for Types A and B, but tend to be somewhat elongated for Type C. Comparison of Types A and D indicates that the initial grain structures of the two lots of TD-nickel used in the investigation were nearly identical (Type A was from Lot 3014 and Type D from Lot 3555).

E. Elevated Temperature Tensile Tests

The various material conditions (A-F) were tested in tension in the temperature range 866°K (1100°F) ($0.5T_m$) to 1589°K (2400°F) ($0.92T_m$). Fabrication techniques required that a sheet specimen geometry be employed for grain size specimens (A,B,C), while a round specimen geometry be used for grain shape specimens (D,E,F). Specifications of the sheet and round specimen geometries are shown in Figures 1 and 2. Sharp radii of curvature at the specimen shoulders were employed in specimen design to insure that all deformation took place within a well-defined gage section.

For controlled grain size specimens, the test axis was parallel to the rolling direction (Direction 1 in Table 2). However, Type C specimens were also tested parallel to the transverse direction (Direction 2 in

Table 2). This became necessary when Type C specimens tested in the rolling direction exhibited brittle behavior. In further discussions, Type C-1 indicates C specimens tested in the rolling direction, while Type C-2 denotes specimens tested in the transverse direction. For grain shape control specimens, the test axis was the swaging direction (Direction 1 in Table 2).

Specimen grips used in the testing were made of TD-nickel, and suitably designed so that no grip deformation occurred on testing. Grips were oxidized to eliminate parting problems after testing.

The test apparatus was an Instron-Brew furnace combination. Temperature was maintained by resistance heating of a tantalum element, in a vacuum of 6.65×10^{-3} N M^{-2} (5×10^{-5} torr). Temperature control was $\pm 2.8^{\circ}K$ ($\pm 5^{\circ}F$). Specimen temperature was measured with an insulated Platinum-10% Rhodium thermocouple in contact with the specimen. Thermal expansion during heating was taken up by integral movement in the grips. The grips were also designed for universal joint alignment. Tensile tests were conducted at a cross-head speed of 0.0254 cm/minute (0.01 inch/minute). This gave an initial strain rate of 0.01/minute for the 2.54 cm (1 inch) gage length used.

Differential strain rate and temperature experiments, as well as stress relaxation studies, were made in tension to determine thermal activation parameters. Differential strain rate tests require the strain rate to be changed discontinuously at some point in the flow curve, and the resultant change in flow stress measured. The two strain rates used were 0.002/minute and 0.02/minute. Differential temperature tests were made by stopping and unloading the strained specimen, changing the temperature and equilibrating, and then reloading the specimen. The change in flow stress with temperature was then recorded. The temperature change used was 45°K (80°F). Stress relaxation tests were conducted by straining the specimen to a selected point in the flow curve, stopping the Instron cross-head movement, and recording the stress decay with time. The stress seemed to be fully relaxed after about five minutes.

F. Elevated Temperature Creep Tests

Specimens and grips used for tensile tests were also used in the creep investigation. Creep tests were performed on Satec Model LD creep units. Furnace-retort assemblies were used to run tests in an inert argon

atmosphere. All tests were conducted at 1255°K (1800°F), with a temperature control of $\pm$1.7 K ($\pm$3 F). Tests were made at constant stress by employing the lever arm modifications described by Fullman (26).

Specimen strain was measured by monitoring the motion of the load train with an LVDT, whose input drove a chart recorder. Maximum sensitivity of the strain measurement system was $\pm$0.000127 cm ($\pm$0.00005 inch).

Creep tests were conducted as a function of stress, with at least four stresses employed for each grain condition. Stress levels were determined as fractions of the yield stresses obtained in tension tests. Aside from the instantaneous strain on loading, the entire creep curve was measured.

Thermal activation parameters were examined through differential temperature and stress tests. In differential temperature tests, the temperature was changed as quickly as possible (keeping the stress constant by compensating for thermal expansion or contraction of the load train), and the change in creep rate measured. Maximum equilibration time after a temperature change was one-half hour. The maximum temperature change

employed was 45°K (80°F). Differential stress tests were made by instantaneously changing the applied load, and observing effects on the creep rate.

G. Electron Microscopy

Tensile test fracture surfaces were examined with the scanning electron microscope. High voltage transmission electron microscopy (650 KV) was used for grain structure determinations, as well as for the examination of deformation features produced by tensile and creep deformation.

RESULTS

A. Tensile

1. Tensile Test Data

Elevated temperature stress-strain curves at 1366°K (2000°F) for the various material Conditions (A-F) are presented in Figures 3 and 4. Yield stress (0.2% offset criterion), tensile stress, and per cent elongation values as a function of temperature are shown in Figures 5-10.

Yield stresses for all material conditions exhibited significant temperature dependencies. Yield stress increased with increasing grain diameter and increasing L/D ratio. The L/D ratio appeared to have more influence on strength levels than did the grain diameter. Conditions A and D, similar in grain diameter and L/D ratio, were also similar in strength level.

Ductility generally decreased with increasing grain diameter and increasing L/D ratio. Condition C-1 was brittle over nearly the entire temperature range of testing. Condition C-2, however, was even more ductile than Condition B. The ductilities of Conditions A and D

were somewhat different. This difference may be attributable to the different specimen geometries used. In most cases, increased ductility was noted at the lowest and highest testing temperatures employed.

Yield stress and per cent elongation at 1366°K (2000°F) are compared for the various material conditions in Figure 11. Small, elongated grains possessed the highest strength, while small, equiaxed grains had the greatest ductility. Figures 12 and 13 show that there was no positive correlation between strength and ductility trends at room temperature (298°K (77°F)) and elevated temperature (1366°K (2000°F)). Indeed, any correlation present appeared to be an inverse one. Effects of tensile strain rate on strength and ductility are shown in Figure 14 for Condition D. Both quantities increased with increasing strain rate. This trend was the same for all material conditions.

Attempts to correlate the yield stress to the grain size, according to the Hall-Petch relationship (27,28) are shown in Figure 15. The Hall-Petch relationship is:

$$\sigma = \sigma_o + kd^{-1/2} \qquad (10)$$

where σ = yield stress, σ_o = yield stress at infinite grain diameter, d = grain diameter, and k = a constant. If the Hall=Petch relationship is obeyed, a plot of ln σ versus ln d will be linear, with a slope of $-\frac{1}{2}$. Figure 15 shows that the Hall-Petch relationship does not describe the elevated temperature yield strength of TD-nickel, an observation also made by Wilcox et. al. (2). At room temperature, a value significantly smaller than $-\frac{1}{2}$ was obtained.

Wilcox et. al. (2) have suggested that the elevated temperature yield stress is a linear function of the L/D ratio. Figure 16 indicates a relationship to the L/D ratio (although the number of data points is limited). However, a potential functional relationship may not be linear.

2. Tensile Thermal Activation Parameter Measurements

The thermally activated deformation analysis of Conrad (29-31) was adopted for activation parameter measurements. The apparent activation enthalpy as measured in a tensile test is given by:

$$\Delta H = -kT^2 \left(\frac{\partial \ln \dot{\varepsilon}}{\partial \sigma}\right)_T \left(\frac{\partial \sigma^*}{\partial T}\right)_{\dot{\varepsilon}} \qquad (11)$$

where ΔH = activation enthalpy, k = Boltzman constant, T = absolute temperature, $\dot{\varepsilon}$ = uniaxial strain rate, σ = uniaxial stress, and σ^* = effective stress. Effective stress is defined by the following relationship:

$$\sigma = \sigma^* + \sigma_i \qquad (12)$$

where σ = applied stress and σ_i = internal stress. The internal stress σ_i is usually assumed proportional to the shear modulus (32). On this assumption, Equation 11 may be changed to the form:

$$\Delta H = -kT^2 \left(\frac{\partial \ln \dot{\varepsilon}}{\partial \sigma}\right)_T \left\{\left(\frac{\partial \sigma}{\partial T}\right)_{\dot{\varepsilon}} - \frac{\sigma_i}{\mu} \frac{d\mu}{dT}\right\} \qquad (13)$$

where μ = shear modulus. Values for the shear modulus of nickel as a function of temperature are given in Table 3 (33).

Values for $(\partial \ln \dot{\varepsilon}/\partial \sigma)_T$ were obtained from differential strain rate change tests. Complications arose from the occurrence of a strain rate change transient, as shown schematically in Figure 17. On the first low-to-high strain rate change upon loading of the specimen, a greater stress sensitivity was observed

than for subsequent changes. This was accompanied by an increase in stress level, suggesting that the internal structure of the specimen had been altered by the first strain rate change. Later unloading and reloading of the specimen caused the transient to reappear, although its relative magnitude (i.e. $\Delta\sigma_1/\Delta\sigma_2$ where 1 refers to the first strain rate change and 2 to the second) was smaller than that occurring on initial loading, indicating a possible reduction in the effect with increasing strain. The transient was absent if the first strain rate change on loading was from a high to low strain rate.

The relative magnitude of the transient decreased with decreasing temperature. At the lowest test temperature (866°K (1100°F), no transient was observed. At the highest test temperature (1589°K (2400°F)), the relative magnitude of the transient was greater than 5. Transient behavior occurred for all material conditions. The relative magnitude of the transient was nearly constant with grain diameter, but decreased with increasing L/D ratio.

The observed strain rate change transient was thought to be a real effect associated with the deformation characteristics of the specimen, rather than an

extraneous effect due to the testing apparatus. Properties of the transient which support this conclusion are: 1) the transient occurred only on the first strain rate change upon loading; 2) the transient was not present when the first strain rate change was high-to-low; 3) the transient disappeared at low test temperatures. Differential strain rate change transient behavior has not been reported in the literature (1,5) for TD-nickel, perhaps because the effect was ignored, or perhaps because the first strain rate changes were made from high to low strain rates. Transient values of $(\partial \ln \dot{\varepsilon}/\partial \sigma)_T$ were not used in calculations of tensile activation enthalpies.

Yield stress versus temperature plots, as well as differential temperature change tests, were employed to obtain values for $(\partial \sigma/\partial T)_{\dot{\varepsilon}}$. Agreement between the two measurement methods was good in all cases. The internal stress σ_i was measured using stress relaxation tests (32).

Activation enthalpies calculated from Equation 13 are plotted versus temperature for Condition D in Figure 18. ΔH increased dramatically with temperature, to values which can only be regarded as physically unrealistic. Comparison of the present results with

those of Lasalmonie and Sindzingre (5) indicates that such trends have been observed in the past.

The influence of grain diameter and L/D ratio on the activation enthalpy calculated from Equation 13 is shown in Figure 19. Condition D was used for both the small grain size and equiaxed grain shape, as previous tensile results indicated very little difference between Conditions A and D. Activation enthalpies in Figure 19 are high compared to the self diffusion enthalpy (3 ev), and are in reasonable agreement with the previous work of Doble (1).

Measured internal stresses are shown as a function of temperature in Figure 20 for Condition D. The ratio of the internal stress to the applied stress, σ_i/σ, increased with increasing temperature, approaching values close to 1 at the higher temperatures. Effects of grain diameter and L/D ratio on the internal stress may be seen in Figure 21. σ_i/σ was not strongly influenced by these variables.

Effects of strain on ΔH and σ_i/σ were examined for Condition D, which possessed a high ductility. Results are shown in Figure 22. Both these quantities tended to decrease with increasing strain.

The ratio of the measured internal stress to the

shear modulus, σ_i/μ, is shown versus temperature in Figure 23, for Condition D. The ratio is not constant with temperature. This means the assumption that σ_i is proportional to the shear modulus does not hold for Condition D in tension. This is in contrast to the properties of pure nickel, where the internal stress has been shown to be related to the elastic constants (10). As Equation 13 relied on this assumption, the results in Figure 23 indicate that Equation 13 cannot be applied directly to calculate activation enthalpies. Rather, Equation 11 must be used. As will be shown, this is the source of the unrealistic activation enthalpies obtained in Figure 18.

Since measurements of σ_i were made as a function of temperature for Condition D, values of σ^* could be obtained through Equation 12. This has been done to develop the data shown in Figure 24. Values of $(\partial\sigma^*/\partial T)_{\dot{\varepsilon}}$ were derived from Figure 24, for use in Equation 11.

Activation enthalpies for Condition D were re-calculated using Equation 11, and are shown in Figure 25. Although ΔH increases above the self diffusion enthalpy at higher temperatures, the high values are now at least near the boundaries of

physical reality.

σ_i was not measured as a function of temperature for the other material conditions for which ΔH was calculated from Equation 13 (Figure 19). Thus, $(\partial\sigma^*/\partial T)_{\dot{\varepsilon}}^*$ could not be obtained for these conditions from measurements. However, based on the admittedly unjustified assumption that the ratio of $(\partial\sigma^*/\partial T)_{\dot{\varepsilon}}^*/(\partial\sigma/\partial T)_{\dot{\varepsilon}}^*$ was the same for these conditions as for Condition D, values were recalculated using Equation 11. These recalculated values are shown in Figure 26. They are all less than the nickel self diffusion enthalpy.

B. Creep

1. Creep Test Data

Creep behavior was observed as a function of stress at 1255°K (1800°F) for Conditions B, C-2, D, E, and F. Condition D served as both the small grain size and equiaxed grain shape. Creep curves for Condition D as a function of stress are shown in Figure 27.

Figures 28 and 29 indicate the stress dependence of the steady state creep rate. As these figures show, it was not possible in the present investigation to

define the functional dependence of the steady state creep rate on stress. The dependence could equally well have been exponential in stress or stress raised to a power.

Slopes derived from Figures 28 and 29 are presented in Figures 30 and 31. Conventional values (Figures 28 and 29) are also compared with data obtained from differential stress change tests. The comparison is close except for Conditions C-2 and F. Differential data may be more accurate, since relatively few creep tests were run to obtain each conventional value, thus leaving these values susceptible to normal creep test scatter in the steady state creep rate. The degree of scatter was greatest for Conditions C-2 and F.

Assuming a power dependence of steady state creep rate on stress, Figure 31 indicates that the stress exponent increased with increasing L/D ratio and increasing grain diameter. The observed trend with L/D ratio is in agreement with previous work (2,6), while the trend with grain diameter is not (2,7). Values for Conditions D and B were somewhat higher than have been reported (2,7). For Condition D, differential tests showed the stress exponent to be independent of

strain.

Influences of stress level on primary and steady state creep strain are shown for the various material conditions in Figures 32 and 33. In all cases, tertiary creep strain was small. Condition D possessed the largest creep strains, with both primary and steady state creep strain decreasing with decreasing stress. For Condition D, the steady state creep strain appeared to become constant at lower stresses. All other material conditions had much lower creep strains, and trends with stress were less marked. More variability in strain values was also noted for these other material conditions.

Dependence of the steady state creep rate on grain diameter and L/D ratio was examined in Figures 34 and 35. Creep rate values at various constant stresses were obtained by extrapolation of the plots in Figure 28. To minimize the potential error incurred as a result of extrapolation, stresses as close as possible to measured values were used.

If diffusion controlled grain boundary sliding is operative, Raj and Ashby (20) predict that a plot of ln $\dot{\varepsilon}_s$ versus ln (grain diameter) will be a straight line, with a slope of minus 2-3. Allowing for extrapolation

errors, Figure 34 may suggest such a functional relationship, although some slopes are larger than predicted.

In a plot of ln $\dot{\varepsilon}_s$ versus ln (L/D ratio), a linear relationship with slope between -½ and -2 is expected for diffusion controlled grain boundary sliding (20). For stresses close to experimental values, slopes in Figure 35 are much larger than predicted.

Stress-rupture characteristics exhibited by the various material conditions at 1255°K (1800°F) are shown in Figure 36. Although tests were conducted at constant stress, strains were small enough so that constant load conditions very nearly prevailed. Typical stress-rupture plots were obtained for all material conditions.

2. Creep Thermal Activation Parameter Measurements

The apparent activation enthalpy may be calculated from measurements made in creep with the following express (29-32):

$$\Delta H = kT^2 \left(\frac{\partial \ln \dot{\varepsilon}}{\partial T}\right)_{\sigma^*} \qquad (14)$$

where $\dot{\varepsilon}$ is the creep rate. The effective stress σ^* is defined in Equation 12. With the assumption that the internal stress σ_i is proportional to the shear modulus, Equation 14 becomes:

$$\Delta H = kT^2\{(\frac{\partial \ln \dot{\varepsilon}}{\partial T})_\sigma + (\frac{\partial \ln \dot{\varepsilon}}{\partial \sigma})_T (\frac{\sigma_i}{\mu} \frac{d\mu}{dT})\} \qquad (15)$$

Equation 15 was used to calculate activation enthalpies from creep measurements. This expression incorporates a correction term for the change in internal stress σ_i with changes in temperature. Values for $(\partial \ln \dot{\varepsilon}/\partial T)_\sigma$ were obtained from differential temperature change tests. Data in Figure 30 were used for $(\partial \ln \dot{\varepsilon}/\partial \sigma)_T$. Table 3 was employed for the shear modulus variation with temperature.

σ_i was approximated by using the applied stress, since no internal stress measurements were made in creep. This is a good approximation in tension (Figures 20 and 21). However, in tension it was also found that the internal stress was not proportional to the shear modulus. Thus, the validity of the internal stress correction factor in Equation 15 is open to question. However, since $(\partial \sigma_i/\partial T)$ was not known, Equation 15 was used as a first approximation to

internal stress corrections. Corrections to steady state creep activation enthalpies were never more than 30% of the uncorrected values (given by $kT^2 (\partial \ln \dot{\varepsilon} / \partial T)_\sigma$). Upper limits to the creep activation enthalpies are fixed by simply neglecting to correct for the internal stress, giving steady state values about 30% larger than calculated from Equation 15.

Creep activation enthalpies obtained for the various material conditions are presented as a function of stress and strain in Figures 37-41. Tests at different stress levels were made at constant temperature.

Condition D possessed the greatest ductility of all material conditions in creep, thus allowing the maximum number of ΔH measurements as a function of strain (Figure 37). Low ΔH values were measured in the primary creep region. In the steady state region, ΔH was constant with strain, and close to the nickel self diffusion enthalpy. ΔH values for Condition D were not stress dependent.

The behavior of Condition B was similar to that of Condition D (Figure 38), with ΔH close to the self-diffusion enthalpy and independent of strain. Condition C-2, however, showed some strain dependency

of ΔH, and exhibited a value somewhat higher than self diffusion (Figure 39).

Activation enthalpies for Condition E (Figure 40) were for the most part near the self-diffusion enthalpy. One value was low and may have been associated with primary creep. ΔH did not seem strongly stress dependent for this condition, and trends with strain were not obvious, due to the limited number of measurements.

Condition F contrasted with Condition D in that activation enthalpies were strongly stress and strain dependent (Figure 41). ΔH increased with decreasing stress and increasing strain. At a stress of 9.60×10^7 N M^{-2} (13,920 psi), all values were below 3 ev and only weakly strain dependent. However, at 8.40×10^7 N M^{-2} (12,180 psi), ΔH increased markedly with strain, reaching a final value above 10 ev.

Trends in measured creep activation enthalpies with grain size and grain shape are shown in Figure 42. ΔH is constant at small and intermediate equiaxed grain sizes, increasing somewhat at the large grain size. ΔH values with grain size are near that of nickel self diffusion. With increasing L/D ratio, ΔH increases to values much higher than the self

diffusion enthalpy, depending on applied stress level as was shown in Figure 41.

Present results are compared with the literature values of Wilcox and Clauer (6,7) in Figure 42. Reasonably close agreement is observed. The results in Figure 42 show for the first time that high activation enthalpies in TD-nickel are associated with high L/D ratios, and may also be associated with large grain diameters.

C. Fractography

Fracture surfaces of elevated temperature tensile specimens (tested in vacuum) were examined with the scanning electron microscope. Conditions B, C-1, C-2, D, E and F were observed. Comparisons were made between room temperature and elevated temperature (1366^{o}K (2000^{o}F)) fracture surfaces.

Figures 43 and 44 show the room temperature and elevated temperature fracture surfaces, respectively, of Condition D. Condition D was ductile at room temperature, and the fracture surface presents a fibrous appearance typical of ductile fractures. The spacial separation of features in Figure 43 was smaller than the measured average grain diameter,

indicating that the room temperature deformation mode was intragranular.

The 1366°K (2000°F) fracture surface of Condition D (Figure 44) was markedly different from that of room temperature. The fracture surface had many smooth areas, and shapes of features suggested the grain structure of the material. Spacial characteristics of fracture features matched the measured average grain diameter. The nature of the elevated temperature fracture surface suggested an intergranular fracture mode.

The fracture surface of Figure 44 was necessarily exposed to the elevated temperature, while the room temperature fracture surface (Figure 43) was not. To compensate for this difference, the room temperature fracture surface was given the same temperature exposure as that of Figure 44. Exposure smoothed out all the jagged features in Figure 43, but did not produce the apparent grain outline structure of Figure 44. The small particles evident in Figure 44 may be thoria, although they were not identified in the investigation. These particles also appeared when the room temperature fracture surface was exposed to elevated temperature.

Conditions D, E and F all exhibited surface features similar to those of the elevated temperature fracture surfaces. The spacial separation of fracture features decreased with increasing L/D ratio, as expected of an intergranular fracture mode. Conditions B, C-1 and C-2 showed intergranular cracks at magnifications low enough to contain a number of grain boundaries within the field of view (200-500X). At the magnification of Figure 44, these conditions were much less featured than Conditions D, E, and F.

D. Transmission Electron Microscopy

Tensile and creep specimens of Condition D were observed by high voltage (650 KV) transmission electron microscopy. Attention was focused on Condition D, since this material condition exhibited the highest ductilities in both tension and creep, thus maximizing the possibility of observing distinct deformation features.

Tensile tests at 1366°K (2000°F) were run to approximately 15% elongation (one-half of the total elongation), whereupon the test was stopped and the specimen cooled under load. Creep tests at 1255°K (1800°F) and a stress of 2.48×10^7 N M^{-2}

(3592 psi) were terminated midway along the steady state region, and the specimen cooled under load. For both tensile and creep specimens, thin foils were obtained from the center of the gage section.

The most striking substructural feature observed in both tension and creep was deformation induced movement of the thoria particles and their collection at grain boundaries. Examples of this phenomenon are shown in Figure 45 for tension and Figure 46 for creep. It appeared that elevated temperature deformation caused the thoria particles to move in relation to the grain boundaries. The magnitude of this effect seemed about the same for both tension and creep. While the thoria dispersion was not perfectly random in the undeformed state, the degree of non-randomness introduced by deformation was still striking by comparison.

This phenomenon may explain the difficulty encountered in preparing thin foils of the deformed specimens. Electrochemical thinning procedures which were highly successful for undeformed samples (i.e. gave brilliant polishes with minimal pitting of the sample) produced severe pitting in deformed specimens, even though identical conditions were employed. The

severe pitting may have been due to preferential chemical attack at regions of high (or low) thoria content produced by deformation.

The literature contains no mention of deformation induced thoria dispersion non-randomness, as observed by transmission electron microscopy. High voltage transmission electron microscopy maximizes such an effect since thicker specimen areas may be observed. Previous investigations have all been conducted at 100 KV. It is also possible that previous workers neglected the phenomenon altogether.

Dislocation substructures were more prominent in tension than in creep, although quantitative dislocation density measurements were not made. Two dislocation features of interest were noted. These were parallel dislocation arrays (Figure 47), and grain boundary dislocation sources (Figure 48). Such features have been noted in the literature (6,7). In tension, isolated areas exhibited a high density of tangled dislocations, but there was no uniform formation of a distinctive dislocation cell structure. Nearly all dislocations were observed to be "pinned" to thoria particles (Figure 47). Dislocation segments bowed out between thoria particles were commonly observed.

DISCUSSION

A. Model for the Elevated Temperature Deformation of TD-Nickel

1. Proposal I

To explain the observed behavior of TD-nickel, it is proposed that two concurrent (parallel) processes may contribute to elevated temperature deformation. The first is diffusion controlled grain boundary sliding, while the second is dislocation motion.

The observation in transmission electron microscopy that the thoria particle distribution was altered by deformation suggests diffusion controlled grain boundary sliding. Such a result would occur if thoria particles acted as inert markers with respect to lattice diffusion. This effect has also been predicted by Burton (34), although no observations of the phenomenon were made. Aside from exceptional circumstances (e.g. very high temperatures and very low stresses), dislocation motion is expected to contribute to the deformation of metals, since dislocations are the primary flow defects.

On the basis of Proposal I, the total shear strain

rate will be given by:

$$\dot{\gamma} = \dot{\gamma}_{GBS} + \dot{\gamma}_{DIS} \qquad (16)$$

where $\dot{\gamma}$ = total shear strain rate, $\dot{\gamma}_{GBS}$ = shear strain rate due to diffusion controlled grain boundary sliding, and $\dot{\gamma}_{DIS}$ = shear strain rate due to dislocation motion. The functional dependencies of $\dot{\gamma}_{GBS}$ have been described by Raj and Ashby (20). $\dot{\gamma}_{DIS}$ will be given by the considerations of Proposal II.

2. Proposal II

It is proposed that both dislocation glide and climb are strongly influenced by matrix stresses at thoria particles, which arise from surface tension effects at the particle-matrix interface. Appendix A describes the proposed surface tension effects for small, incoherent, second phase dispersed particles.

Surface tensions produce a pressure at the particle-matrix interface, which, in turn, causes a triaxial state of stress to be present in the matrix surrounding the particle. Such a situation has also been postulated for voids in copper by Nolfi and Johnson (35). The triaxial stress state is purely

deviational in character (i.e. there is no dilatational component). Surface tension effects of the type in Appendix A are expected to be important only for very small interfacial radii of curvature. This is the case in TD-nickel, where the average particle radius is 100 x 10^{-10} M, and where many particles are smaller in size.

Matrix atomic displacements in Appendix A are radial in nature. Ashby and Brown (36,37) have calculated diffraction contrast expected in transmission electron microscopy from such strain effects. "D-lobe" contrast results for elastic strain fields of reasonable strength (ε = 0.013, for coherent particles), with the operative reciprocal lattice vector, $\bar{g}$, oriented perpendicular to the line of no contrast. Unusually large (anomalous) image widths occur for particles near the top or bottom of the foil, with black-white images produced in this case, rather than "D-lobe" images ($\bar{g}$ is still perpendicular to the line of no contrast). Bright and dark field views of anomalous images are identical for particles near the top of the foil, and complimentary for those at the bottom of the foil.

Efforts were made to image matrix surface tension

strain contrast features at thoria particles with the high voltage (650 KV) electron microscope. Matrix surface tension effects have elastic strain field strengths of only $\varepsilon = 0.0002$ (as calculated from Appendix A using values for TD-nickel). Thus, initial calculations (36,37) as to the visibility of such features showed they would be very difficult to image except under the most opportune conditions (high hkl $\bar{g}$ vector, particles near foil surfaces where images are unusually wide, very small particles, large extinction distances).

Potential thoria particle surface tension matrix strains are shown in Figures 49 and 50. A thin region of the foil was examined, so that many particles would be near the foil surfaces. Anomalous black-white images and some "D-lobe" images are evident. The reciprocal lattice vector $\bar{g}_{\bar{2}20}$ is perpendicular to the line of no contrast in all cases. Complimentary behavior in bright and dark field images is seen in some cases. Contrast effects are present for only the smallest thoria particles.

Figures 49 and 50 suggest a direct observation of thoria particle surface tension matrix strains. However, three other effects could also have been

operative. These are: 1) electron beam heating of the foil, to produce differential thermal expansion strains at the thoria particles; 2) presence of small dislocation loops, which give contrast effects identical to surface tension strain contrast; 3) "locked-in" differential thermal expansion strains from prior thermomechanical processing. Foil heating was not more than 25°K (45°F), which makes differential thermal expansion strains unlikely ($\varepsilon = 0.00005$). However, small dislocation loop effects could not be ruled out, nor could "locked-in" differential thermal expansion strains (although specimens were furnace heated and cooled). For these reasons, the features in Figures 49 and 50 must be regarded with caution as conclusive evidence for thoria particle surface tension matrix strains.

If matrix surface tension stresses are present, then Appendix B describes their interaction with edge dislocations. Shear stresses and climb stresses result, which will interact with both the dislocation glide and climb processes near the particle. Imai and Miyazaki (38) have obtained similar relationships for strain effects due to differential thermal expansion. Appendix B shows that an edge dislocation

near the particle will experience both glide and climb "pinning" forces. The magnitudes of the interactions are not negligible. Unlike differential thermal expansion stresses at second phase particles, surface tension stresses cannot be relieved at elevated temperatures by vacancy diffusion, since vacancy flow will not reduce surface tension interface stresses. Thus, the dislocation interactions described in Appendix B will always be operative at elevated temperatures, the temperatures of interest in the present investigation.

Thermally activated dislocation motion in the presence of the thoria particle-dislocation interactions discussed in Appendices A and B is examined in Appendix C, for edge dislocations. If thermally activated dislocation glide is the rate controlling process, then the creep rate will be given by:

$$\dot{\gamma} = \left(\frac{\pi^3}{6}\right)^{1/2} \frac{\rho b R_o \nu_o}{f^{1/2}} e^{-U/kT} \qquad (17)$$

where $\dot{\gamma}$ = shear strain rate, ρ = mobile dislocation density, b = Burgers vector, R_o = thoria particle radius, ν_o = frequency factor, f = volume fraction of thoria particles, k = Boltzman constant, T = absolute

temperature, and U = activation enthalpy.

The activation enthalpy U is of the form:

$$U = WL - \tau bA = U_o - \tau bA \qquad (18)$$

where W = dislocation-particle interaction energy per unit dislocation length (from Appendix B), L = length of dislocation interacting with the particle, τ = applied shear stress, and A = activation area. From Appendix C, U_o is estimated to have a value of 12.5 ev. U is stress dependent and decreases with increasing stress. The high value of U_o suggests that a portion of the applied stress τ will be required to lower the activation enthalpy barrier to the point where strain can be observed infinite times. Thus, τ in Equation 18 can be regarded as:

$$\tau = \tau^* + \tau_i \qquad (19)$$

where τ_i may be viewed as an internal stress and τ^* as an effective stress. Hence, the presence of an internal stress in addition to the internal stresses considered by Conrad (29-32) is implied by Equation 18. Properties of this internal stress will be dictated by

the other variables in Equation 18.

A description of thermally activated dislocation motion if climb is the rate controlling mechanism is derived in Appendix C. The shear strain rate is of the form:

$$\dot{\gamma} = \frac{\rho b M D_o \Omega \mu}{2N^{1/2}\pi^{3/2}(1-\nu)kTd_c^{5/2}} e^{-(\Delta H_{SD}+2F_j)/kT} \qquad (20)$$

where Ω = atomic volume, D_o = self diffusion coefficient pre-exponential, μ = shear modulus, N = dislocation source density, ν = Poisson's ratio, d_c = climb distance, M = factor describing the reduction in climb forces due to surface tension effects (M<1), ΔH_{SD} = self diffusion enthalpy, and F_j = jog formation energy. The jog formation energy is 0.59 ev for nickel, from Appendix C.

Equation 20 is similar to expressions derived by Weertman (13,39), except for the introduction of M and F_j, and assumptions concerning the stress dependence of the climb distance d_c.

3. Statement of the Model

Appendices A, B and C (Proposal II) showed that dislocation motion may be a much more difficult

process in a dispersion hardened material than in one without a dispersed phase. For this reason, the system will seek an easier deformation mode if one is available. Proposal I suggests that an alternative deformation mode is diffusion controlled grain boundary sliding.

From Proposals I and II, the total shear strain rate will be of the following form:

$$\dot{\gamma} = \frac{42\tau\Omega D_o}{kTd^2(L/D)^2} e^{-\Delta H_{SD}/kT} + \left(\frac{\pi}{6}\right)^{3/2} \frac{\rho b R_o \nu_o}{f^{1/2}} e^{-U/kT} \qquad (21)$$

where τ = shear stress, Ω = atomic volume, D_o = diffusion coefficient pre-exponential, ΔH_{SD} = self diffusion enthalpy, k = Boltzman constant, T = absolute temperature, d = grain diameter, L/D = grain L/D ratio, ρ = mobile dislocation density, b = Burgers vector, R_o = dispersed particle radius, ν_o = frequency factor, f = volume fraction of dispersed phase, and U = activation enthalpy. For polycrystals, $\dot{\gamma} = \sqrt{2}\,\dot{\epsilon}$ where $\dot{\epsilon}$ is the uniaxial strain rate, and $\tau = \sigma/2$ where σ is the uniaxial stress. The first term in Equation 21 is $\dot{\gamma}_{GBS}$ as given by Raj and

Ashby (20)* and the second term, $\dot{\gamma}_{DIS}$ is thermally activated dislocation glide (Equation 17) as calculated from Appendices A, B and C.

Dislocation glide has been taken as the rate controlling process for dislocation motion. This assumption is at odds with current theories of elevated temperature dislocation creep (17,39), which assume that dislocation climb (i.e. recovery) is rate controlling. However, thermally activated dislocation glide is considered better suited to explaining the behavioral characteristics of TD-nickel, than the corresponding climb process (Equation 20). The above assumption implies that dislocation climb occurs at a faster rate than dislocation glide. For steady state creep, the dislocation density must be reduced by some means (e.g. dislocation climb and annihilation, motion of dislocations to grain boundaries) or the material will monotonically strain harden.

---

*$\dot{\gamma}_{GBS}$ is proportional to $(L/D)^{-1}$ for large L/D ratios.

B. Predictions of the Model

1. Effects of Variables on Deformation Mode

The relative proportions of grain boundary sliding and dislocation motion that occur (i.e. the character of the deformation mode) will, from Equation 21, be sensitive to: 1) L/D ratio; 2) grain diameter; 3) stress; 4) temperature. Deformation modes may be different under different sets of these conditions.

At fixed temperature and stress, Equation 21 shows that the relative contribution of dislocation motion will increase with increasing L/D ratio and increasing grain diameter. For a fixed temperature and grain structure, the relative contribution of dislocation motion will increase with increasing stress, since $\dot{\gamma}_{DIS}$ is more stress sensitive than $\dot{\gamma}_{GBS}$. With a fixed stress and grain structure, the relative proportion of dislocation motion will increase with increasing temperature, provided $U > (\Delta H_{SD} - kT)$ at the fixed stress level.

The above discussion suggests that deformation modes in tensile and creep tests may be different. Stresses are necessarily higher in tension than in creep, because of the imposed tensile strain rate,

which is usually much greater than strain rates in creep. The higher strain rates in tension will favor dislocation motion as the dominant deformation mode.

To estimate the degree to which grain boundary sliding might contribute to the tensile deformation of TD-nickel, $\dot{\gamma}_{GBS}$ in Equation 21 was used to calculate the stresses required to drive grain boundary sliding at tensile strain rates. Except for small, equiaxed grain sizes (Conditions A and D), calculated stresses were higher than those observed in tension, and near to or greater than the theoretical Orowan stress for dislocation bowing between dispersed particles (Appendix B). This suggests that, in the present investigation, dislocation motion was the dominant deformation mode in tension, with grain boundary sliding occurring to a small (but finite) extent.

At the natural strain rates and lower stresses of creep deformation, grain boundary sliding should be more pronounced than in tension. This is especially true for small, equiaxed grain structures, where it may become the dominant deformation mode.

Equation 21 suggests that changes in deformation mode can accompany rapid strain rate changes of the kind made in differential strain rate change tension tests.

This would be especially likely for low-to-high strain rate changes, which might cause the dislocation density to increase. Such effects could account for the strain rate change transient behavior observed in TD-nickel.

2. Grain Size and Shape Dependence of Elevated Temperature Strength

For conditions where grain boundary sliding is the major deformation mode, Equation 21 indicates that elevated temperature strength will increase with increasing grain diameter and increasing L/D ratio. Observed tensile yield strengths did not possess the sensitivity to these variables predicted by grain boundary sliding.

When dislocation motion is dominant (e.g. in tension), strength levels might also be grain size and shape dependent, but to a lesser degree than for grain boundary sliding. Raj and Ashby (20) have analyzed the internal elastic stress distribution present in a polycrystal when grain boundary atomic layers are regarded as fluid. Maximum shear stresses generated by the applied stress, which occur at grain boundary triple points, are proportional to $\tau(L/D)^{-1}$. Thus, τ_{MAX} decreases with increasing L/D ratio, for a given

applied stress. If these stresses are regarded as driving dislocation motion, the applied stress to achieve a given strain rate must increase with increasing L/D ratio.

Changes in grain size are described as having no effect on internal shear stress levels (20). However, if it is assumed that grain boundary triple points are the major sources of dislocations, then the dislocation source density decreases with increasing grain diameter. For a given strain rate, dislocation velocities must necessarily increase. Therefore, the applied stress must increase with increasing grain diameter.

3. Grain Size and Shape Dependence of Elevated Temperature Ductility

Elevated temperature ductilities will be controlled by the fracture process. Fracture strains and times expected in a dispersion hardened material when diffusion controlled grain boundary sliding is the dominant deformation mode are derived in Appendix D. The fracture shear strain is:

$$\gamma_f = \frac{A(V_f - V_o)}{Bd^3 f} \qquad (22)$$

where A,B = constants, V_f = critical volume of dispersed particles at grain boundaries produced by grain boundary sliding, V_o = initial volume of dispersed particles at grain boundaries, d = grain diameter, and f = volume fraction of dispersed phase. The value of B increases with increasing L/D ratio. Ductility decreases with increasing grain diameter, increasing L/D ratio, and increasing volume fraction of dispersed phase.

At elevated temperatures, if dislocation motion is the major deformation mode, intergranular fracture may still be the operative fracture mode. The probability of intergranular cracking should increase with increasing applied stress. Because of strength level trends, ductility should then decrease with increasing L/D ratio and increasing grain diameter. This was the observed trend for TD-nickel in tension.

4. Internal Stress

For diffusion controlled grain boundary sliding in a dispersion hardened material, Ashby (21) has suggested that the ability of grain boundaries to absorb or emit vacancies may lead to the presence of an internal stress proportional to μ/d, where μ is the shear modulus and d is approximately the inter-

particle spacing. The temperature dependence of this stress is that of the shear modulus.

The internal stress for dislocation motion controlled by glide is discussed in Appendix C. It is possible that the internal stress can be an appreciable fraction of the applied stress. Furthermore, the temperature dependence of the internal stress depends on that of the surface energy, rather than the shear modulus. This dependence is (from Appendix C):

$$\frac{d\tau_i}{dT} = \frac{0.646\ L}{A} \frac{dE_s}{dT} \qquad (23)$$

where τ_i = internal stress, T = temperature, L = dislocation length interacting with the dispersed particle, A = activation area, and E_s = surface energy.

Using values for L and A in Appendix C and a value of -0.6×10^{-3} joule $M^{-2}{}^{\circ}K^{-1}$ (40) for dE_s/dT, the calculated value of $d\tau_i/dT$ is -3.88×10^4 N $M^{-2}{}^{\circ}K^{-1}$. Measured values of $d\tau_i/dT$ were near -3×10^4 N $M^{-2}{}^{\circ}K^{-1}$. This is remarkably good agreement, considering the approximate nature of the calculated value.

When dislocation motion is the dominant deformation mode, the previous analysis suggests that the temperature dependence of elevated temperature strength levels

will be controlled by the temperature dependence of the internal stress. This accounts for the temperature sensitivity of tensile yield strengths observed in TD-nickel. Equation 23 and Appendix C also provide explanations for the high internal stress levels noted, and the fact that the measured internal stress was not proportional to the shear modulus.

5. Stress Dependence of Strain Rate

From Equation 21, the stress sensitivity $d\ln\dot{\gamma}_{GBS}/d\ln\tau$ should be equal to unity when diffusion controlled grain boundary sliding is the major deformation mode. Measured stress sensitivities could increase, however, if an internal stress of the type discussed by Ashby (21) is present. When $\dot{\gamma} = A(\tau-\tau_i)^N$, the measured stress sensitivity will be:

$$\frac{d\ln\dot{\gamma}}{d\ln\tau} = \frac{N\tau}{\tau-\tau_i} \qquad (24)$$

for τ_i not a function of τ. Such an effect may have occurred for Condition D in creep, where grain boundary sliding was thought to be the dominant deformation mode, but measured values of $d\ln\dot{\gamma}_{GBS}/d\ln\tau$ were near 13.

When dislocation motion is the controlling deformation mode, Equations 18 and 21 indicate that $\dot{\gamma}_{DIS}$ is exponential in stress, rather than having a power law

stress dependence. This stress dependence is given by:

$$\frac{d\ln\dot{\gamma}_{DIS}}{d\tau} = \frac{bA}{kT} \qquad (25)$$

as described in Appendix C.

On the above basis, the expression for $d\ln\dot{\gamma}_{DIS}/d\ln\tau$ will be $\tau bA/kT$. Hence, this quantity should increase with increasing applied stress. For Condition F in creep, where dislocation motion was thought to be the dominant deformation mode, the calculated value of $d\ln\dot{\gamma}_{DIS}/d\ln\tau$ is 260. The observed differential value was 34. The large discrepancy may indicate that $d\ln\dot{\gamma}_{DIS}/d\ln\tau = \tau^* bA/kT$, where τ^* is the effective stress as shown in Equation 19 and discussed in Appendix C. If this is the case, then, from the above, $\tau^* \simeq 0.1\,\tau$, where τ is the applied stress.

Since the quantity $d\ln\dot{\gamma}_{DIS}/d\ln\tau$ increases with increasing stress, this suggests an explanation for the observation (2) that the stress exponent increases with increasing L/D ratio in TD-nickel. Applied stresses were observed to increase with increasing L/D ratio. The above analysis also provides a basis for the large values of $d\ln\dot{\gamma}/d\ln\tau$ observed in TD-nickel.

6. Activation Enthalpy

The measured activation enthalpy for diffusion controlled grain boundary sliding is the self-diffusion enthalpy. This quantity will be independent of stress, strain and temperature.

However, for dislocation motion, the measured activation enthalpy will be stress dependent (Appendix C) and will increase with decreasing stress. It may also be strain sensitive, if strain alters internal stresses. Finally, the measured activation enthalpy will be temperature dependent, increasing with increasing temperature to a constant value at a critical temperature where the activation barrier becomes "transparent" (29-32). This critical temperature may be above the melting point of the material.

The above suggests an explanation for the trends observed in measured activation enthalpies in TD-nickel. In creep, it is thought that with increasing L/D ratio and increasing grain diameter, the character of the deformation mode changed from diffusion controlled grain boundary sliding to dislocation motion. The resultant high activation enthalpies were then reflective of the dislocation motion mode. In tension,

where dislocation motion was expected to dominate, the measured activation enthalpy increased with increasing temperature, to high levels as compared to the self diffusion enthalpy.

The question must be raised as to whether the high measured activation enthalpies attributed to the dislocation motion process are physically real, or apparent in some manner. $\dot{\gamma}_{DIS}$ in Equation 21 was calculated, using reasonable values for TD-nickel, and an activation enthalpy of 7 ev. The calculated strain rate was 10^{-18} sec^{-1}. Measured values were in the range of 10^{-8} sec^{-1}. This comparison strongly suggests that the high measured activation enthalpies are apparent.

The most probable source of apparent measured activation enthalpies lies in the temperature sensitivity of the activation enthalpy. When the activation enthalpy is temperature sensitive:

$$\Delta H = kT^2\{\frac{d\ln\dot{\gamma}}{dT} + \frac{1}{kT}\frac{d\Delta H}{dT}\} \qquad (26)$$

for a creep rate of the form $\dot{\gamma} = A\, e^{-\Delta H/kT}$.
The activation enthalpy temperature sensitivity is usually attributed to the change in internal stress with temperature, giving $(1/kT)(d\Delta H/dT) = (d\ln\dot{\gamma}/d\tau)(d\tau_i/dT)$.

Creep activation enthalpies were calculated with the internal stress temperature correction shown in Equation 15. The analysis indicates that the proper internal stress temperature correction may be that given in Equation 23. This correction term is expected to be larger than the shear modulus correction, thus reducing the measured values of activation enthalpy to realistic levels.

C. Strengthening of Dispersion Hardened Materials

The proposed model can explain the elevated temperature deformation behavior of TD-nickel observed in the present investigation. The model accounts for: 1) grain size and shape dependence of elevated temperature strength and ductility; 2) differences between tensile and creep behavior; 3) strain rate change transient behavior; 4) internal stress levels; 5) temperature dependence of elevated temperature strength; 6) stress sensitivities; 7) activation enthalpies. Most importantly, potential explanations are provided for the high activation enthalpies and stress dependencies which have been observed in TD-nickel (1,2,5,6,7), and the dependence of these quantities on grain structure.

The proposed model applies to all dispersion hardened materials of the same class as TD-nickel (e.g. SAP alloys, TD-nickel alloys such as TD-nickel-chromium). For this reason, it is appropriate to outline means by which the elevated temperature strengths of these materials may be optimized.

In a single crystal of a dispersion hardened material, elevated temperature deformation will be dictated solely by dislocation motion, as described in Appendices A, B and C. This gives the inherent (i.e. maximum) strength of the dispersion hardened material. This inherent strength will be much greater than that of a pure metal because of the effects discussed. Strengths of polycrystalline dispersion hardened materials may be lower than the inherent strength, due to the occurrence of diffusion controlled grain boundary sliding as a concurrent deformation process with dislocation motion. In polycrystals, strength may be maximized by minimizing grain boundary sliding, through the production of grain structures with large grain diameters and high L/D ratios.

The inherent strength of the dispersion hardened material may also be optimized. From Appendices A, B and C, the inherent strength will increase with

increasing volume fraction of dispersed phase, and decreasing dispersed particle radius (at constant volume fraction). Inherent strengths will also increase as the surface energy of the matrix material increases.

CONCLUSIONS

The following conclusions may be drawn from the results and analysis of the present investigation concerning the elevated temperature deformation of TD-nickel:

1. Elevated temperature strength levels increase with increasing grain diameter and increasing L/D ratio.

2. The assumption that the internal stress is proportional to the shear modulus is not valid for tensile deformation. Measured tensile activation enthalpies will be apparent values only if this approximation is used.

3. Activation enthalpies in tension and creep are not the same.

4. Creep activation enthalpies increase with increasing L/D ratio and increasing grain

diameter, to high values as compared with the self diffusion enthalpy. These high values are apparent.

5. Two concurrent (parallel) processes may contribute to the elevated temperature deformation of polycrystalline TD-nickel. These are diffusion controlled grain boundary sliding, and dislocation motion. The relative contribution of dislocation motion increases with increasing L/D ratio and increasing grain diameter.

6. Dislocation motion is strongly influenced by matrix stresses at small, incoherent, second phase dispersed particles produced by surface tension effects at the particle-matrix interface.

7. Characteristics of the dislocation motion process provide explanations for the high activation enthalpies and stress sensitivities which have been observed in TD-nickel.

8. The elevated temperature strength of a polycrystalline dispersion hardened material will increase with increasing grain diameter and increasing L/D ratio, to an upper limit of the inherent strength. The inherent strength will increase with increasing volume fraction of dispersed phase, decreasing dispersed particle radius, and increasing matrix surface energy.

REFERENCES

1. G. S. Doble: Ph.D. thesis, Case Western Reserve University, November, 1967.

2. B. A. Wilcox, A. H. Clauer and W. B. Hutchinson: NASA contract NAS 3-11167 Final Report, March 1971.

3. R. W. Fraser and D. J. I. Evans: Oxide Dispersion Strengthening, vol. 47, p. 375, Gordon and Breach, New York, 1968.

4. C. J. Smithells: Metals Reference Book, vol. II, 4th edition, p. 644, Plenum Press, New York, 1967.

5. A. Lasalmonie and M. Sindzingre: Acta Met., 1971, vol. 19, p. 57.

6. B. A. Wilcox and A. H. Clauer: Trans. AIME, 1966, vol. 236, p. 570.

7. A. H. Clauer and B. A. Wilcox: Met. Sci. J., 1967, vol. 1, p. 86.

8. J. Weertman and P. Shahinian: Trans. AIME, 1956, vol. 206, p. 1223.

9. C. M. Sellars and A. G. Quarrell: J. Inst. Metals, 1961-62, vol. 90, p. 329.

10. J. E. Cannaday, R. J. Austin and R. K. Saxer: Trans. AIME, 1966, vol. 236, p. 595.

11. S. Karashima, H. Oikawa and T. Motomiya: Trans. JIM, 1969, vol. 10, p. 205.

12. B. A. Wilcox and A. H. Clauer: Trans. AIME, 1965, vol. 233, p. 253.

13. G. S. Ansell and J. Weertman: Trans. AIME, 1959, vol. 215, p. 838.

14. B. A. Wilcox and A. H. Clauer: Oxide Dispersion Strengthening, vol. 47, p. 323, Gordon and Breach, New York, 1968.

15. P. Guyot: Oxide Dispersion Strengthening, vol. 47, p. 405, Gordon and Breach, New York, 1968.

16. J. Friedel: Dislocations, p. 373, Pergamon Press, New York, 1964.

17. R. Lagneborg: J. Mat. Sci., 1968, vol. 3, p. 596.

18. M. Hillert: Acta Met., 1965, vol. 13, p. 227.

19. J. Tien, B. Kear and G. Leverant: Scripta Met., 1972, vol. 6, p. 135.

20. R. Raj and M. F. Ashby: Met. Trans., 1971, vol. 2, p. 1113.

21. M. Ashby: Scripta Met., 1969, vol. 3, p. 837.

22. J. J. Petrovic and L. J. Ebert: Met. Trans., 1972, vol. 3, p. 1123

23. J. J. Petrovic and L. J. Ebert: Met. Trans., 1972, vol. 3, p. 1131.

24. P. Flynn: National Science Foundation Undergraduate Summer Project, 1971, Case Western Reserve University.

25. J. J. Petrovic: M.S. thesis, Division of Metallurgy and Materials Science, Case Western Reserve University, Cleveland, Ohio, January, 1970.

26. R. L. Fullman, R. P. Carreker, Jr., and J. C. Fisher: Trans. AIME, 1953, vol. 197, p. 657.

27. N. J. Petch: J. Iron Steel Inst., 1953, vol. 174, p. 25.

28. E. O. Hall: Proc. Phys. Soc., 1951, Ser. B, vol. 64, p. 747.

29. H. Conrad: J. of Met., 1964, vol. 16, p. 582.

30. H. Conrad and H. Wiedersich: Acta Met., 1960, vol. 8, p. 128.

31. H. Conrad: Mechanical Behavior of Materials at Elevated Temperatures, p. 149, McGraw-Hill, New York, 1961.

32. H. Conrad: Mater. Sci. Eng., 1970, vol. 6, p. 265.

33. C. Susse: J. de Physique, 1956, vol. 17, p. 910.

34. B. Burton: Metal Sci. J., 1971, vol. 5, p. 11.

35. F. V. Nolfi, Jr. and C. A. Johnson: Acta Met., 1972, vol. 20, p. 769.

36. M. F. Ashby and L. M. Brown: Phil. Mag., 1963a, vol. 8, p. 1083.

37. M. F. Ashby and L. M. Brown: Phil. Mag., 1963b, vol. 8, p. 1649.

38. Y. Imai and T. Miyazaki: Trans. JIM, 1968, vol. 9 (Supplement), p. 569.

39. J. Weertman: Trans. ASM, 1968, vol. 61, p. 681.

40. L. E. Murr: Scripta Met., 1972, vol. 6, p. 203.

TABLE 1

VENDOR'S CHEMICAL ANALYSIS OF TD-NICKEL

AS-EXTRUDED 7.62 CM (3 INCH) BAR LOT 3555

ELEMENT	WEIGHT %
C	0.0063
S	0.0010
Cu	0.002
Ti	0.001
Co	0.060
Fe	0.007
Cr	0.001
ThO_2	2.6
Ni	BAL

TABLE 2

GRAIN SIZE AND SHAPE MEASUREMENTS

SPECIMEN CODE	VARIABLE	AVERAGE GRAIN DIMENSION (mm)	L/D RATIO	$\bar{L}_1$ (mm)	$\bar{L}_2$ (mm)	$\bar{L}_3$ (mm)
A	Grain Size	0.000971 ±.000080	1.12 ±.19	0.001243 ±.000105	0.001071 ±.000083	0.001141 ±.000097
B	Grain Size	0.0143 ±.0012	1.61 ±.25	0.0208 ±.0024	0.0188 ±.0016	0.0123 ±.0007
C	Grain Size	0.363 ±.040	3.14 ±.71	0.4125 ±.0339	0.9107 ±.1504	0.2105 ±.0181
D	Grain Shape	0.00105 ±.000095	1.11 ±.21	0.001239 ±.000134	0.001228 ±.000115	0.001167 ±.000092
E	Grain Shape	0.00112 ±.000056	5.19 ±.54	0.003967 ±.000235	0.0007663 ±.0000424	0.0007610 ±.0000274
F	Grain Shape	0.00126 ±.00017	11.03 ±3.94	0.007407 ±.002287	0.0006954 ±.0000421	0.0006481 ±.0000232

TABLE 3

SHEAR MODULUS VERSUS TEMPERATURE FOR NICKEL

TEMPERATURE (^{o}K)	TEMPERATURE (^{o}F)	μ (N M^{-2}) (X10^{10})	μ (X10^{6} psi)
273	32	7.94	11.52
373	212	7.72	11.22
473	392	7.45	10.84
573	572	7.25	10.47
673	752	6.96	10.11
773	932	6.70	9.70
866	1100	6.48	9.39
873	1112	6.46	9.37
973	1292	6.18	8.96
1073	1472	5.89	8.53
1089	1500	5.87	8.51
1173	1652	5.58	8.09
1255	1800	5.33	7.72
1273	1832	5.25	7.61
1366	2000	4.91*	7.11*
1477	2200	4.51*	6.54*
1589	2400	4.13*	5.98*

*Extrapolated

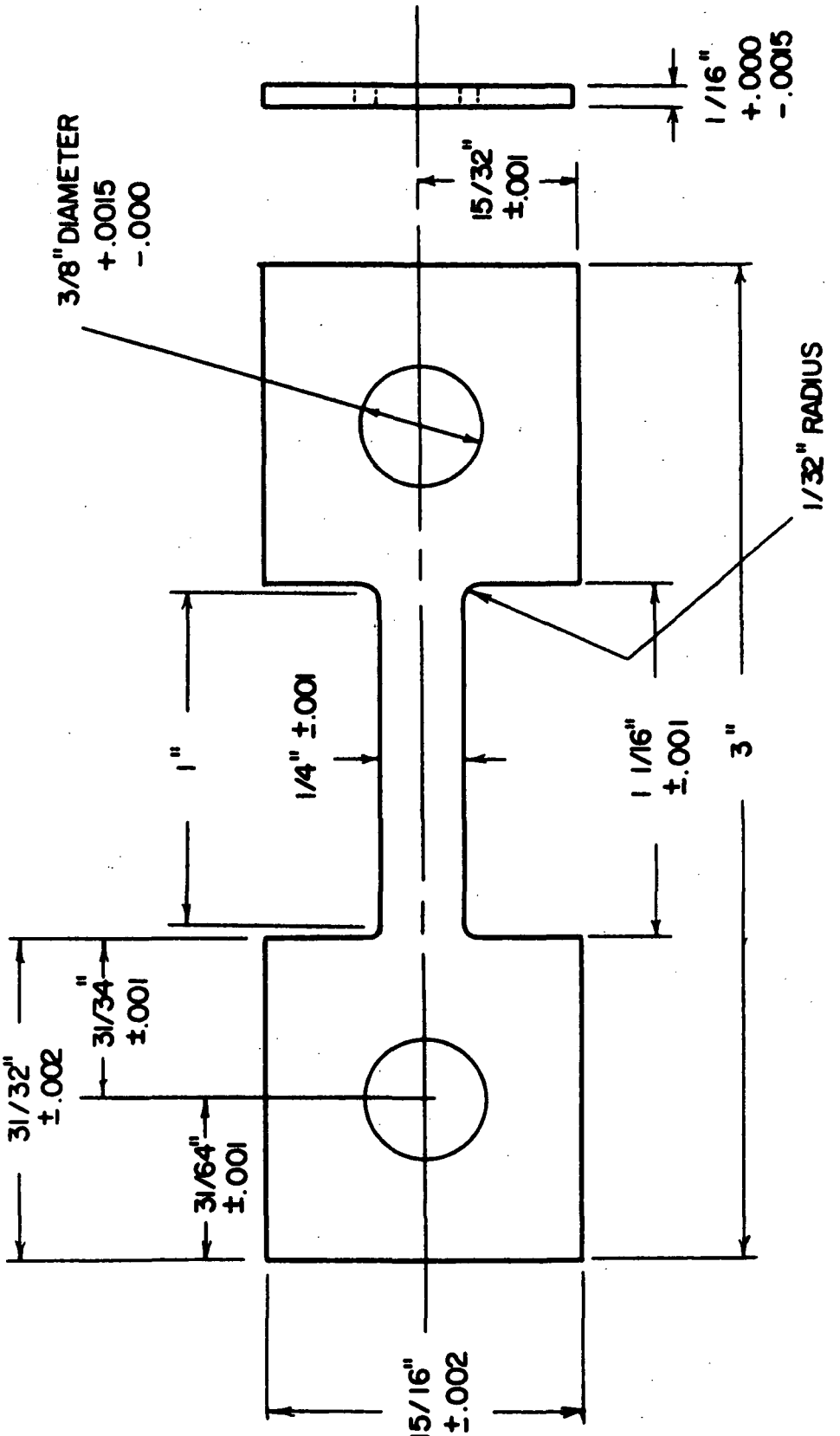

Figure 1 - Sheet specimen geometry.

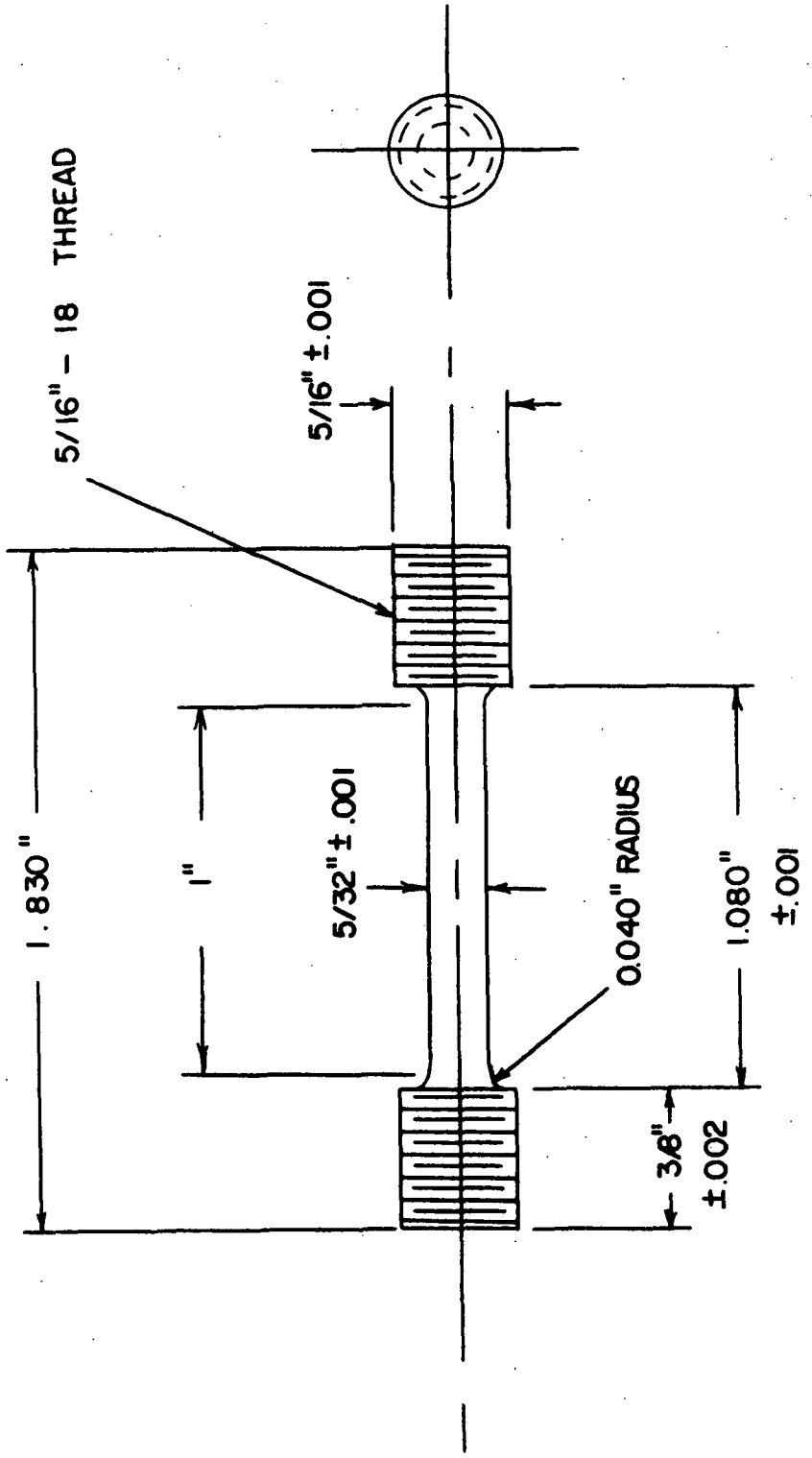

Figure 2 - Round specimen geometry.

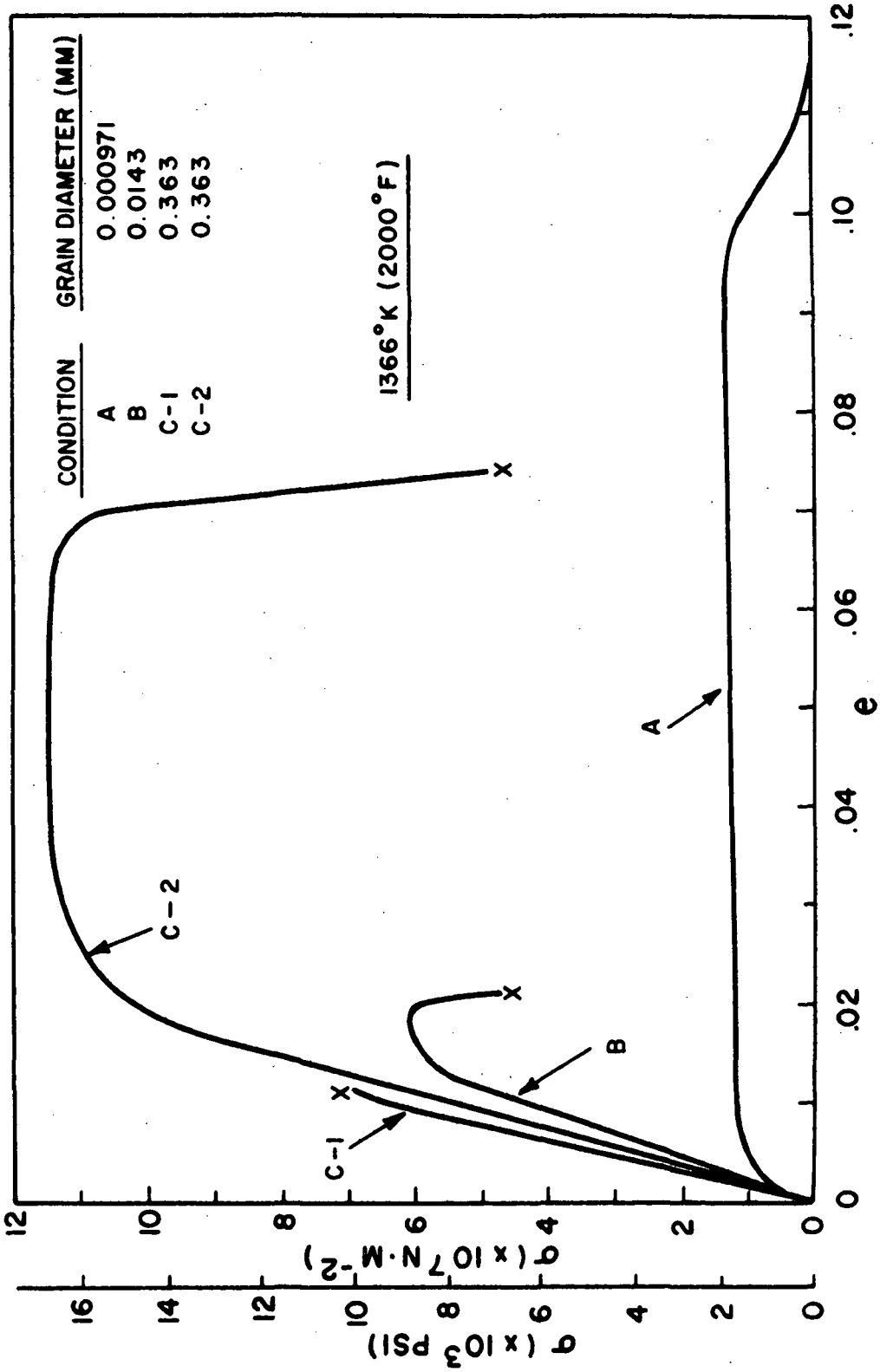

Figure 3 - Stress-strain curves for various grain sizes at 1366°K (2000°F).

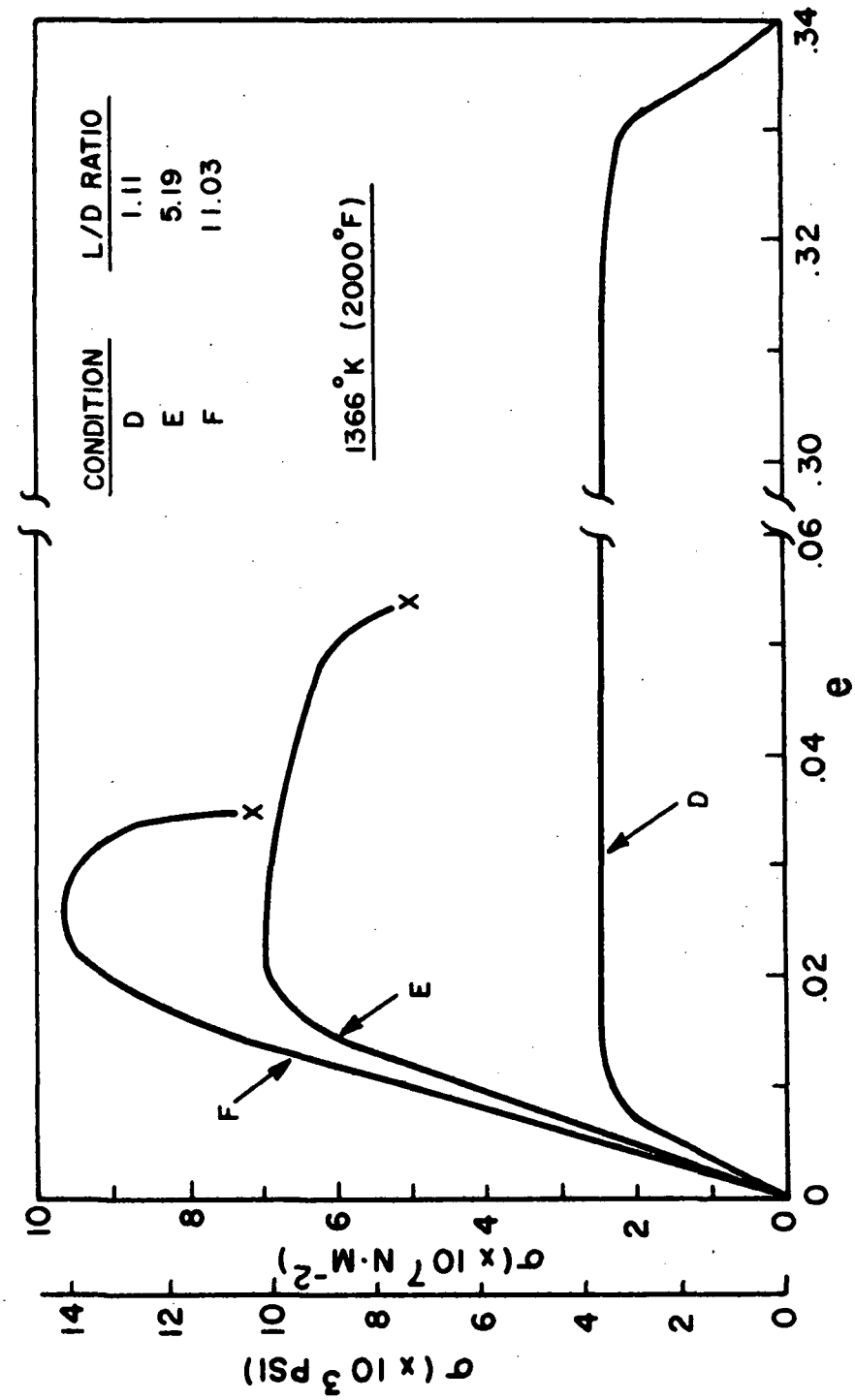

Figure 4 - Stress-strain curves for various grain shapes at 1366°K (2000°F).

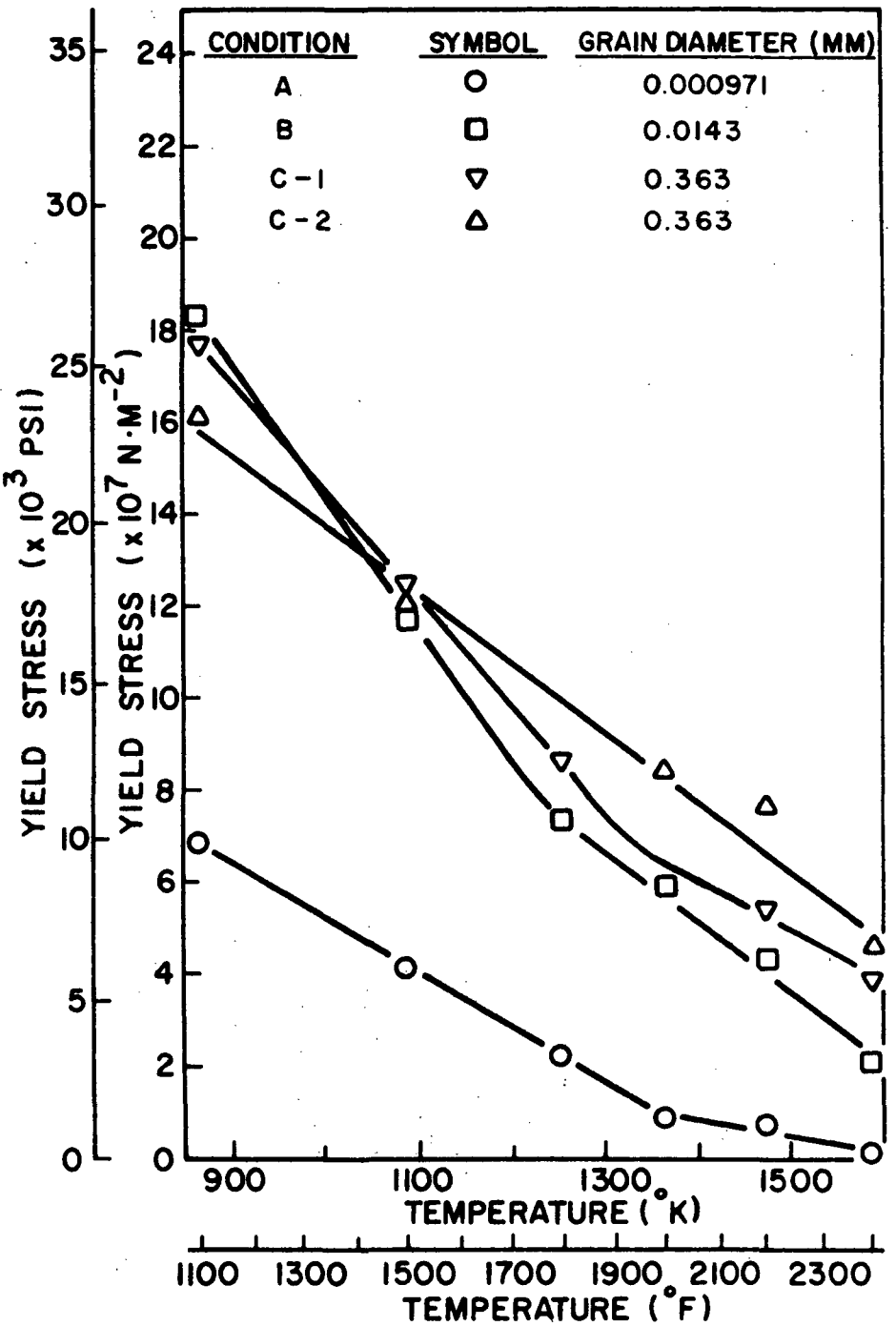

Figure 5 - Yield stress versus temperature for various grain sizes.

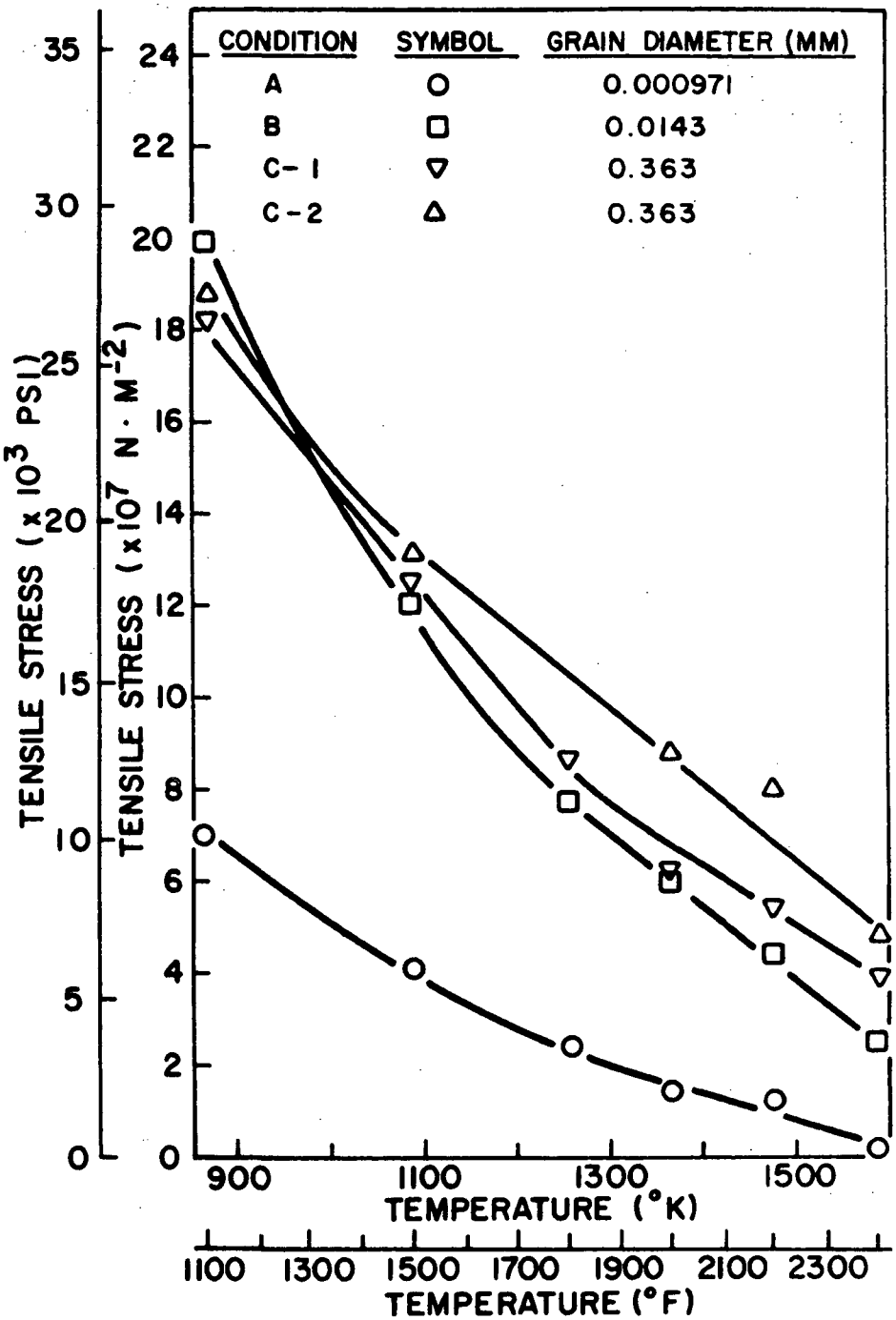

Figure 6 - Tensile stress versus temperature for various grain sizes.

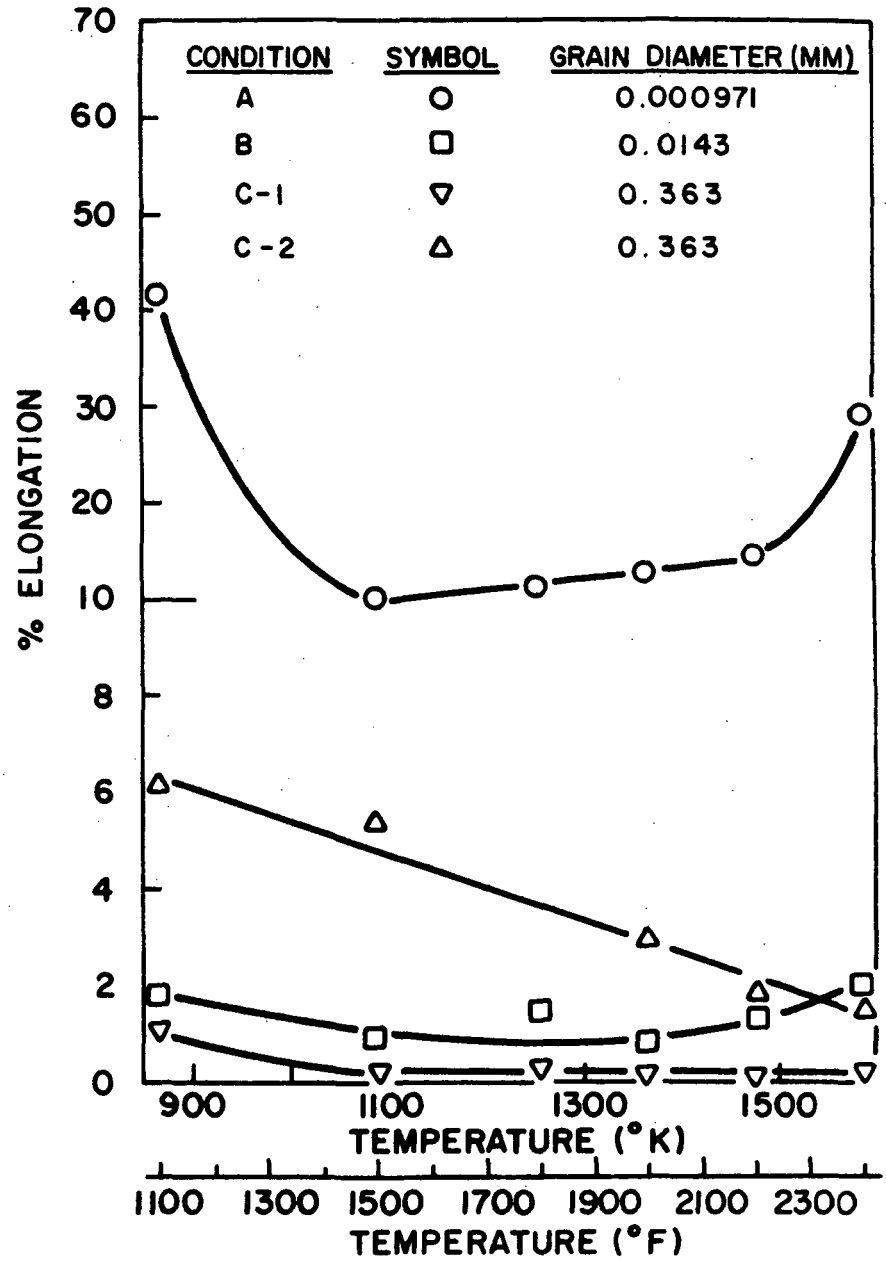

Figure 7 - % elongation versus temperature for various grain sizes.

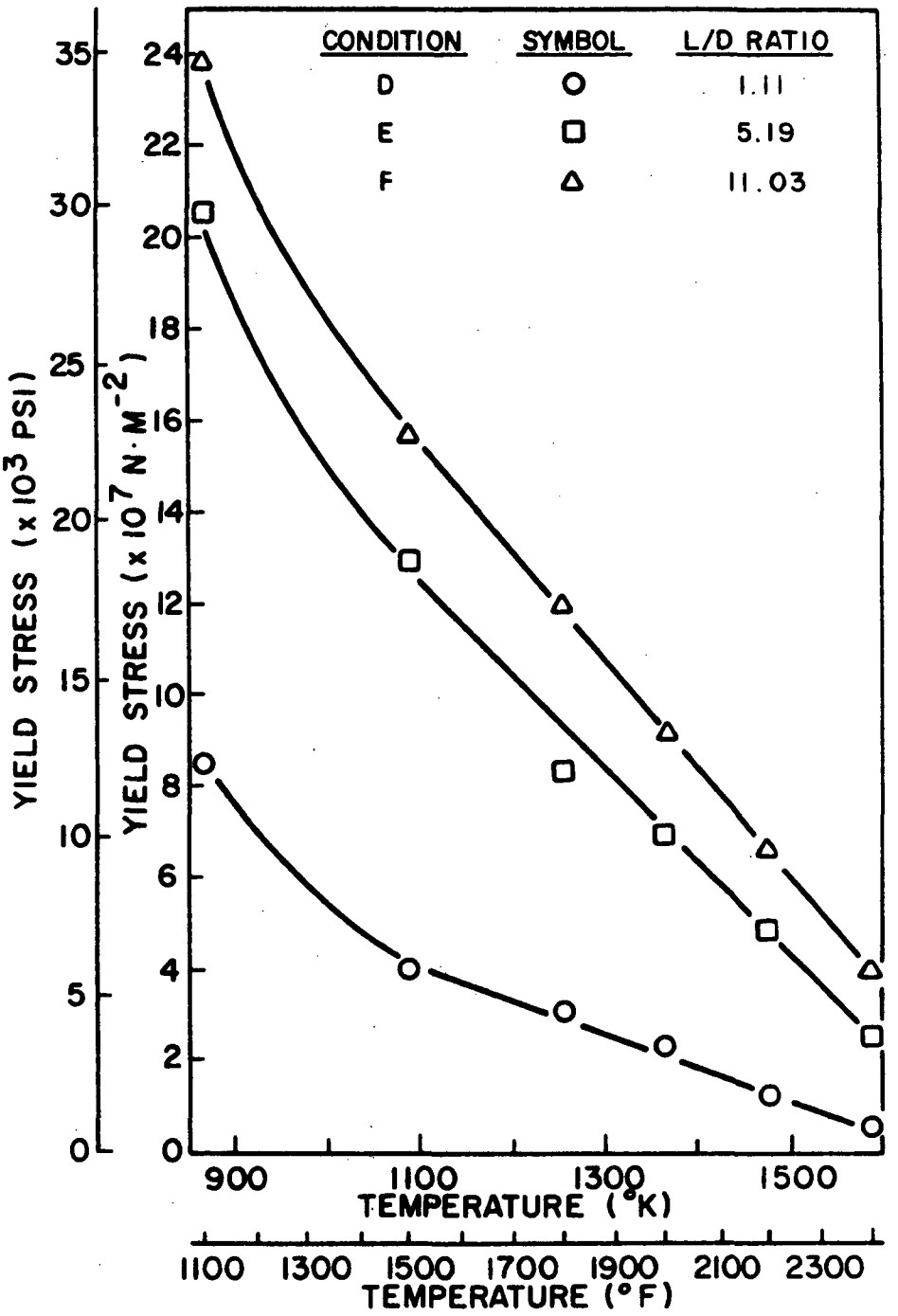

Figure 8 - Yield stress versus temperature for various grain shapes.

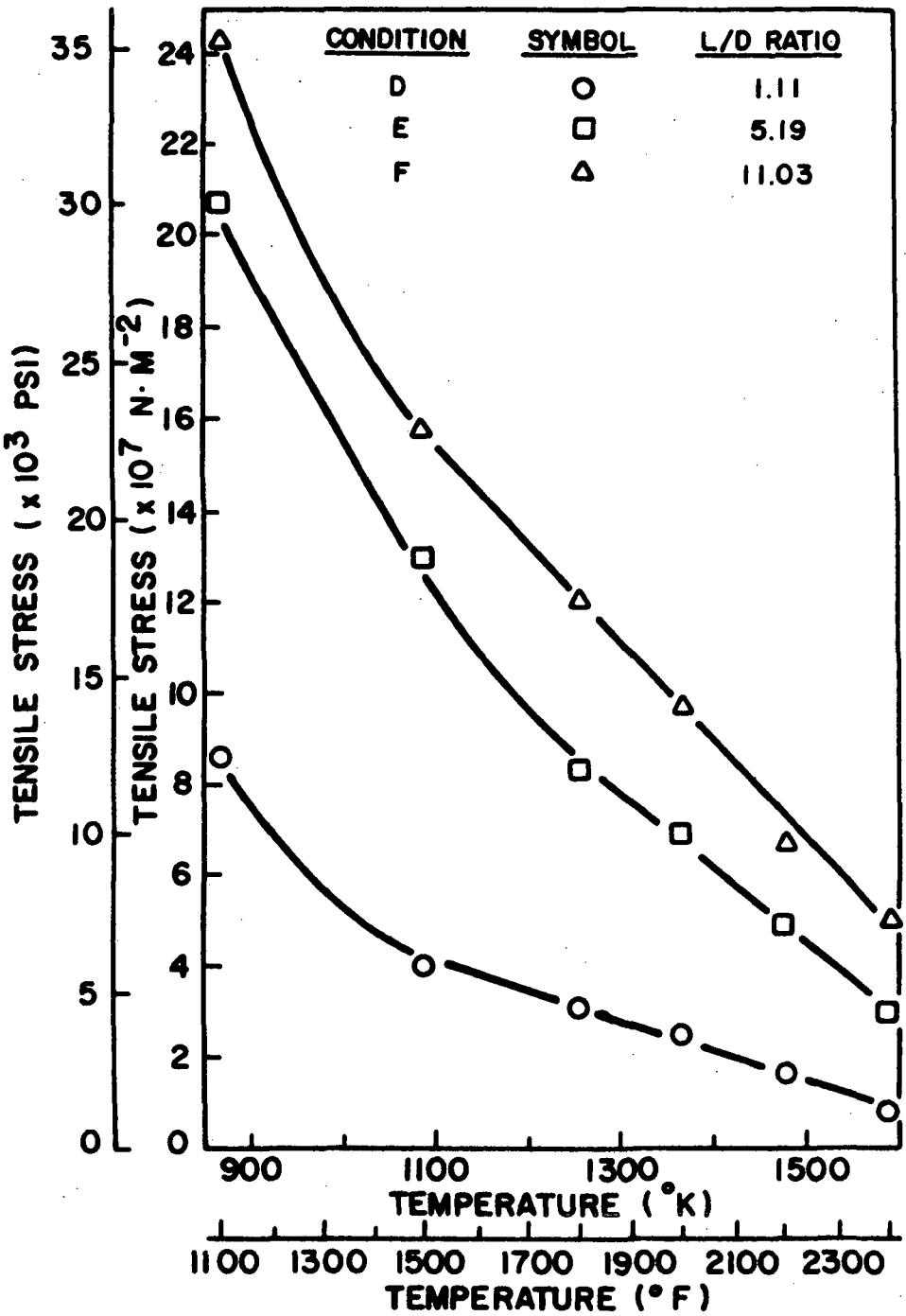

Figure 9 - Tensile stress versus temperature for various grain shapes.

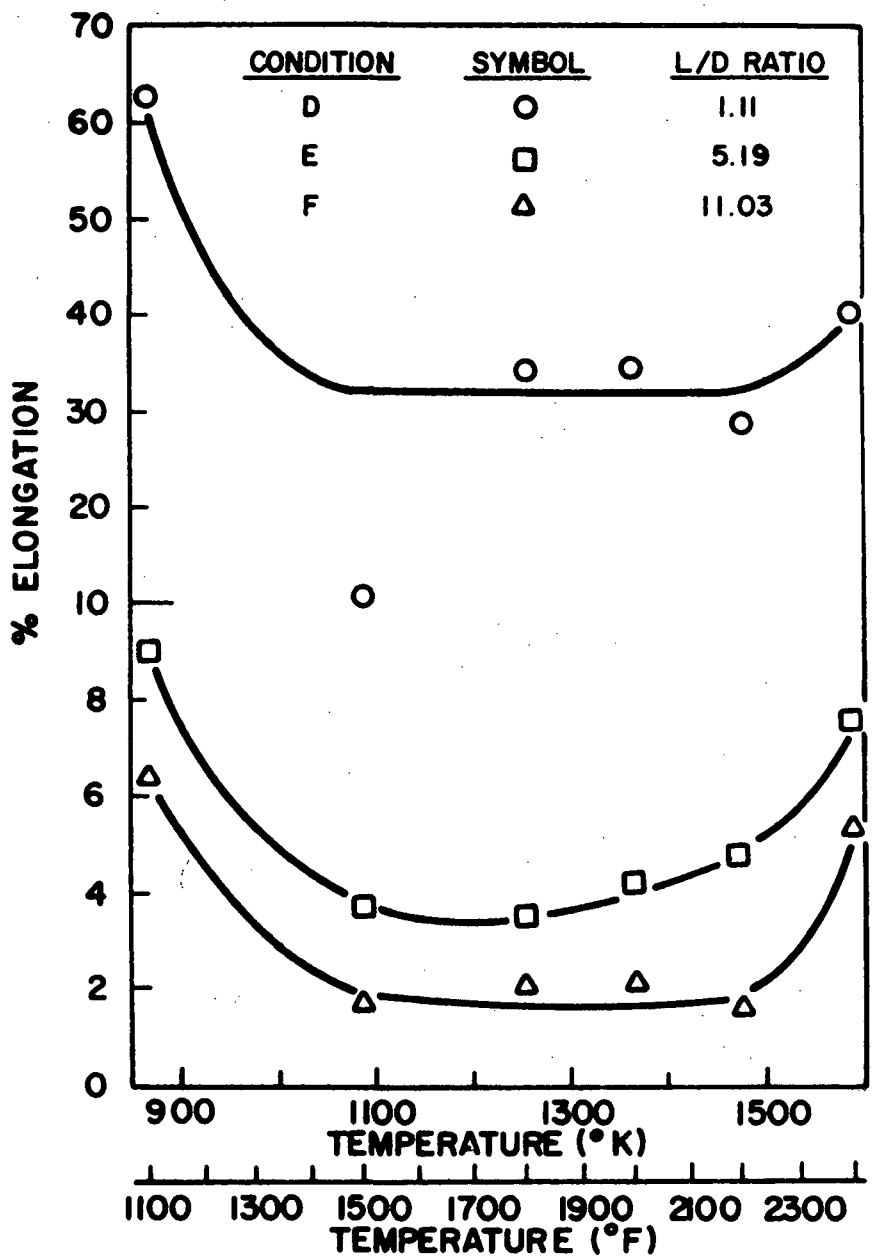

Figure 10 - % elongation versus temperature for various grain shapes.

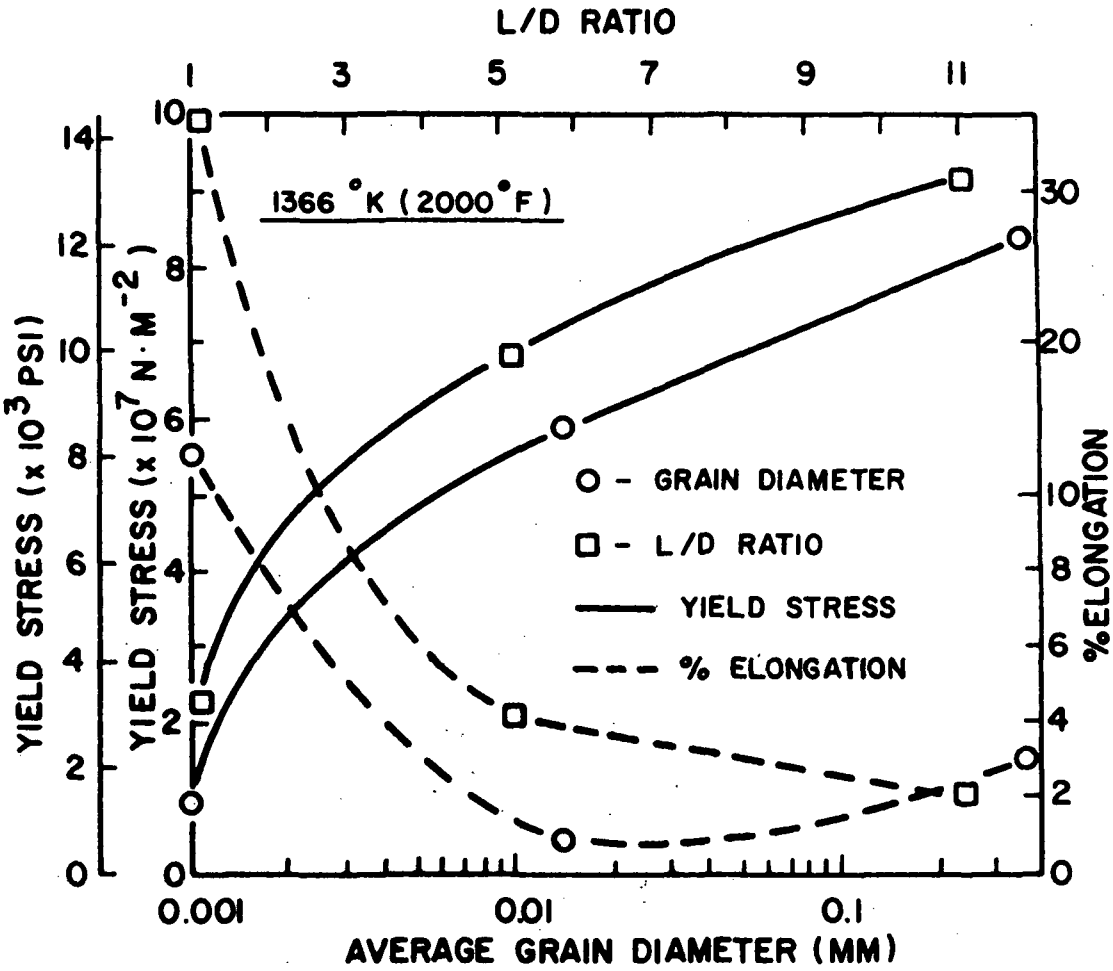

Figure 11 - Yield stress and % elongation versus average grain diameter and L/D ratio at 1366°K (2000°F).

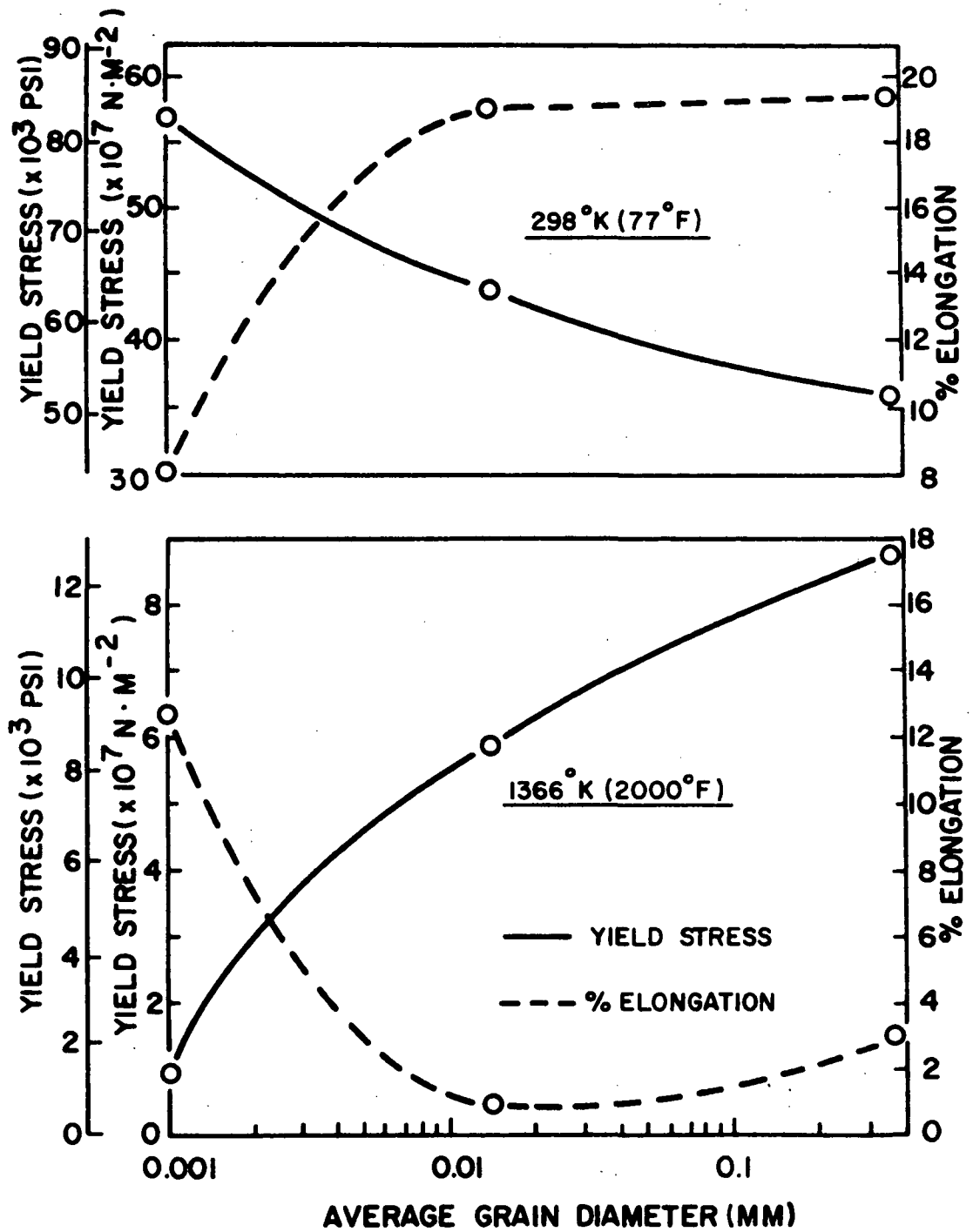

Figure 12 - Comparison of yield stress and % elongation trends with average grain diameter at 298°K (77°F) and 1366°K (2000°F).

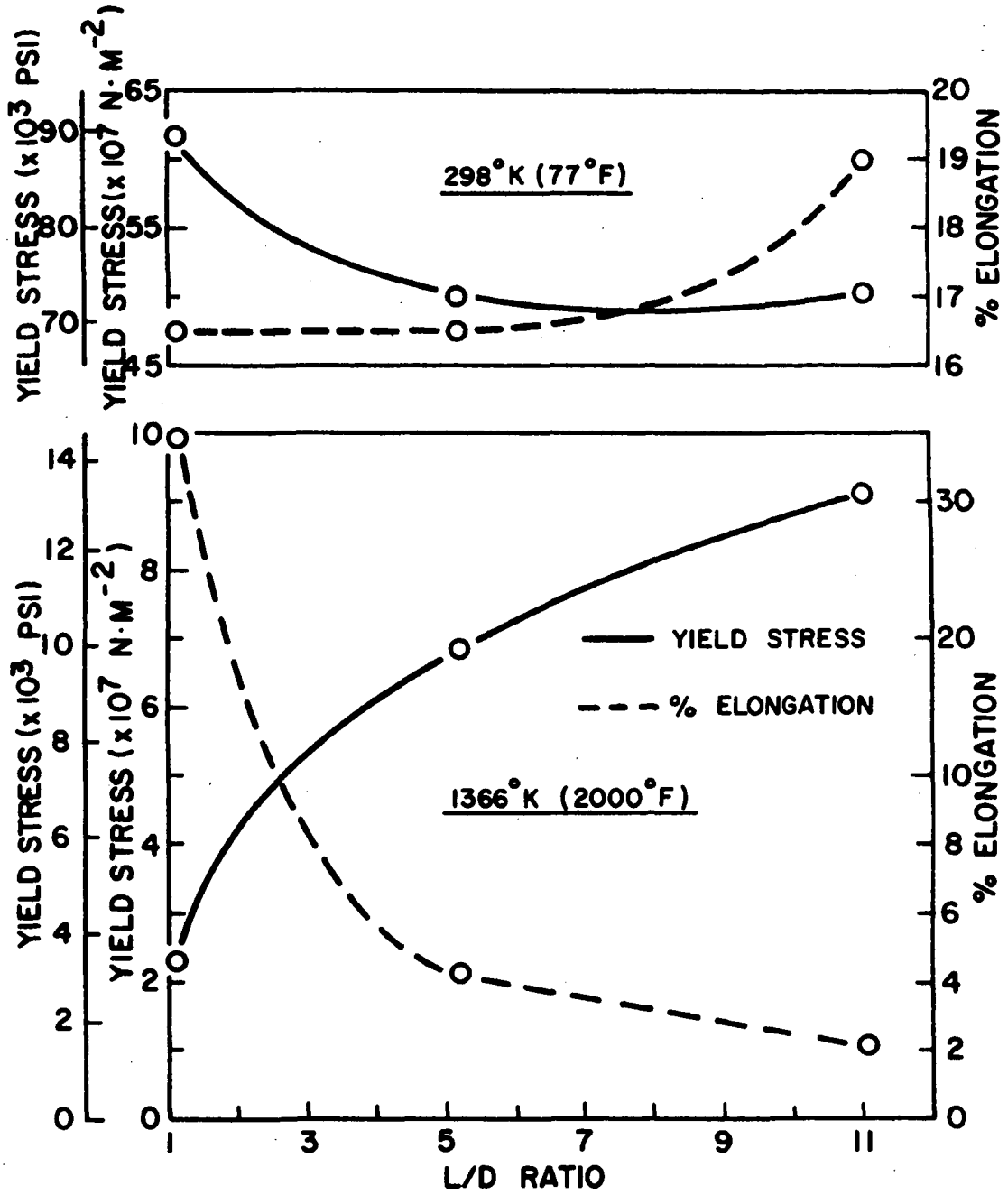

Figure 13 - Comparison of yield stress and % elongation trends with L/D ratio at 298°K (77°F) and 1366°K (2000°F).

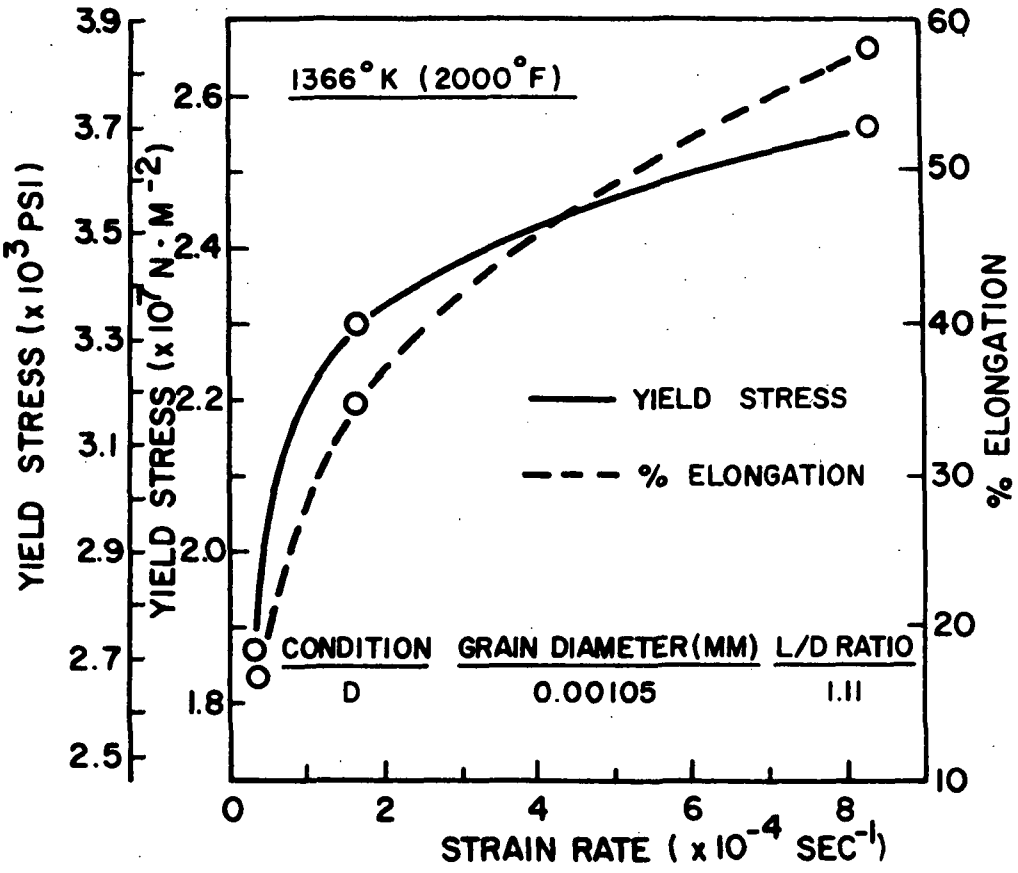

Figure 14 - Effect of tensile strain rate on yield stress and % elongation for Condition D at 1366°K (2000°F).

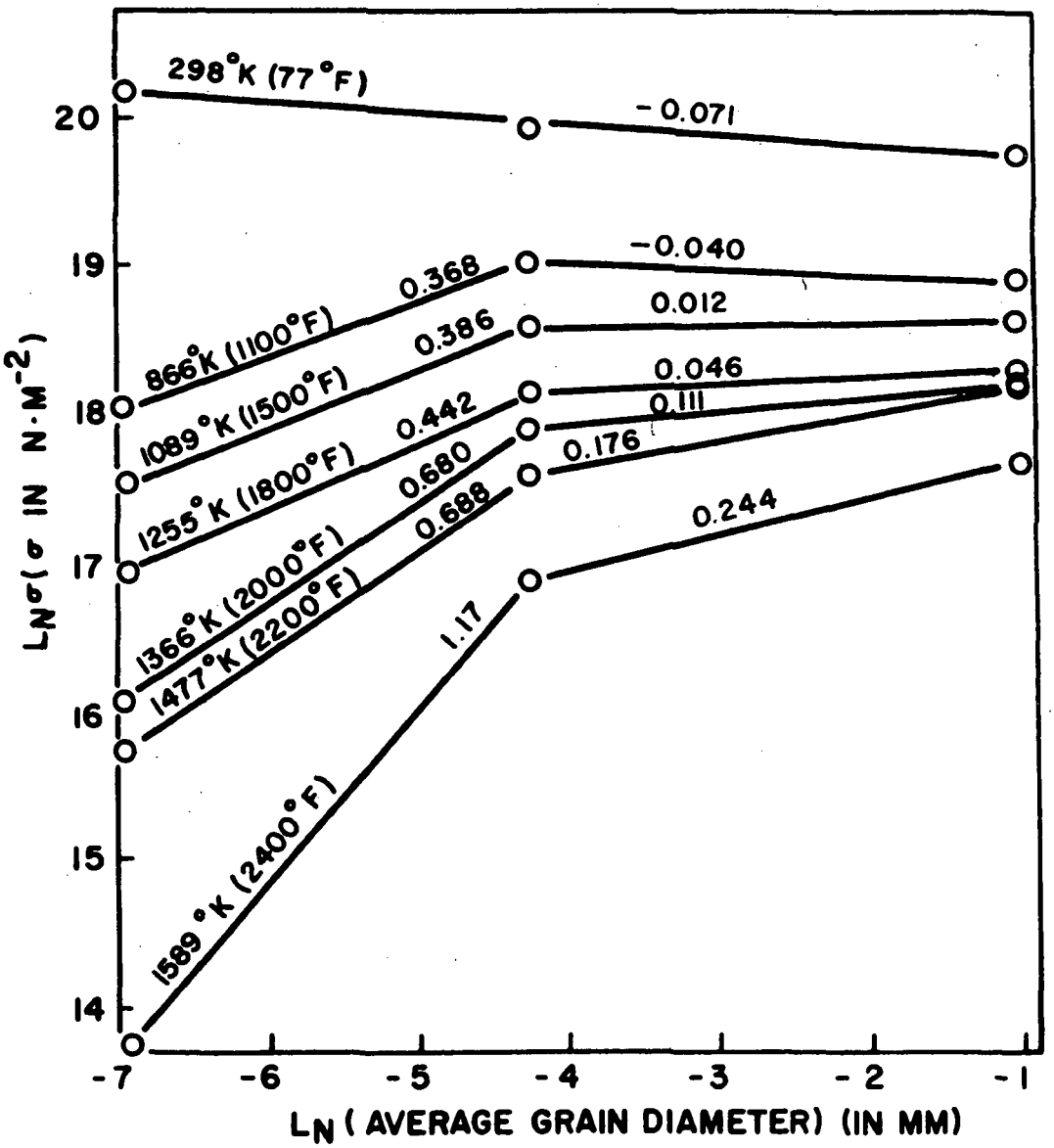

Figure 15 - Ln(yield stress) versus Ln(average grain diameter) at various temperatures.

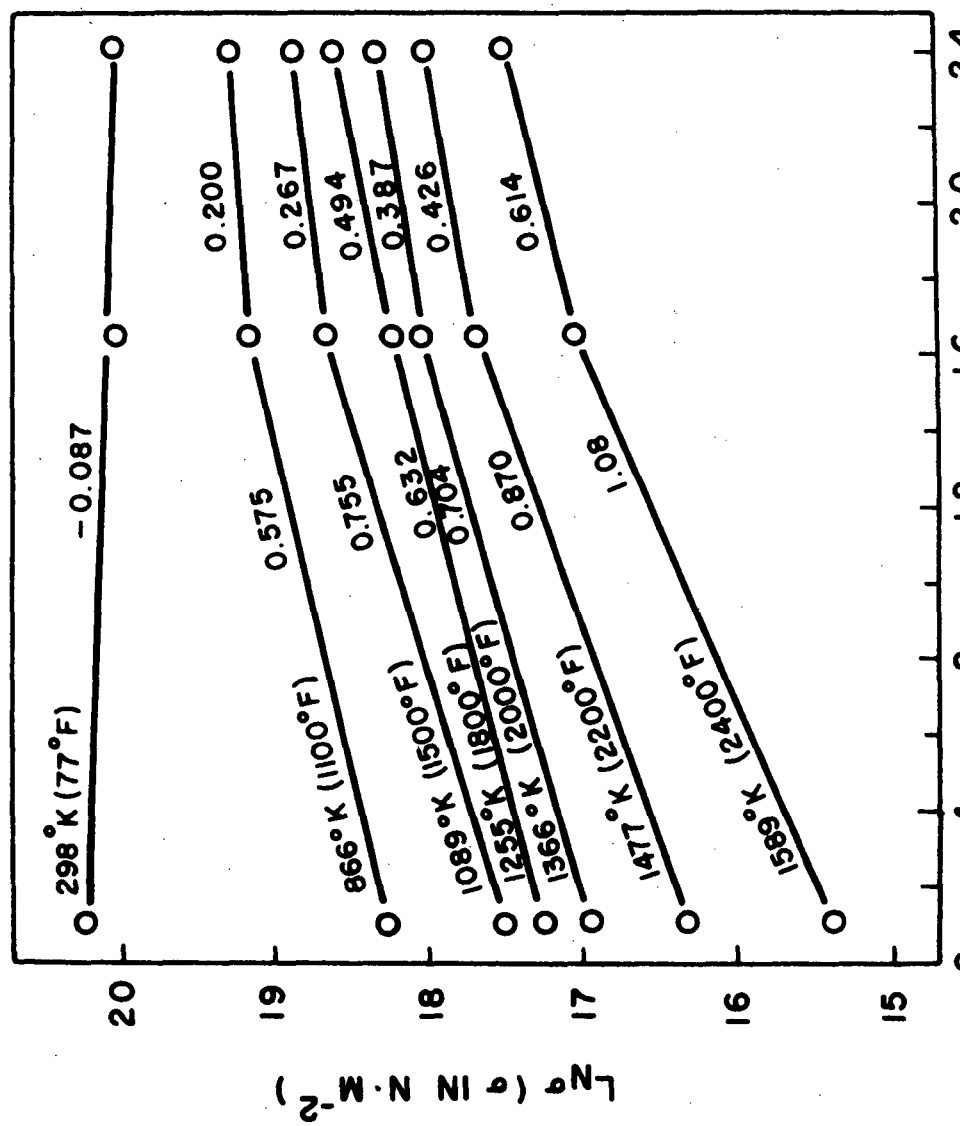

Figure 16 - Ln(yield stress) versus Ln(L/D ratio) at various temperatures.

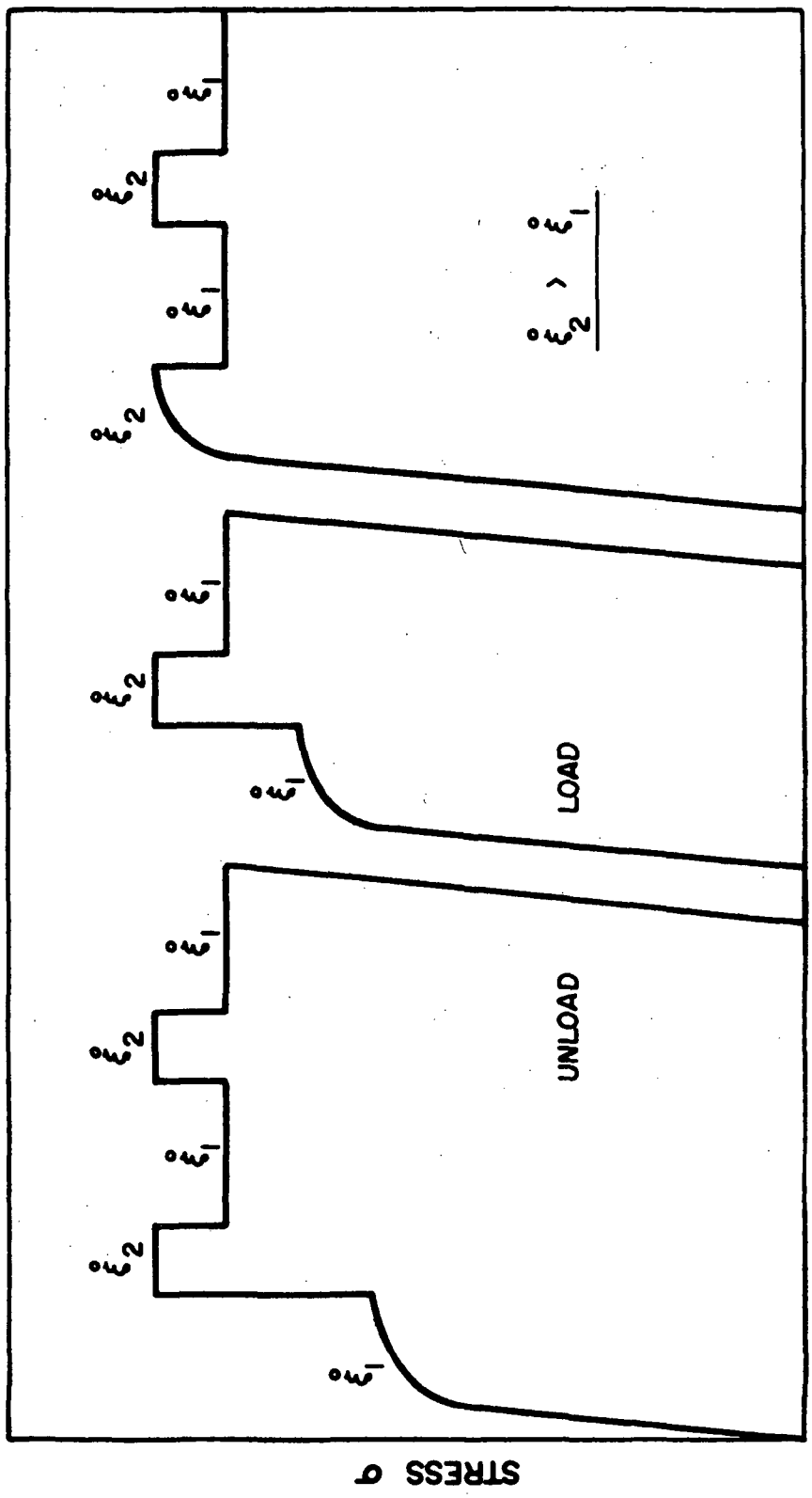

Figure 17 - Schematic description of differential strain rate change transient behavior.

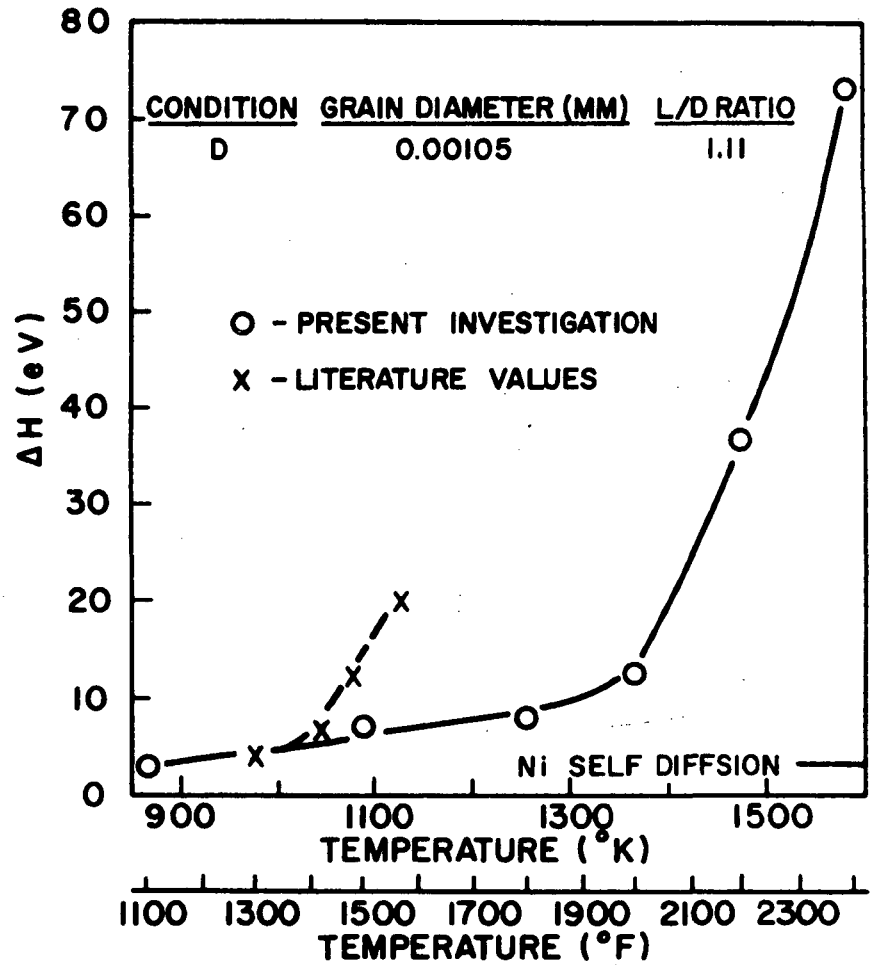

Figure 18 - Activation enthalpy versus temperature for Condition D. ΔH was calculated from Equation 13. Literature values are from Reference (5).

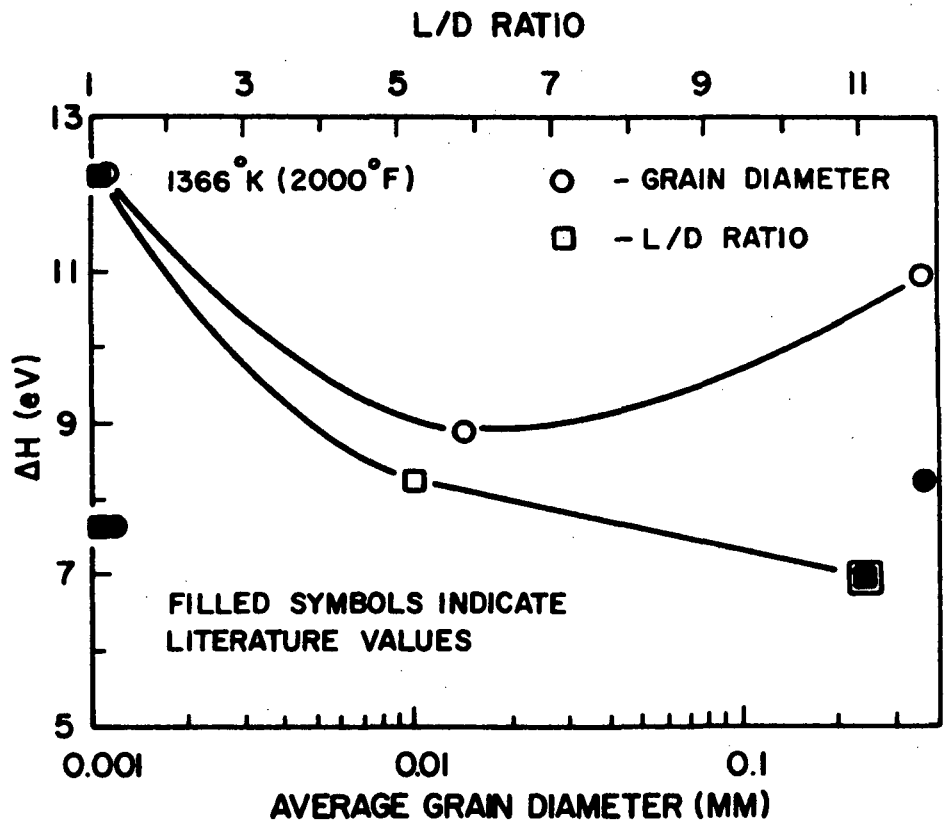

Figure 19 - Activation enthalpy at 1366°K (2000°F) versus average grain diameter and L/D ratio. ΔH was calculated from Equation 13. Literature values are from Reference (1).

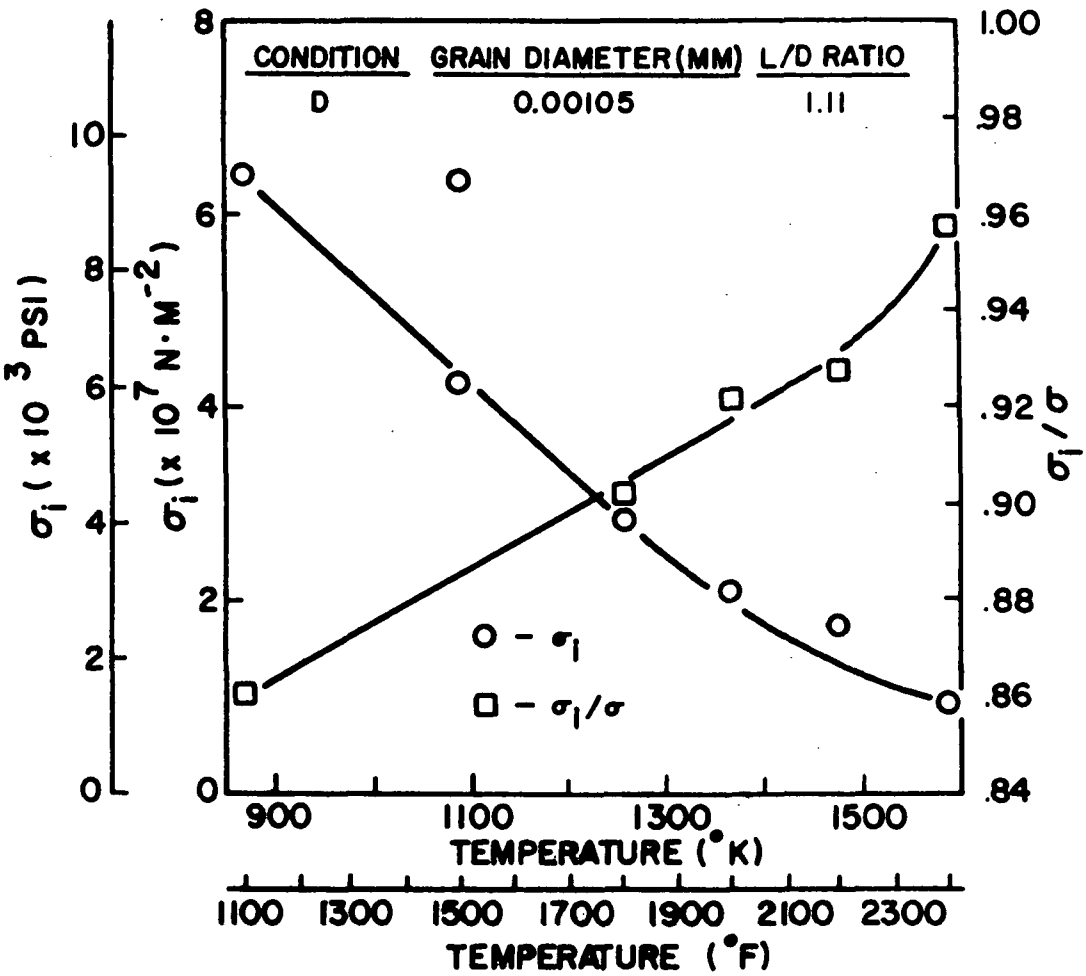

Figure 20 - Internal stress σ_i and internal stress-to-applied stress ratio σ_i/σ versus temperature for Condition D.

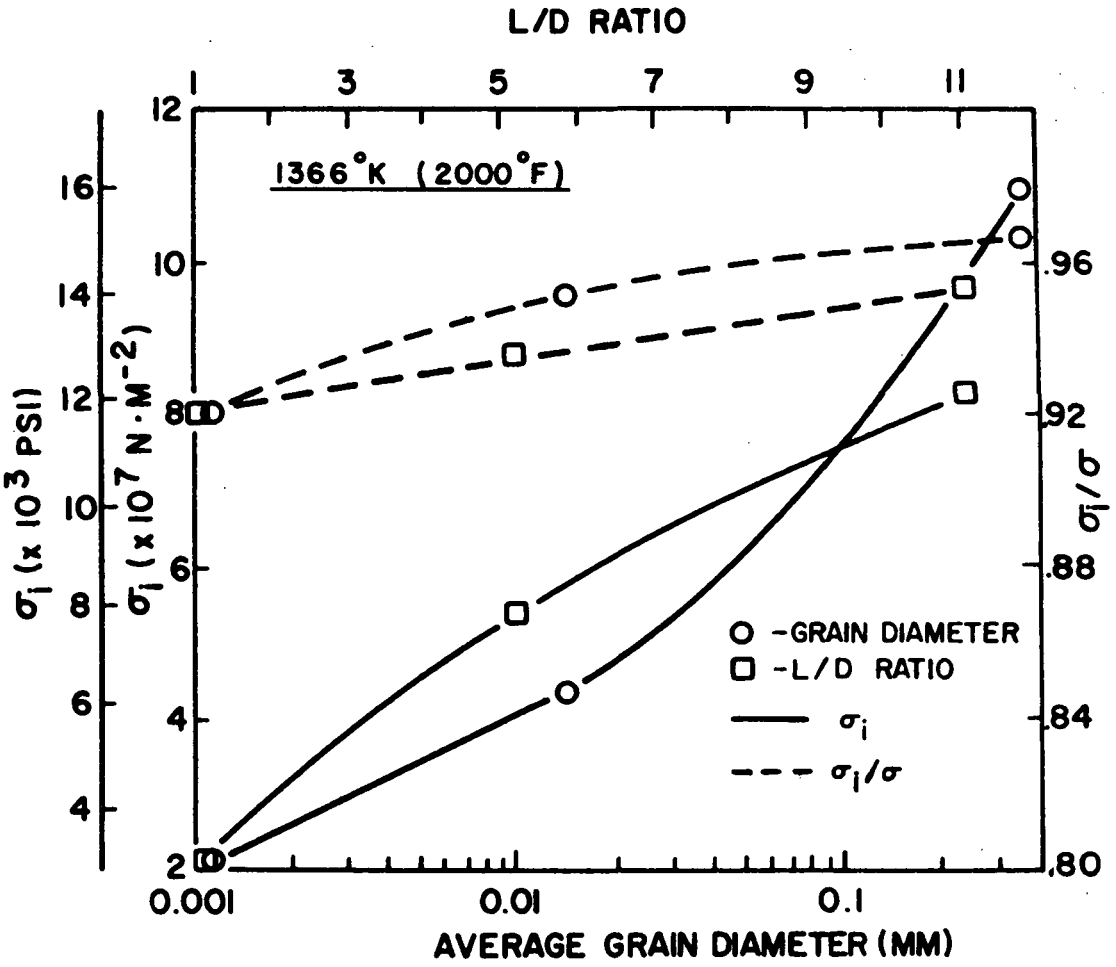

Figure 21 - Internal stress σ_i and internal stress-to-applied stress ratio σ_i/σ versus average grain diameter and L/D ratio at 1366°K (2000°F).

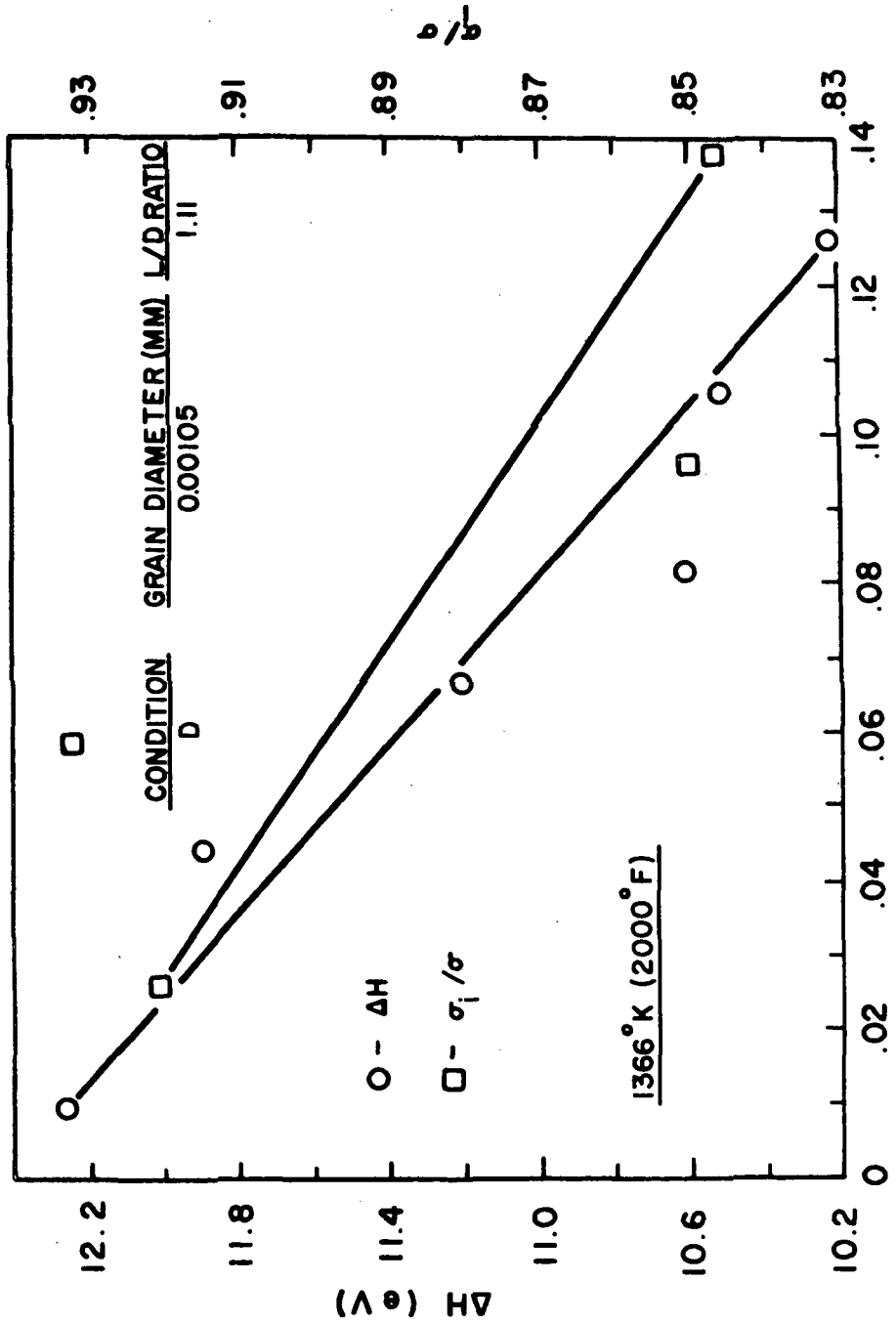

Figure 22 - ΔH and σ_i/σ versus strain for Condition D at 1366°K (2000°F).

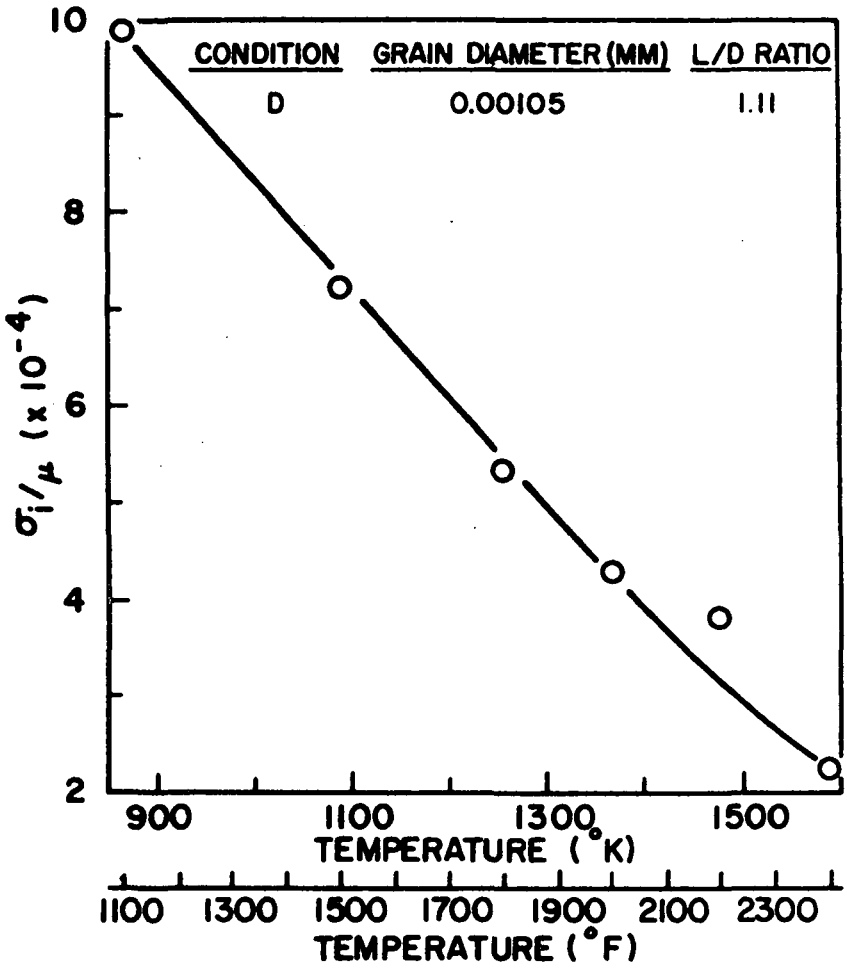

Figure 23 - Internal stress-to-shear modulus ratio σ_i/μ versus temperature for Condition D.

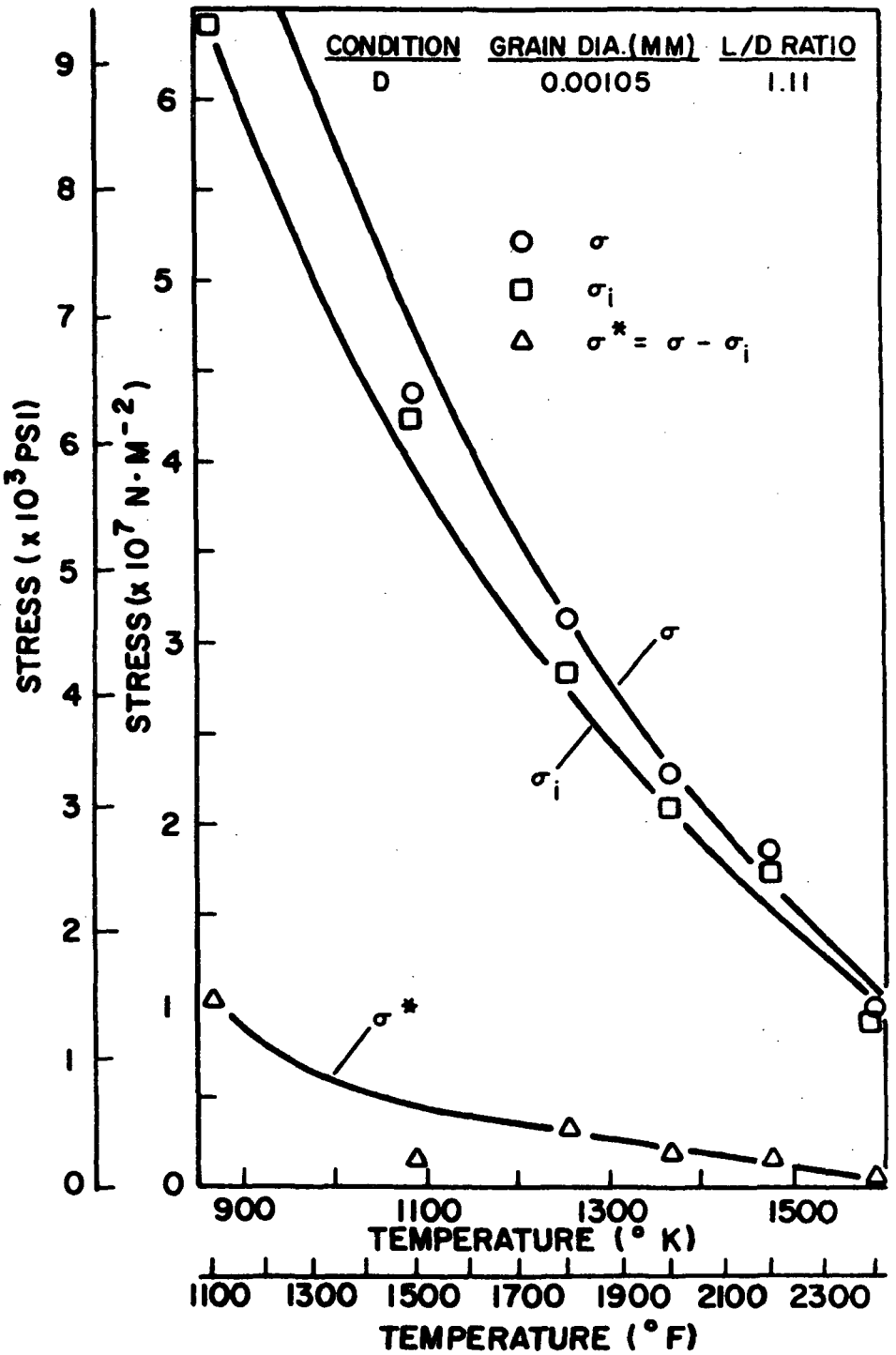

Figure 24 - Effective stress σ^* versus temperature for Condition D.

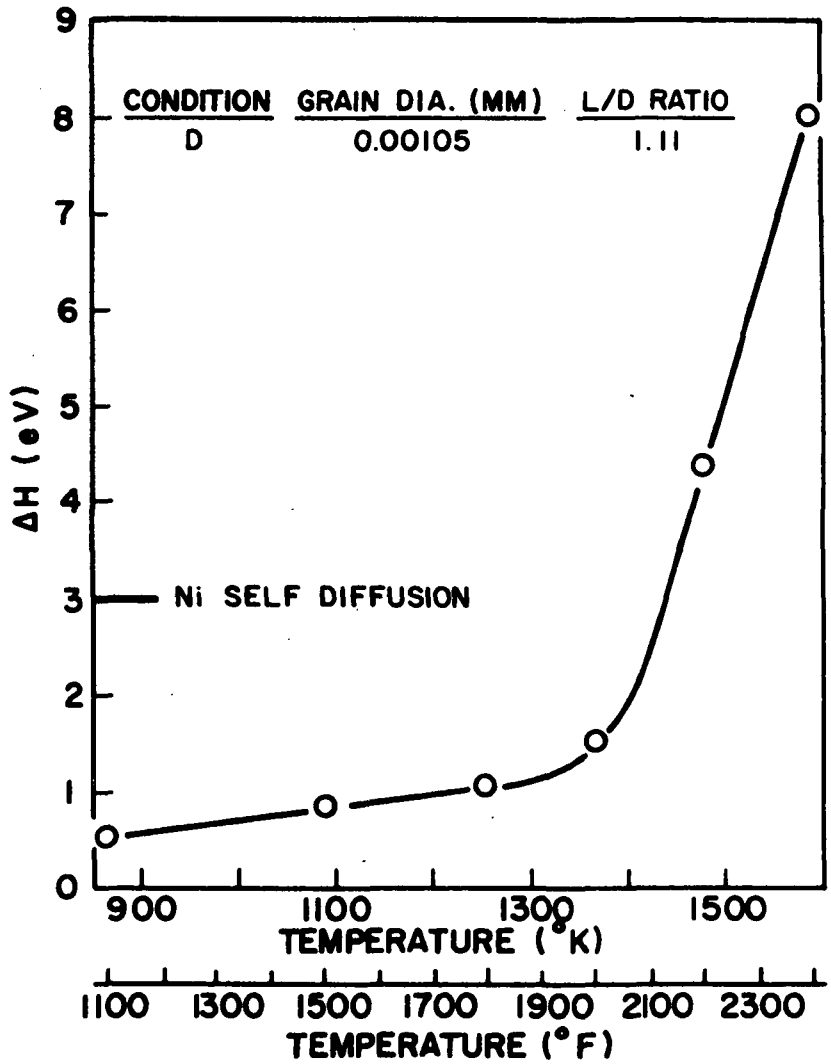

Figure 25 - Activation enthalpy versus temperature for Condition D. ΔH was calculated from Equation 11, using the data in Figure 24.

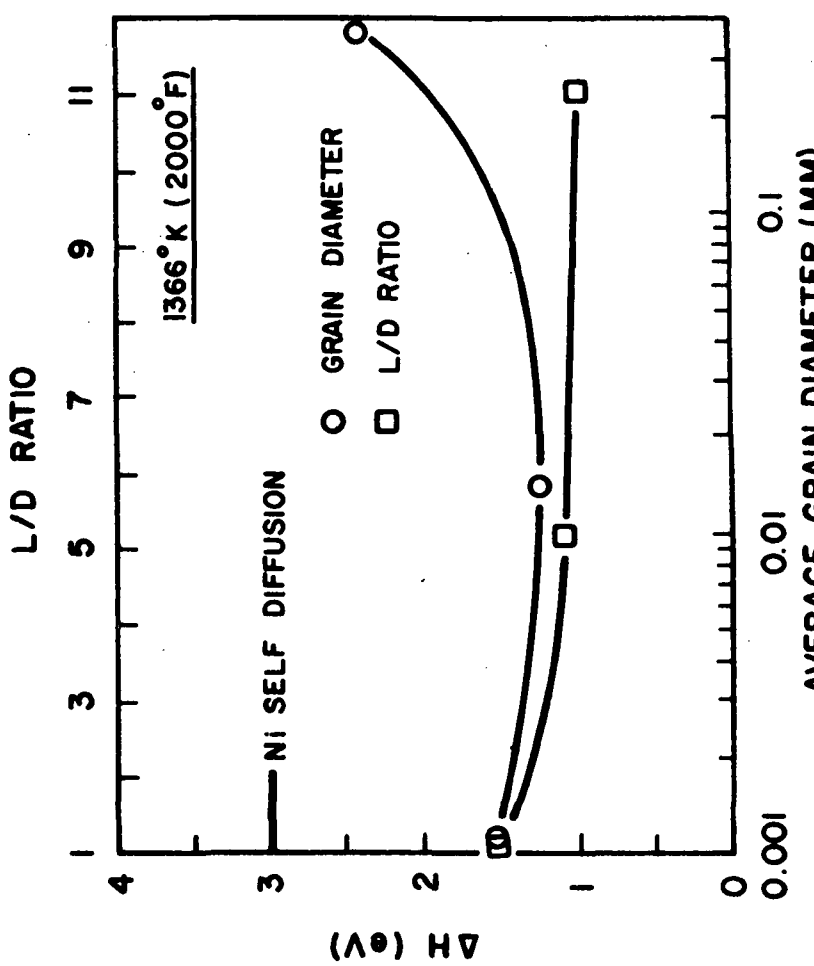

Figure 26 - Activation enthalpy at 1366°K (2000°F) versus average grain diameter and L/D ratio. ΔH was calculated from Equation 11.

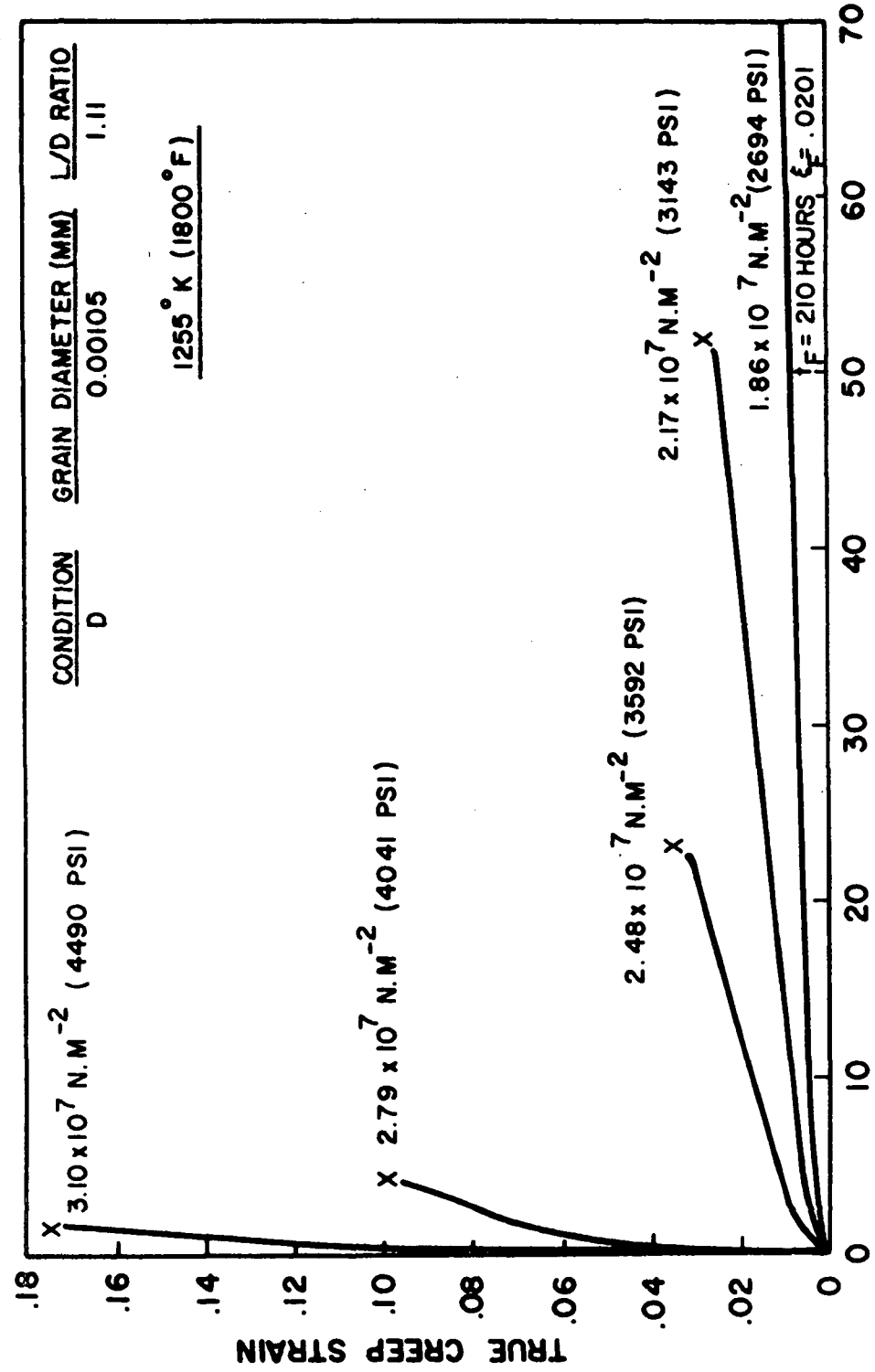

Figure 27 - Creep curves at 1255°K (1800°F) for Condition D at various stress levels.

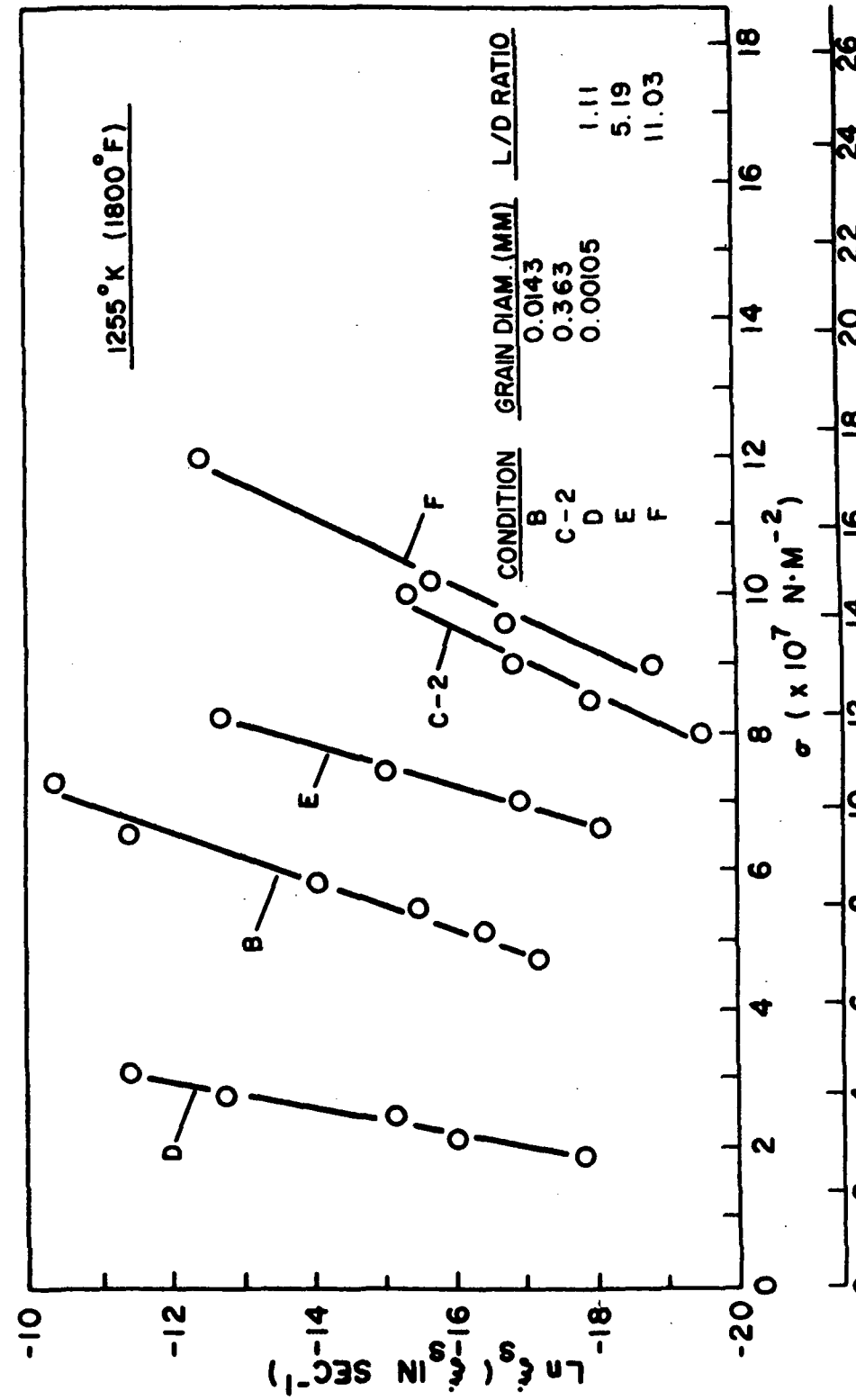

Figure 28 - Ln(steady state creep rate) versus stress for various material conditions. Straight lines are least squares fits of the data.

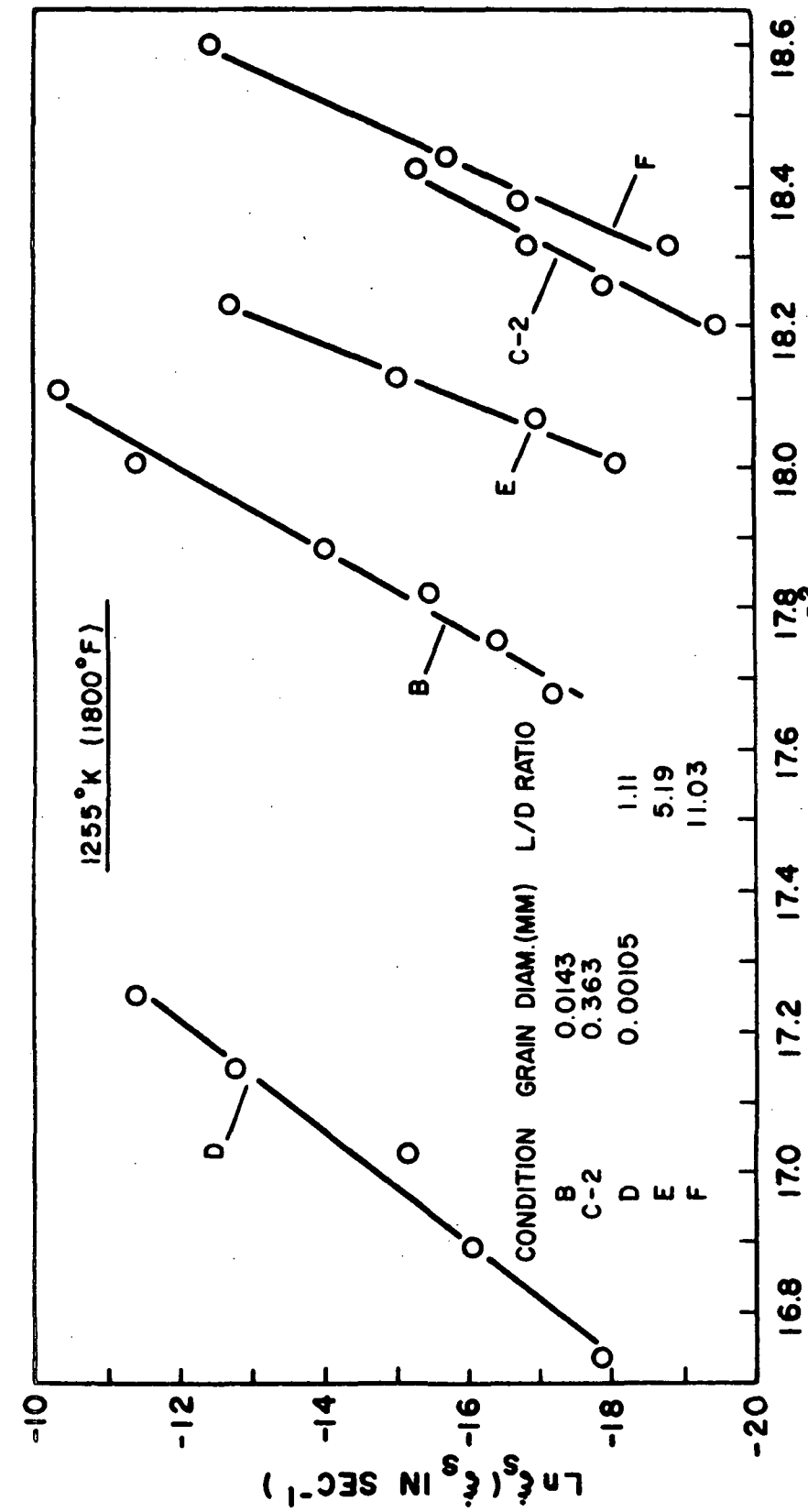

Figure 29 - Ln(steady state creep rate) versus Ln(stress) for various material conditions. Straight lines are least squares fits of the data.

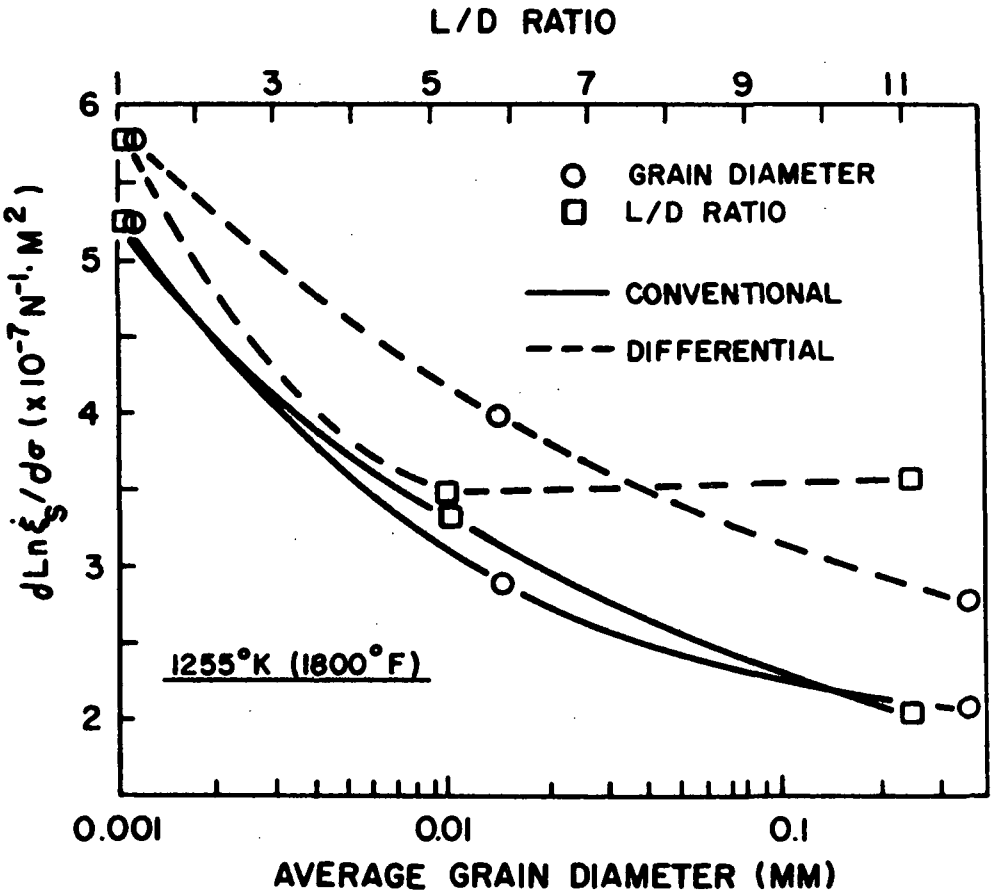

Figure 30 - $d\ln\dot{\varepsilon}_s/d\sigma$ versus average grain diameter and L/D ratio, for both conventional and differential tests. Conventional values are from Figure 28.

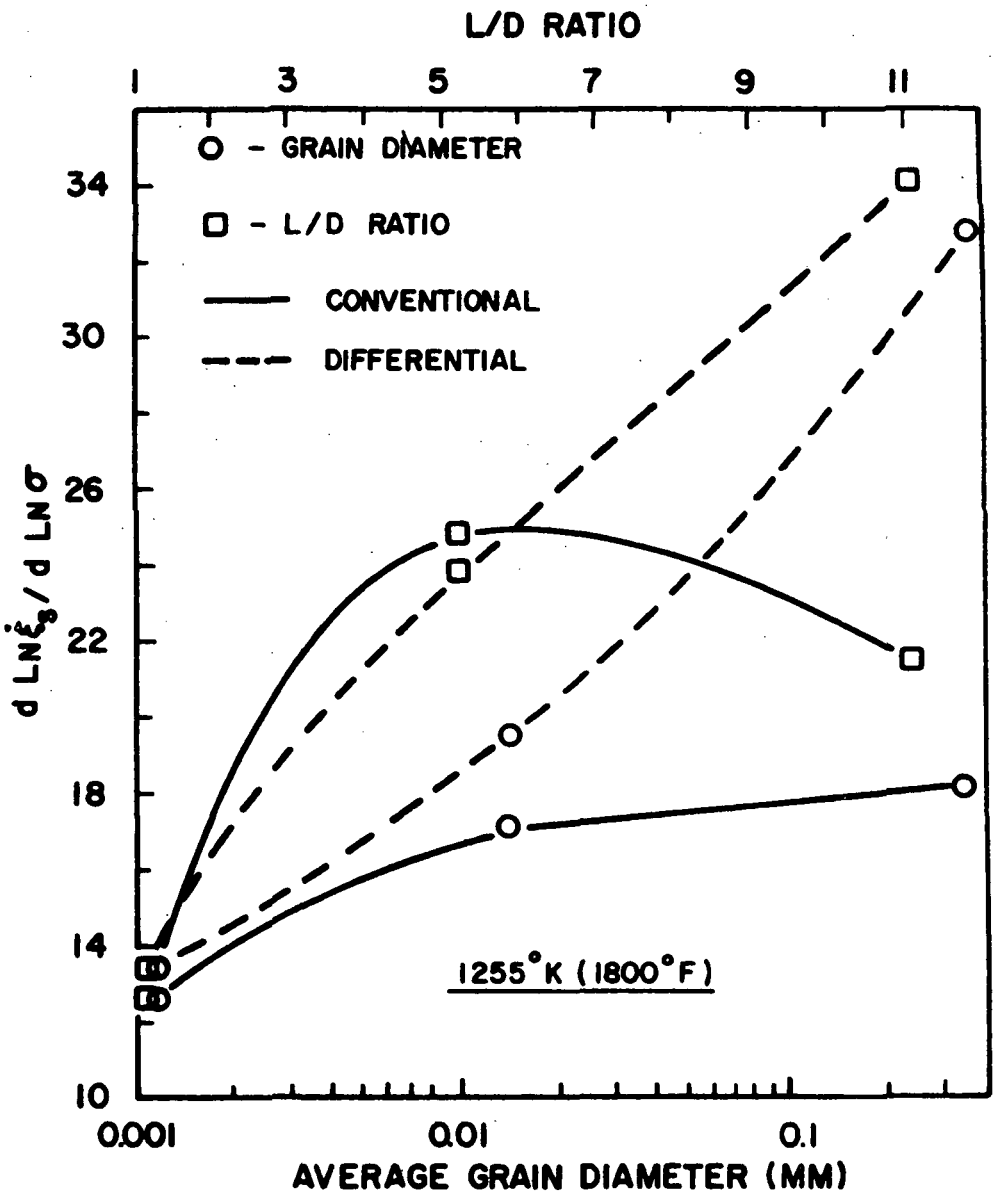

Figure 31 - $d\ln\dot{\varepsilon}_s/d\ln\sigma$ versus average grain diameter and L/D ratio, for both conventional and differential tests. Conventional values are from Figure 29.

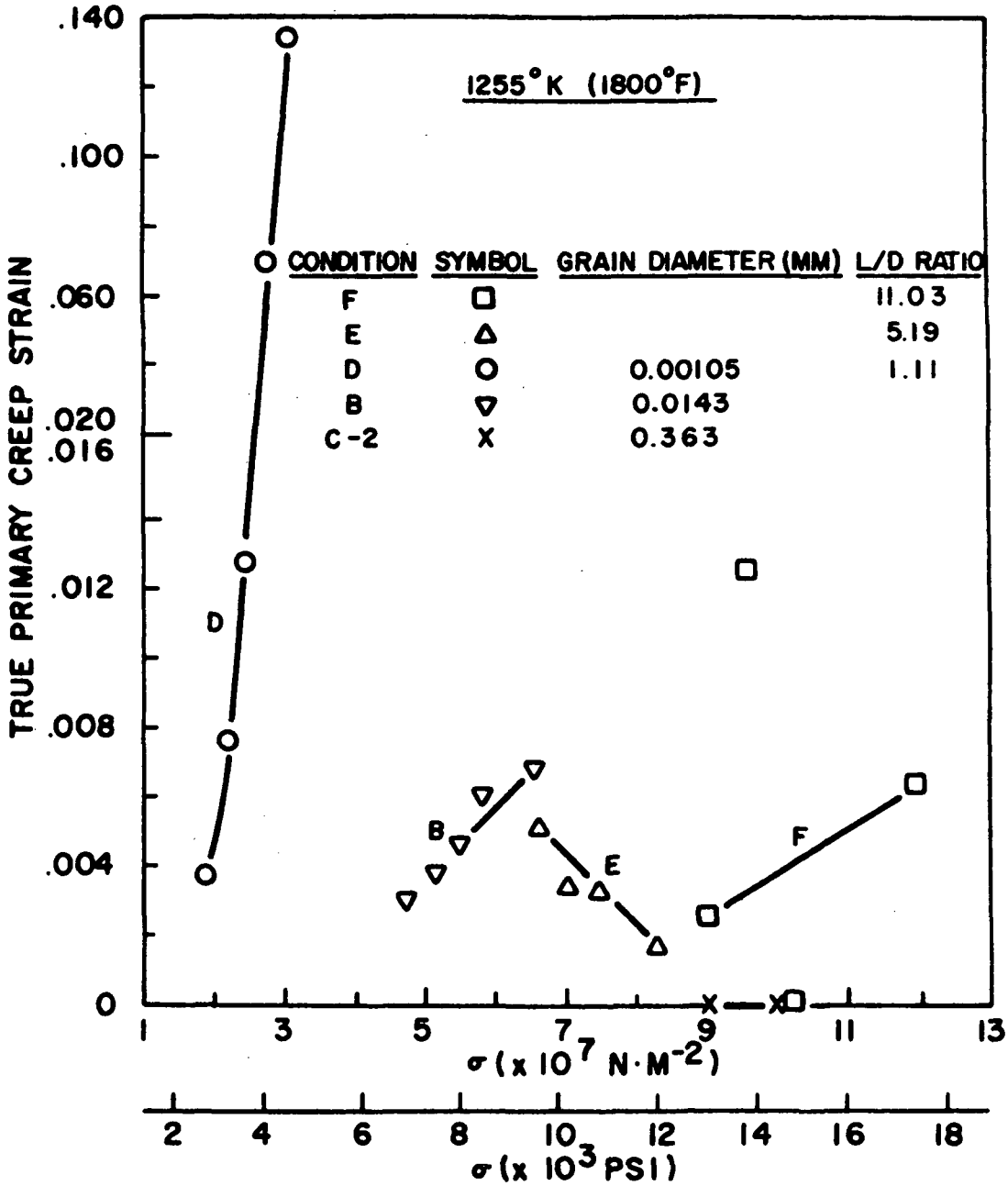

Figure 32 - True primary creep strain versus stress for various material conditions.

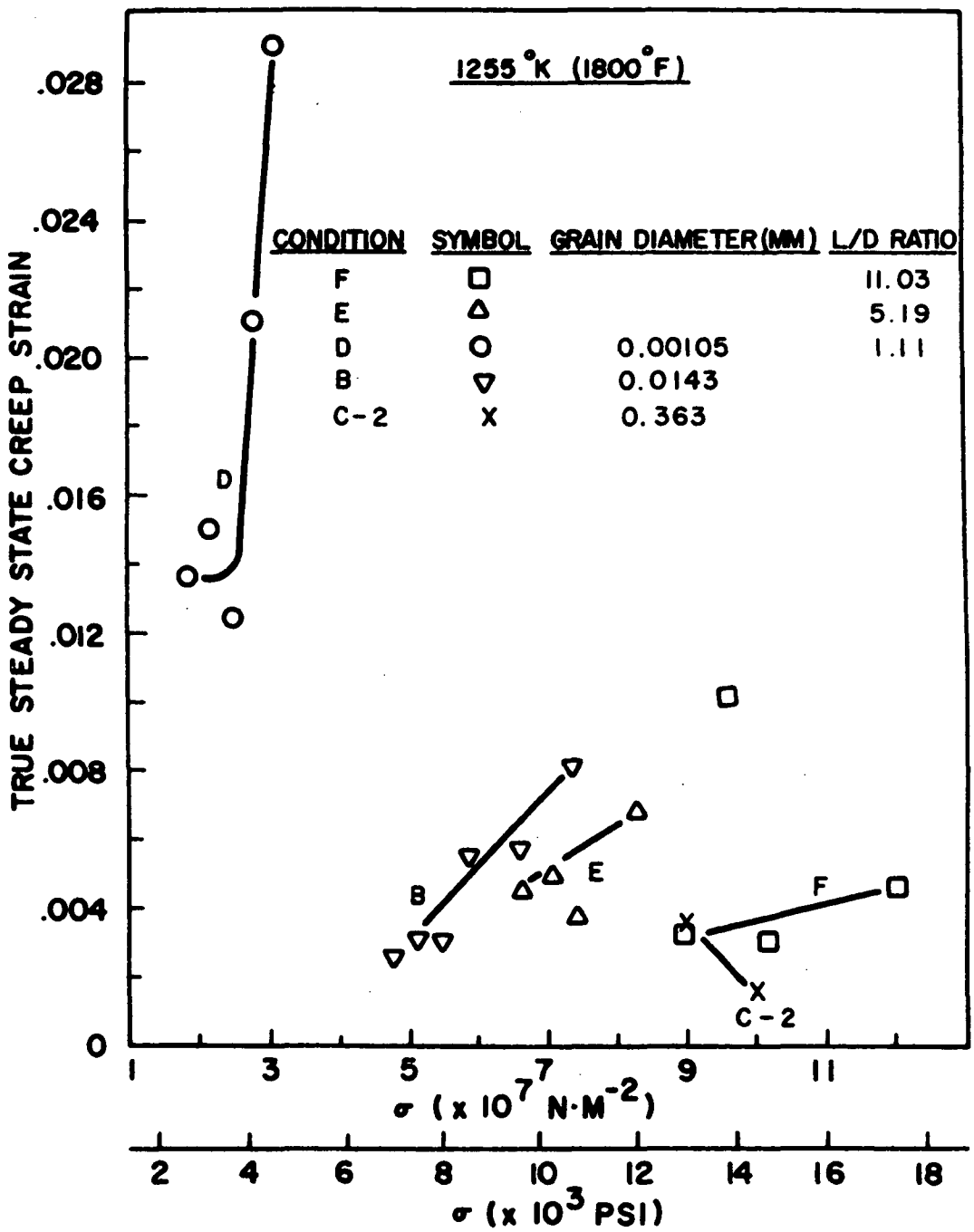

Figure 33 - True steady state creep strain versus stress for various material conditions.

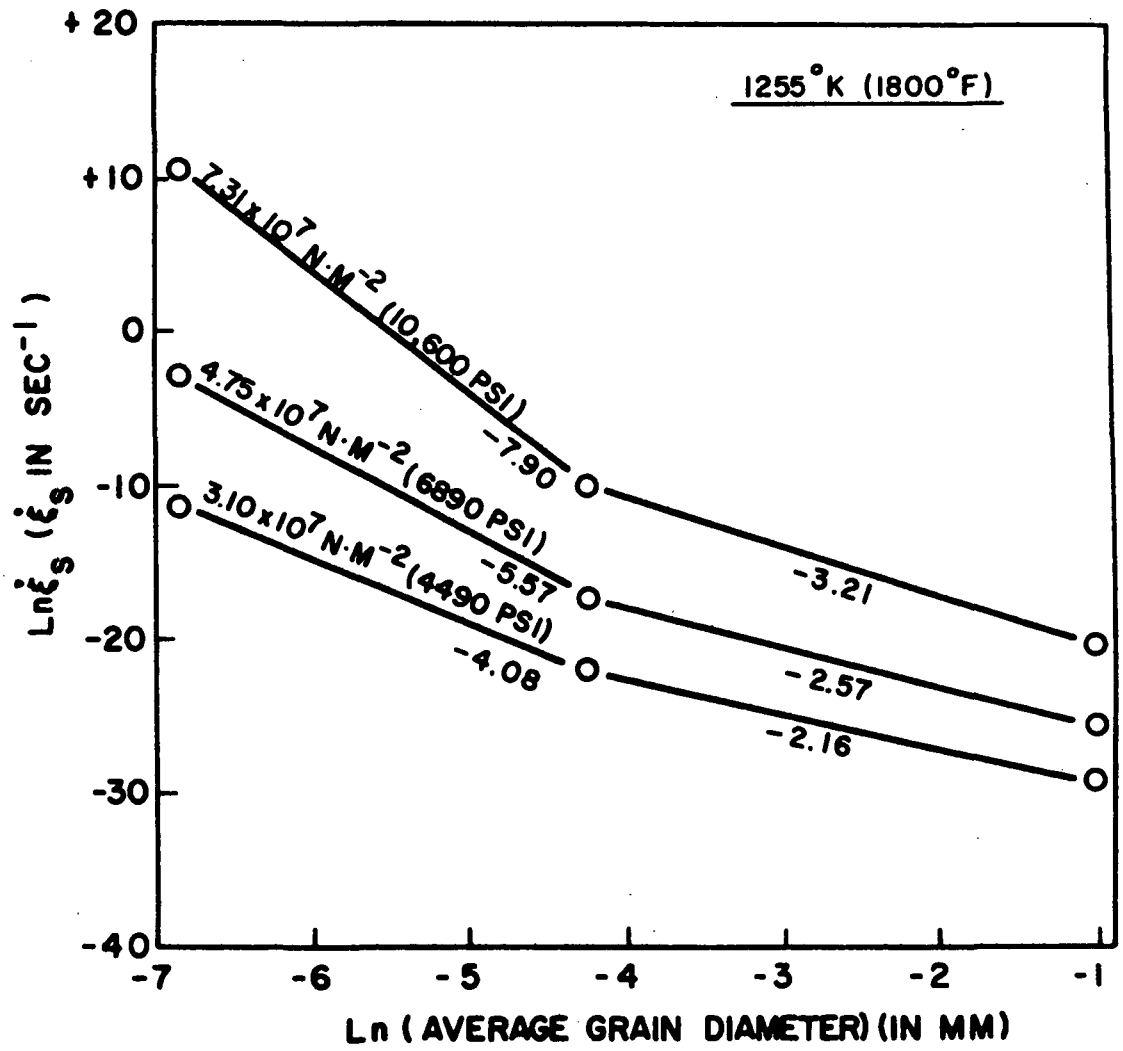

Figure 34 - Ln(steady state creep rate) versus Ln(average grain diameter) for various stress levels.

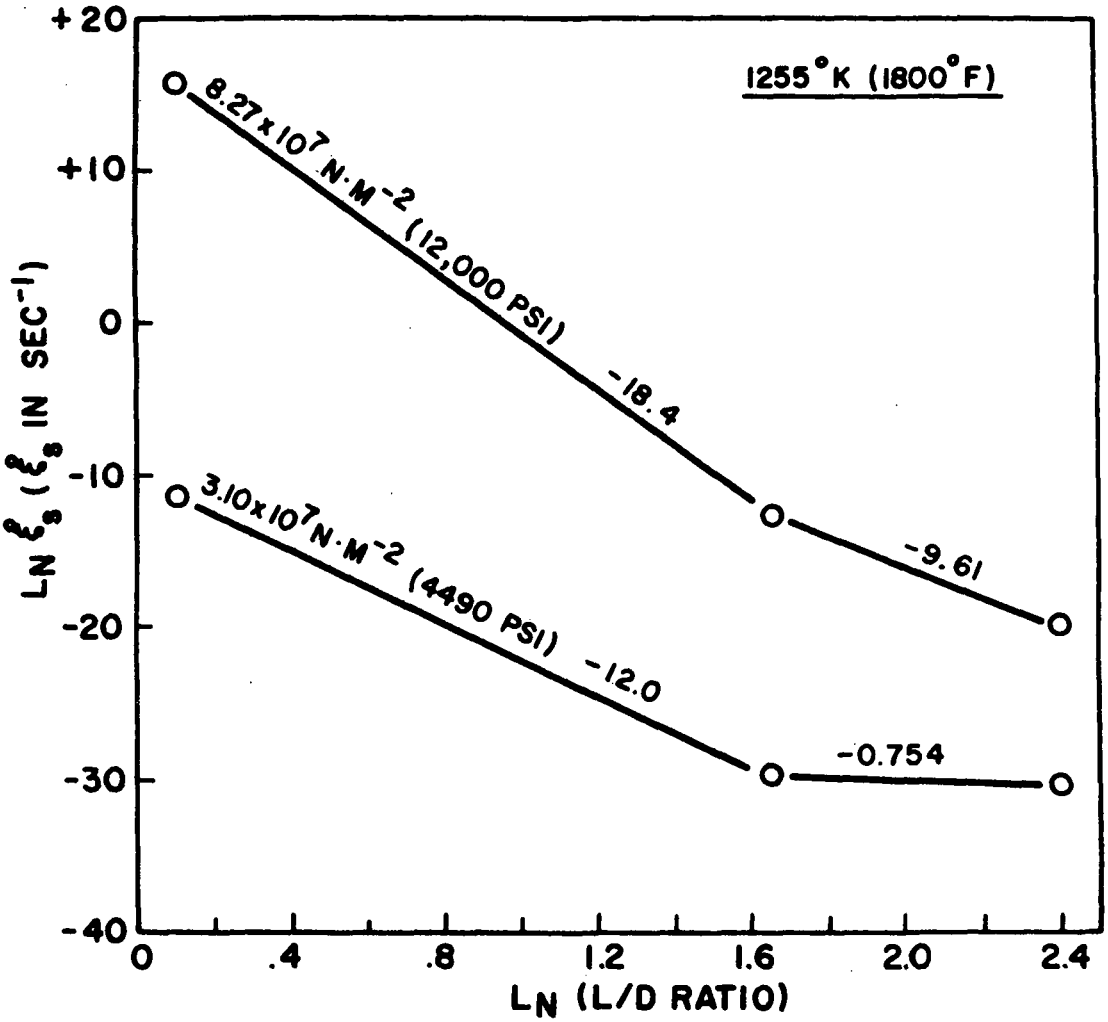

Figure 35 - Ln(steady state creep rate) versus Ln(L/D ratio) for various stress levels.

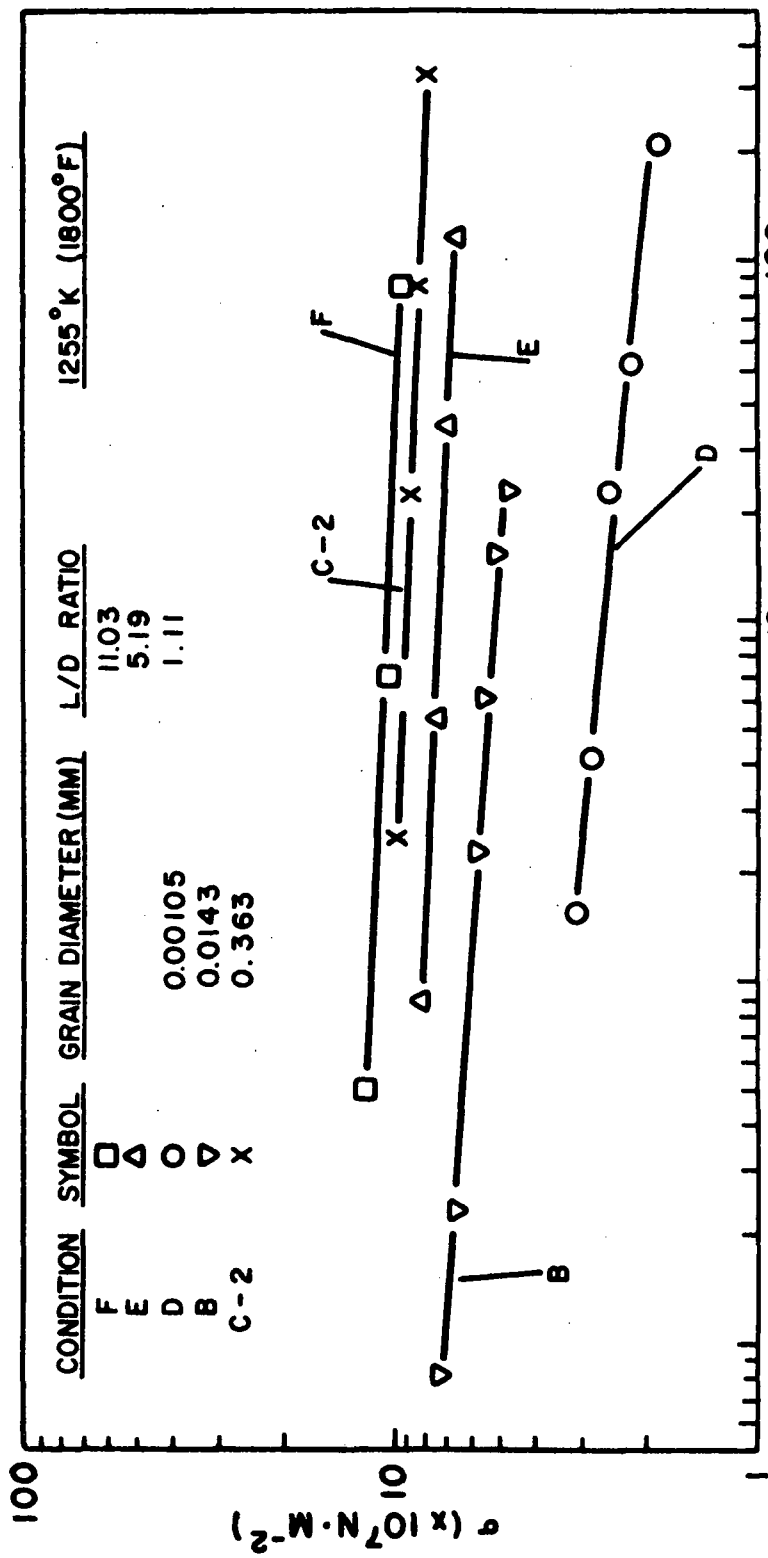

Figure 36 - Stress rupture behavior of various material conditions.

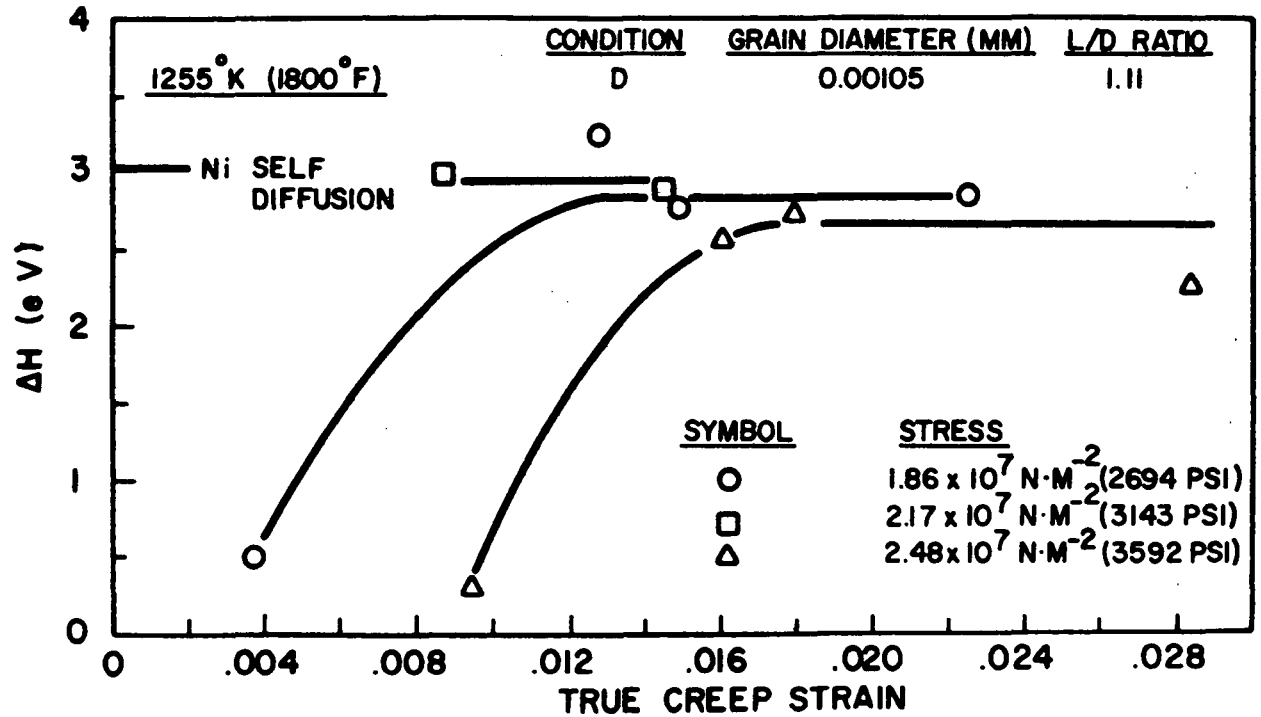

Figure 37 - Creep activation enthalpy versus strain for Condition D at various stress levels.

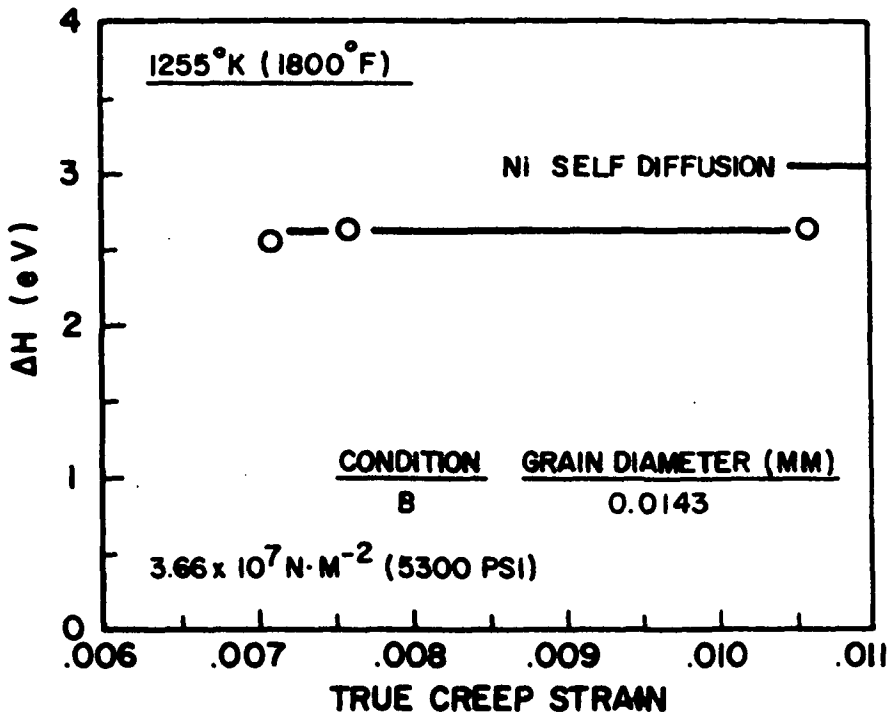

Figure 38 - Creep activation enthalpy versus strain for Condition B.

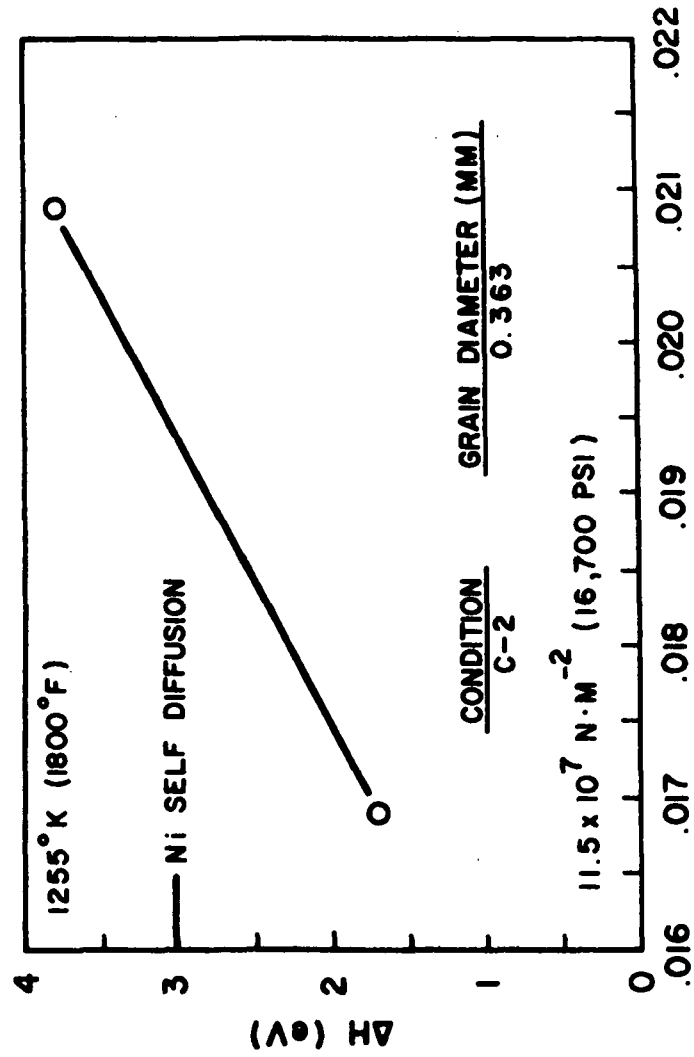

Figure 39 - Creep activation enthalpy versus strain for Condition C-2.

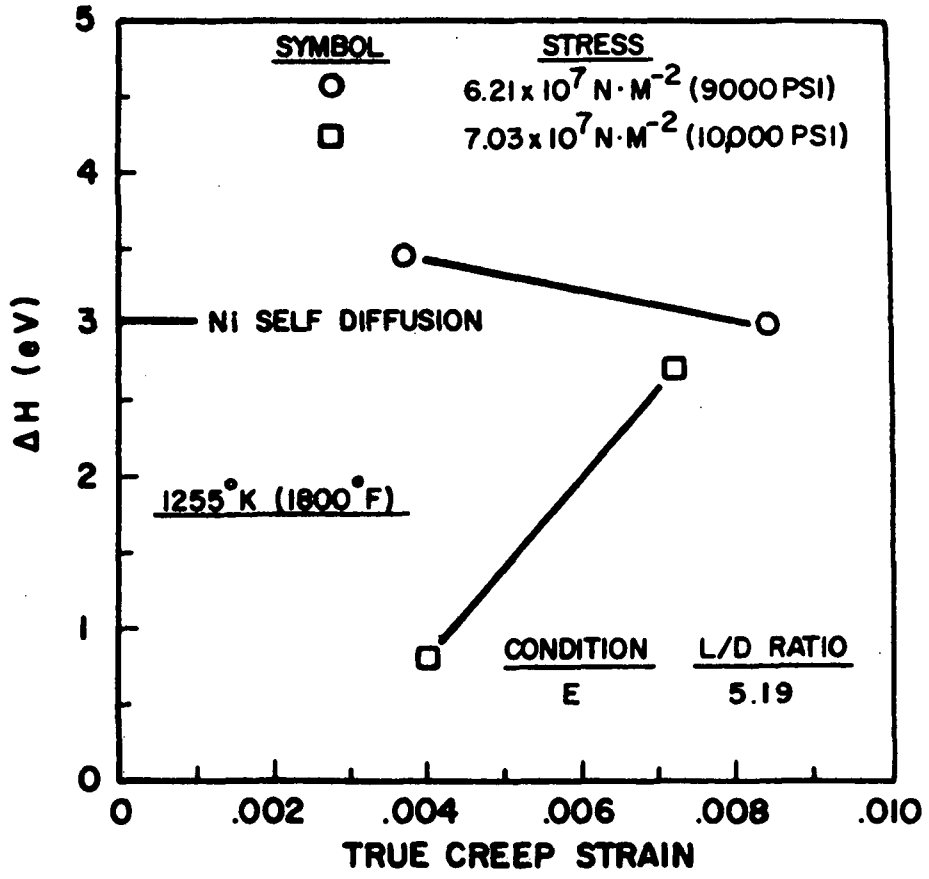

Figure 40 - Creep activation enthalpy versus strain for Condition E at various stress levels.

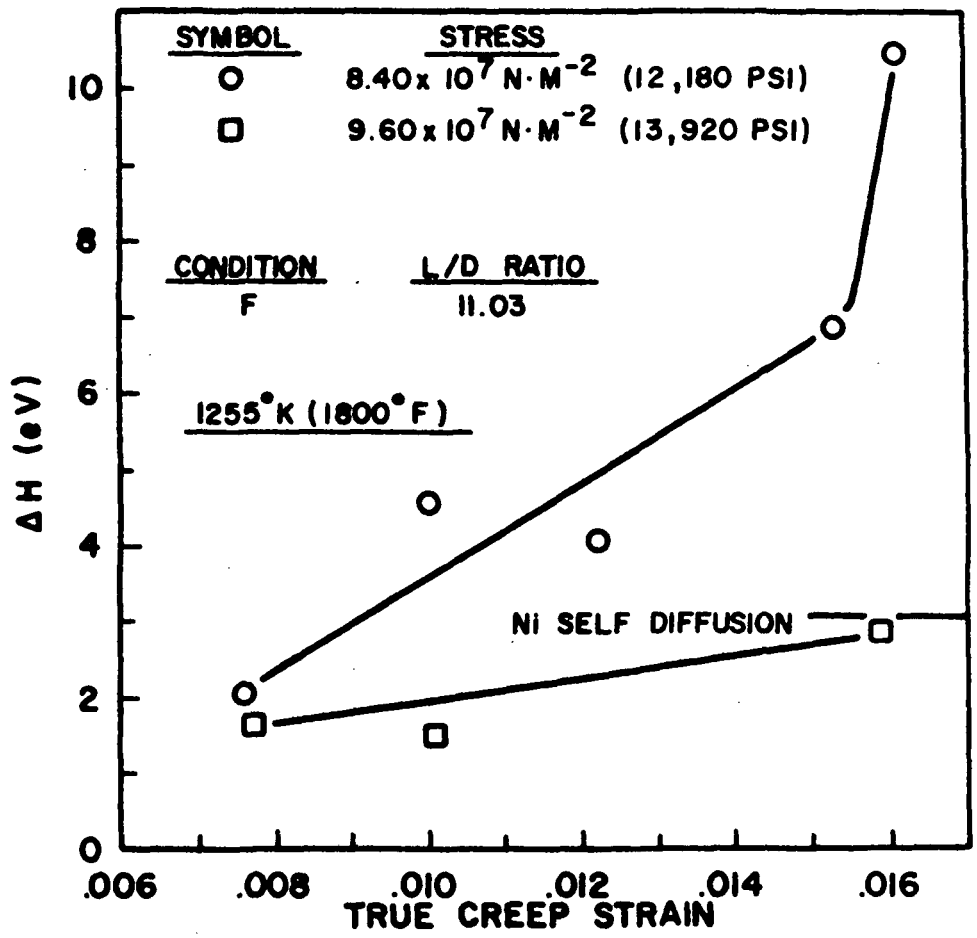

Figure 41 - Creep activation enthalpy versus strain for Condition F at various stress levels.

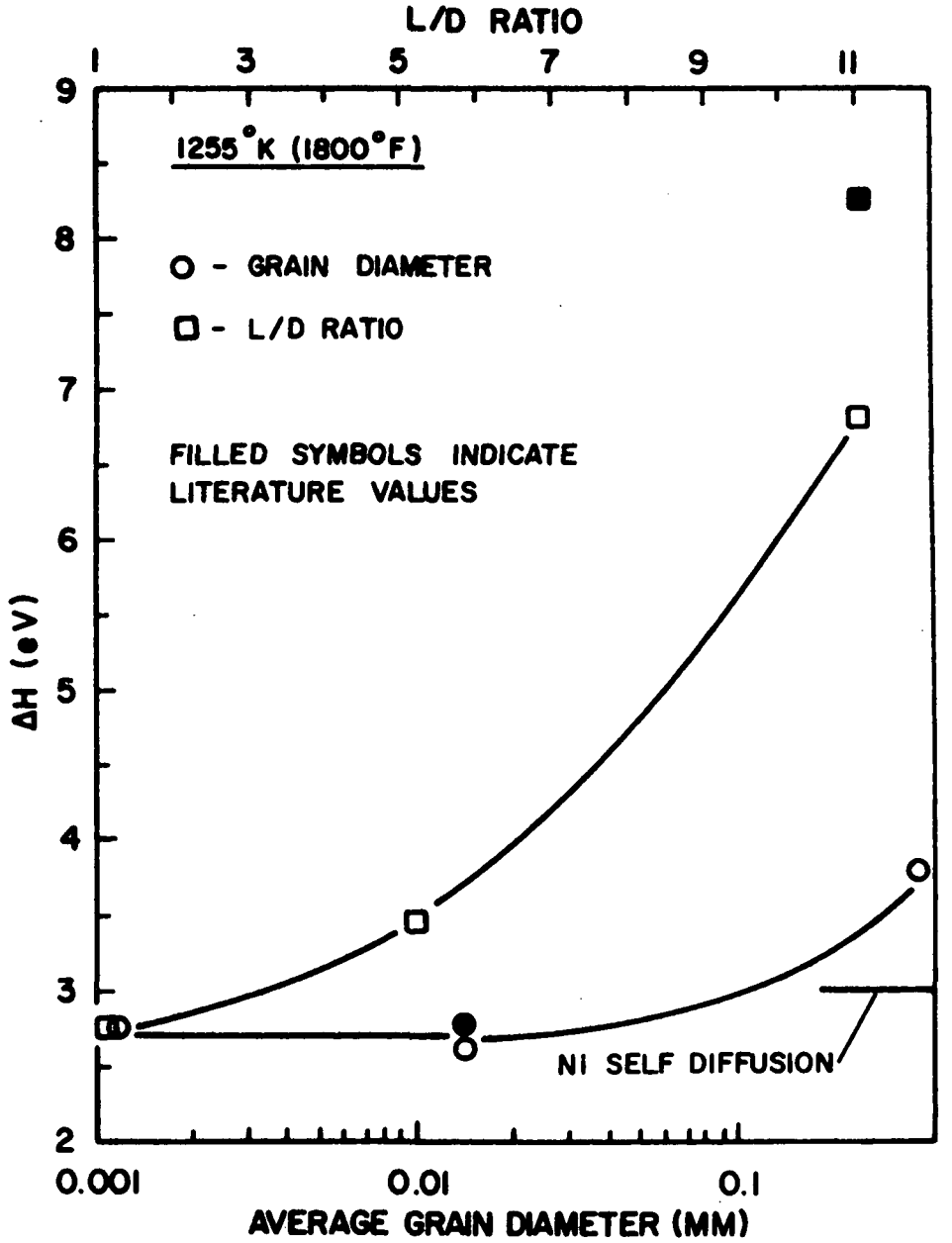

Figure 42 - Creep activation enthalpy versus average grain diameter and L/D ratio. ● is from Reference (7). ■ is from Reference (6).

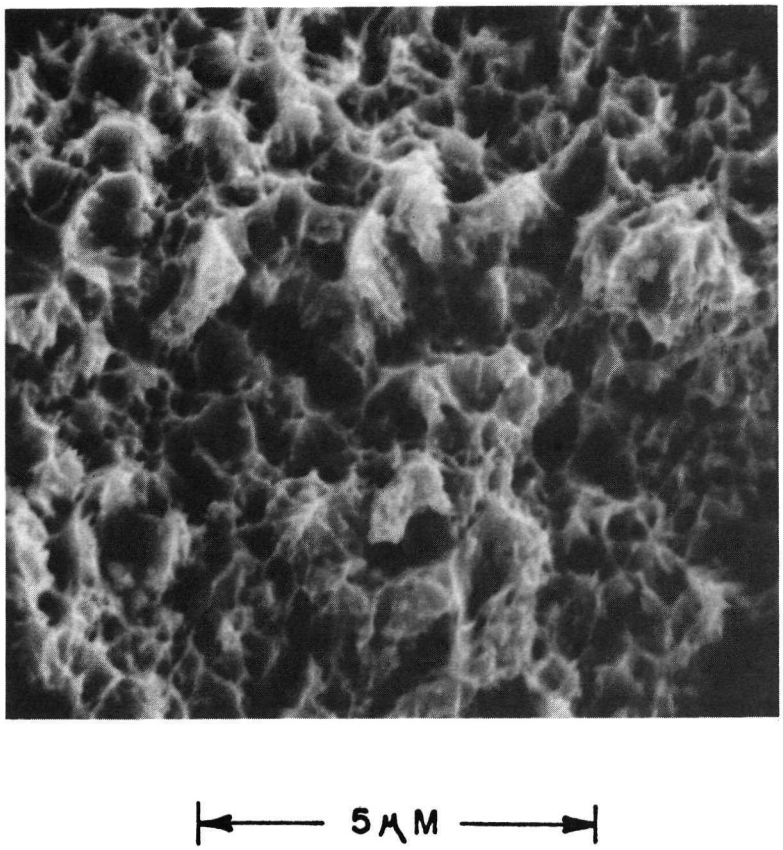

Figure 43 - Room temperature fracture surface of Condition D.

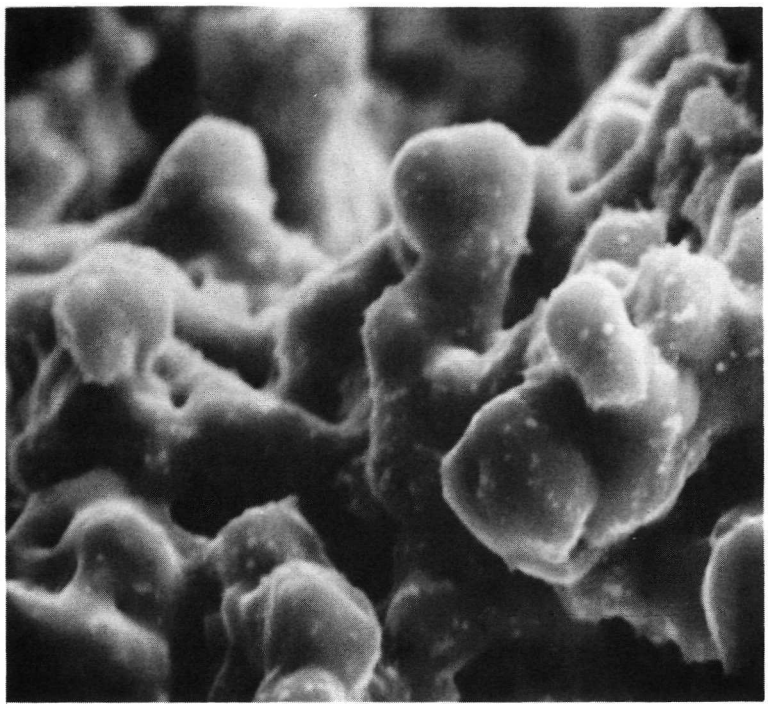

Figure 44 - Elevated temperature (1366°K (2000°F)) fracture surface of Condition D.

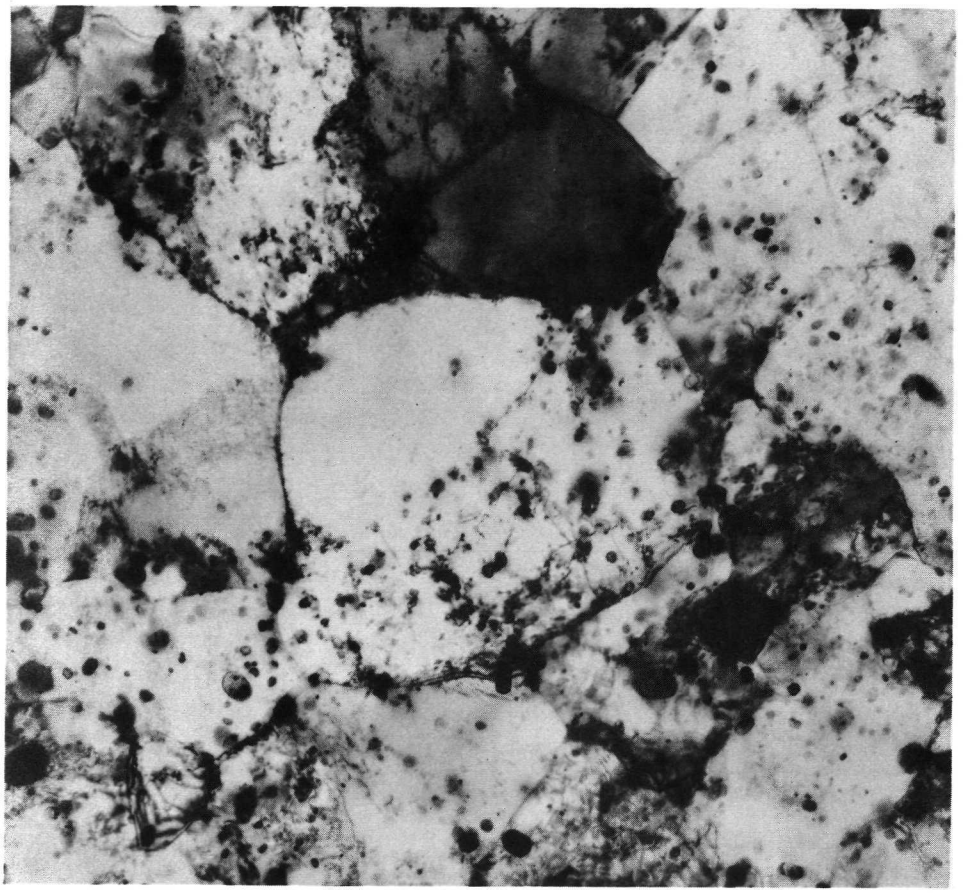

Figure 45 - Changes in the thoria particle distribution due to elevated temperature tensile deformation. No crystallographic boundary separates the low and high thoria density regions.

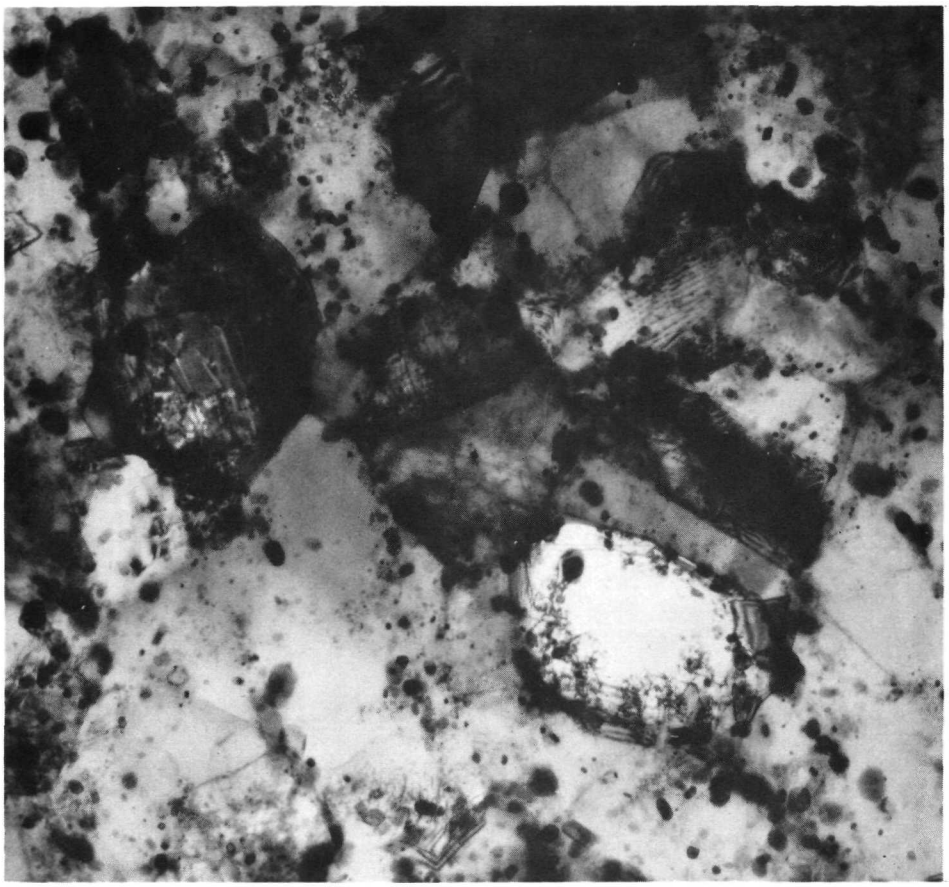

Figure 46 - Changes in the thoria particle distribution due to elevated temperature creep deformation. Note thoria particle collection at grain boundaries.

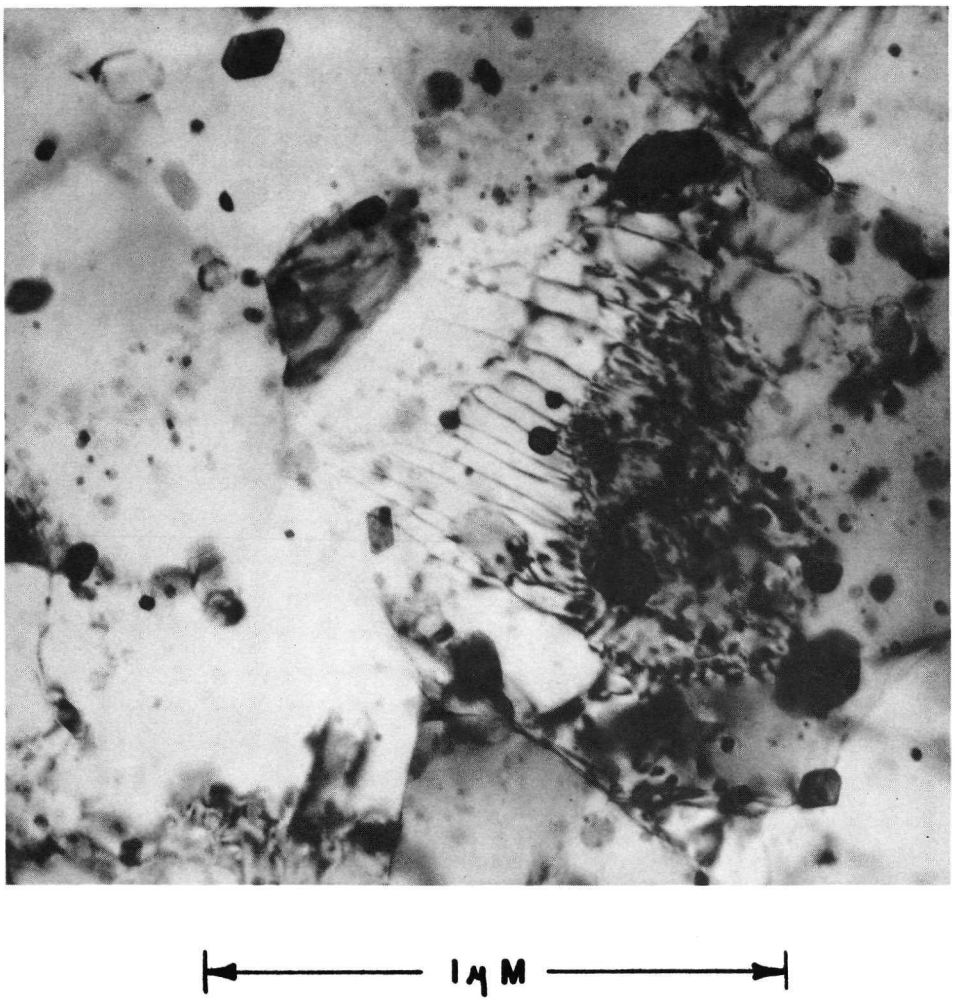

Figure 47 - Parallel dislocation array. Note dislocations "pinned" to thoria particles.

Figure 48 - Grain boundary dislocation source. Note source operation in center of micrograph.

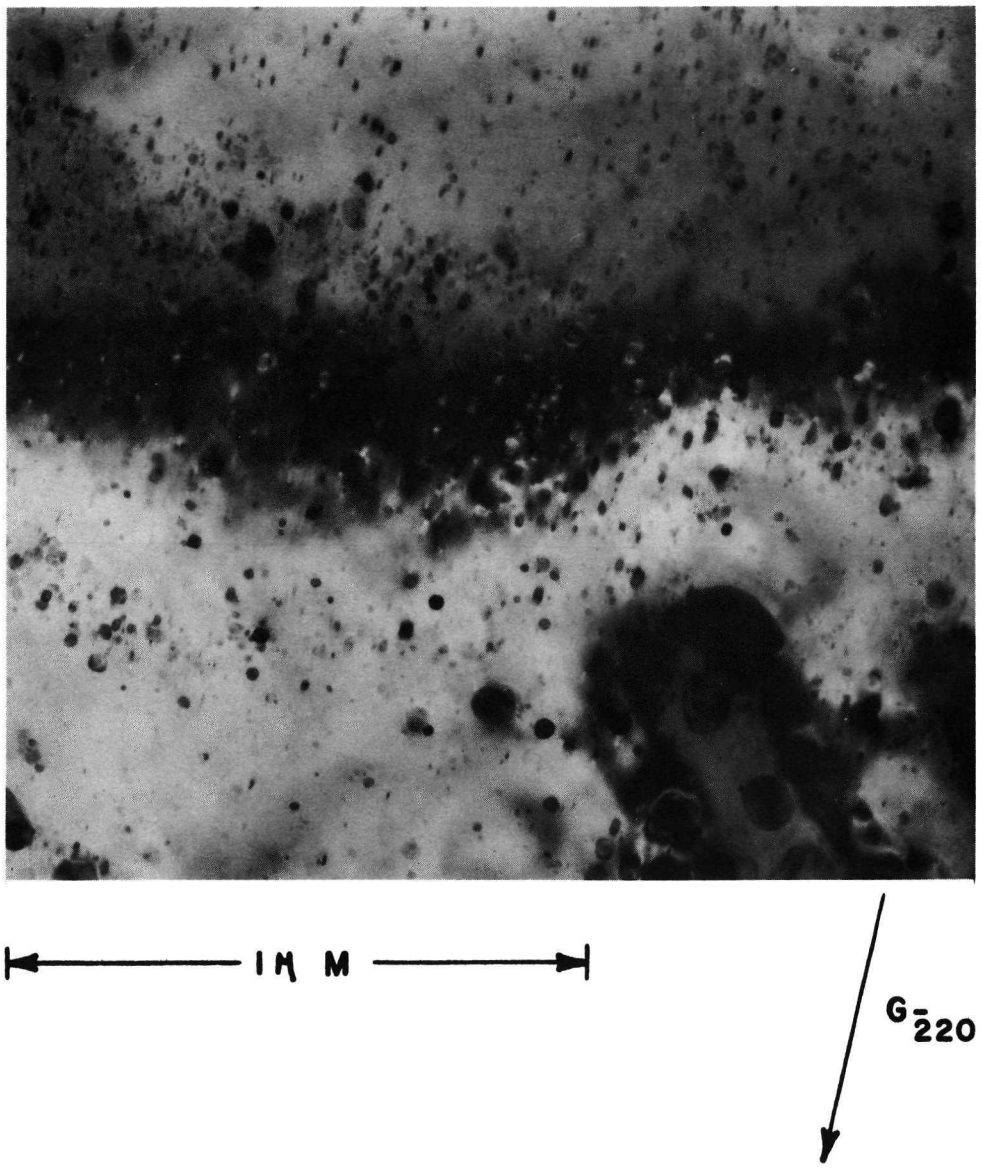

Figure 49 - Bright field micrograph of possible thoria particle surface tension matrix strains. The direction of the operative reciprocal lattice vector is shown.

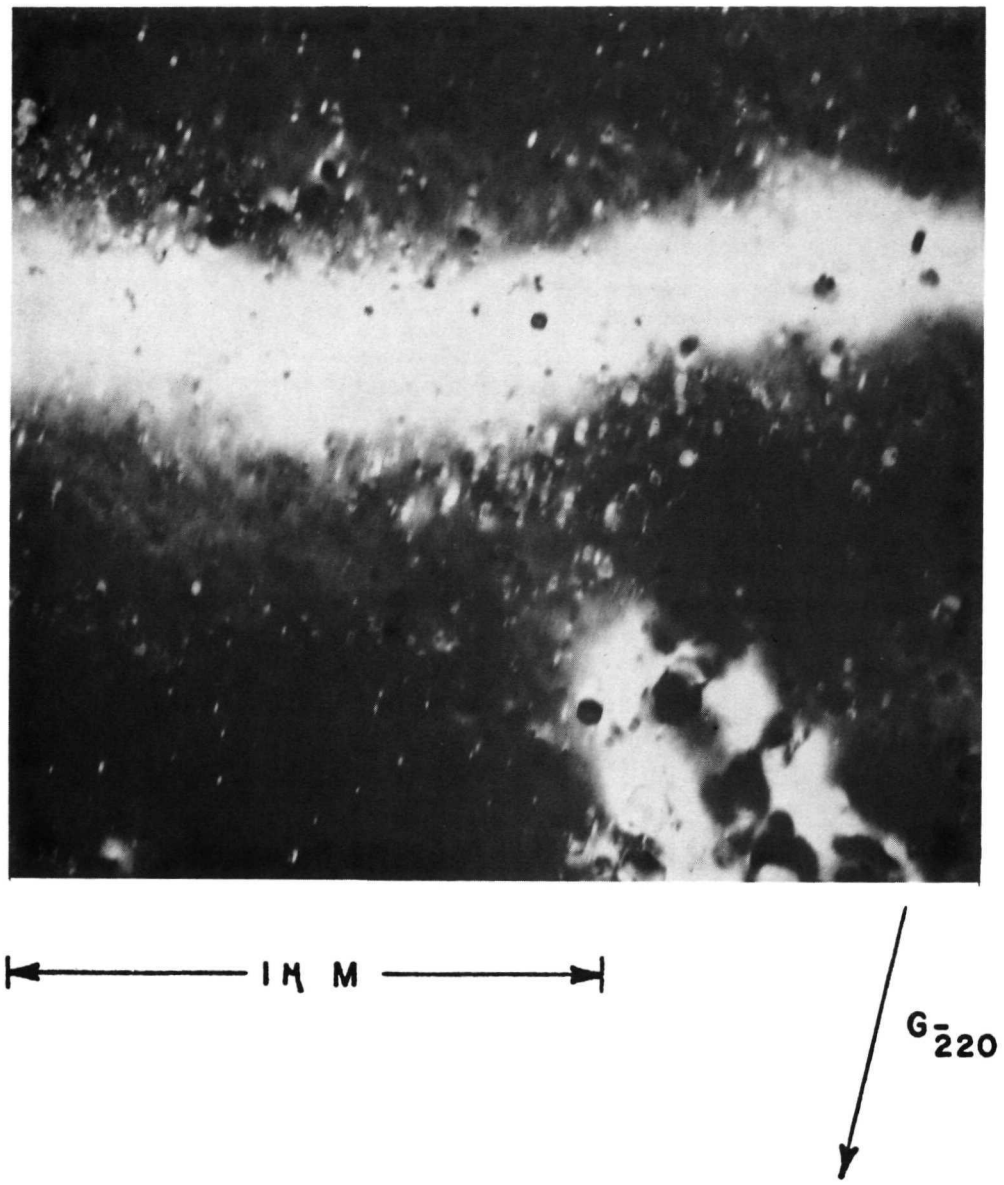

Figure 50 - Dark field micrograph of possible thoria particle surface tension matrix strains (same area as Figure 49). The direction of the operative reciprocal lattice vector is shown.

APPENDIX A

MATRIX SURFACE TENSION STRESSES AT SMALL, INCOHERENT, SECOND PHASE DISPERSED PARTICLES

Consider the small, second phase dispersed particle shown in Figure A1-a. The particle is assumed incoherent with the surrounding matrix (i.e. there is no continuity of lattice planes between particle and matrix). A surface tension σ exists at the particle-matrix interface. This surface tension is taken as equal to the surface energy E_s.

With respect to the matrix, presence of the particle serves to create an interface with a negative radius of curvature. In effect, the particle produces a "void" in the matrix material. For the small matrix surface element in Figure A1-b, mechanical equilibrium requires that surface tension forces be balanced by a pressure P. P may be calculated by slicing the "void" in half and equating forces, as in Figure A1-c. Thus, P is given by:

$$\pi R_o^2 P = 2\pi R_o \sigma \qquad \text{(A1)}$$

$$P = \frac{2\sigma}{R_o} = \frac{2E_s}{R_o} \quad , \text{ for } \sigma = E_s \qquad (A2)$$

Existence of the pressure P produces radial strains in the surrounding matrix (A1). Stresses can be described as those for a cavity with internal pressure in an infinite, isotropic solid (A2). Whether the internal pressure in the cavity is tensile (outward radial displacements) or compressive (inward displacements) depends on the sign of σ. σ will be assumed negative*. Stresses in the matrix are:

$$\sigma_{RR} = -\frac{2E_s}{R_o}\left(\frac{R_o}{R}\right)^3 \qquad (A3)$$

$$\sigma_{\theta\theta} = \sigma_{\phi\phi} = -\frac{1}{2}\sigma_{RR} = \frac{E_s}{R_o}\left(\frac{R_o}{R}\right)^3 \qquad (A4)$$

The stress field is triaxial and purely deviational in character (there is no dilatational component). This stress field is shown in Figure A2.

REFERENCES:

A1. F. V. Nolfi, Jr., and C. A. Johnson: Acta Met., 1972, vol. 20, p. 769.

A2. A. Eringen: Mechanics of Continua, p. 222, John Wiley & Sons, New York, 1967.

*A positive surface tension σ is probably more physically realistic. Use of a positive σ changes only the signs of σ_{RR}, $\sigma_{\theta\theta}$ and $\sigma_{\phi\phi}$.

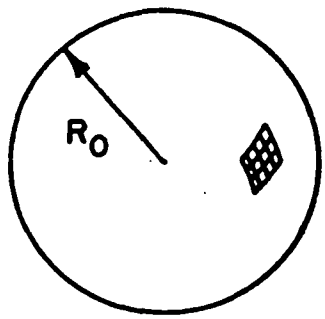

(a)

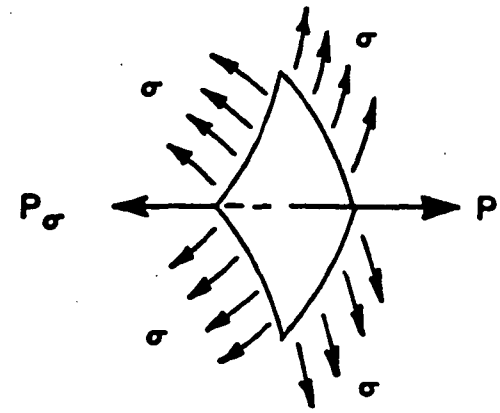

(b)

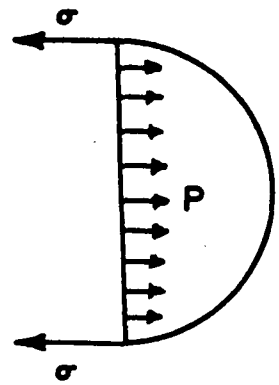

$$P = \frac{2E_S}{R_O}$$

(c)

Figure A1 - Surface tension stresses at the particle-matrix interface, for a positive surface tension σ. Stresses are reversed when σ is negative.

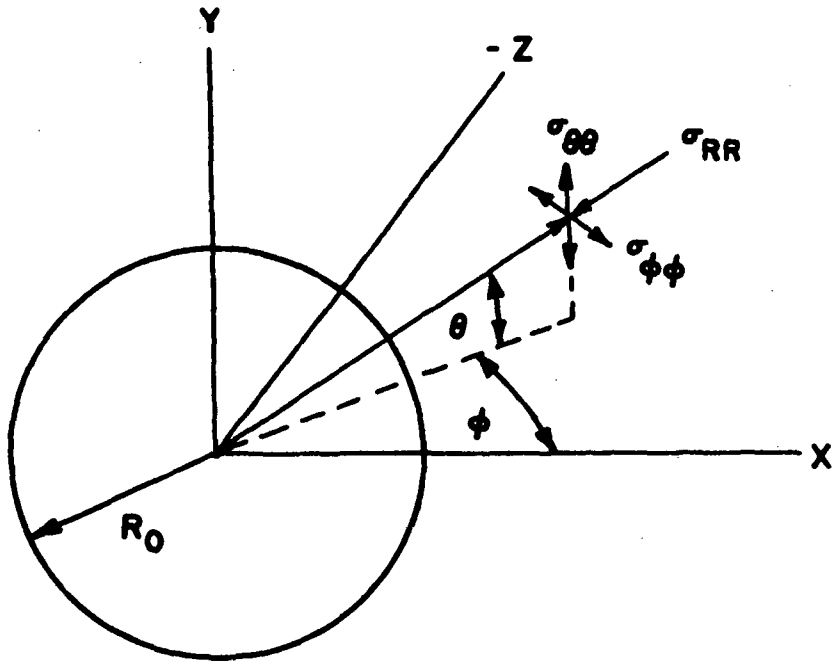

$$\sigma_{RR} = - \frac{2E_s}{R_0}\left(\frac{R_0}{R}\right)^3$$

$$\sigma_{\theta\theta} = \sigma_{\phi\phi} = - \frac{1}{2}\sigma_{RR} = \frac{E_s}{R_0}\left(\frac{R_0}{R}\right)^3$$

Figure A2 - Matrix stress field due to surface tension effects.

APPENDIX B

DISLOCATION-PARTICLE INTERACTIONS DUE TO MATRIX SURFACE TENSION STRESSES AT SMALL, INCOHERENT, SECOND PHASE DISPERSED PARTICLES

1. Interaction with Dislocation Glide

A. Surface Tension Shear Stress

A shear stress will result in the plane shown in Figure B1 as a consequence of the existence of the surface tension stress field in Appendix A. For a triaxial stress state (B1):

$$\tau^2 = (\sigma_1-\sigma_2)^2L^2M^2 + (\sigma_1-\sigma_3)^2L^2N^2 + (\sigma_2-\sigma_3)^2M^2N^2 \quad (B1)$$

where L, M and N are the direction cosines of the normal to the plane in question with the 1, 2 and 3 principal stress axes, respectively. Let:

$$\sigma_1 = \sigma_{RR},\ \sigma_2 = \sigma_{\theta\theta},\ \sigma_3 = \sigma_{\phi\phi}$$
$$L = \cos(90^o-\theta),\ M = \cos\theta,\ N = \cos 90^o = 0 \quad (B2)$$

as given in Figure B1 and Appendix A.

Therefore:

$$\tau_{xy} = \frac{(\sigma_{RR} - \sigma_{\theta\theta})}{2} \sin 2\theta \qquad \text{(B3)}$$

Converting to the cartesian coordinate system shown in Figure B1, τ_{xy} becomes:

$$\tau_{xy} = (-3E_s R_o^2)\{\frac{XY}{(X^2 + Y^2)^{5/2}}\} \qquad \text{(B4)}$$

This expression for τ_{xy} applies strictly only for the case where Z = O (the Z = O X-Y plane in Figure B1). For points where Z $\neq$ O, the shear stress defined by Equation B3 is different in direction than that shown in Figure B1. Thus, its component τ_{xy} will be different. For simplicity in the present analysis, only Equation B4 will be considered, since third dimension effects will not alter basic trends.

The shear stress τ_{xy} changes sign as X and Y change sign. A schematic description of the shear stress field is shown in Figure B2. Imai and Miyazaki (B2) have obtained a like τ_{xy} expression, for stress fields similar to those in Appendix A, but resulting from differential thermal expansion effects.

B. Edge Dislocation Interaction with the Surface Tension Shear Stress

Figure B3 shows an edge disloaction moving toward the particle. If the dislocation is of proper sign, work will be done by its motion in the field of τ_{xy} (i.e. it will be attracted toward the particle). The work done per unit dislocation length when the dislocation moves a distance dx in the direction of τ_{xy} is:

$$dW = \tau_{xy}\, b\, dx \qquad (B5)$$

The total work done may be found by integrating dW from $X = \infty$ to $X = X^*$ in Figure B3. However, the limit of infinity is unrealistic for the case of a dispersed second phase particle. The maximum outer integration limit should be one-half the interparticle spacing, since the shear stress fields of the particles overlap. In reality, the actual outer limit may be less than one-half the interparticle spacing due to the presence of internal stresses. If the outer integration limit is set at some distance d_o:

$$W = \int_{d_o}^{X^*} \tau_{xy}\, b\, dx \qquad (B6)$$

Therefore, using Equation B4:

$$W = E_s R_o^2 Yb\left\{\frac{1}{(X^{*2} + Y^2)^{3/2}} - \frac{1}{(d_o^2 + Y^2)^{3/2}}\right\} \qquad (B7)$$

The maximum interaction occurs when $X^* = 0$ (i.e. $Y = R_o$). For this case:

$$W = E_s R_o^3 b\left\{\frac{1}{R_o^3} - \frac{1}{(d_o^2 + R_o^2)^{3/2}}\right\} \qquad (B8)$$

The maximum interaction energy thus depends on both d_o and R_o. Considering d_o as fixed and varying R_o, the interaction energy is:

$$\begin{aligned} d_o &<< R_o: \quad W = 0 \\ d_o &\simeq R_o: \quad W = 0.646\ E_s b \\ d_o &>> R_o: \quad W = E_s b \end{aligned} \qquad (B9)$$

The interaction energy increases with decreasing R_o and has a maximum possible value of $E_s b$.

C. Estimate of the Magnitude of Surface Tension-Dislocation Glide Interactions

Consider an edge dislocation gliding on the plane $Y = R_o$ in Figure B3. It experiences a maximum attractive interaction (i.e. maximum binding energy)

when it reaches the point $(0,R_o)$. For the dislocation to move away from this point, work will have to be done by an imposed (i.e. external) shear stress.

A rough estimate of the shear stress required to move the dislocation away from the particle may be obtained in the following manner. Let the dislocation in Figure B3 be at position $(0,R_o)$ and apply an external shear stress τ, to move the dislocation away from the particle by a distance R_o. Then:

$$E_s b = \tau b R_o, \quad \tau = \frac{E_s}{R_o} \qquad \text{(B10)}$$

where $E_s b$ is the work required to move the dislocation per unit dislocation length, and $\tau b R_o$ is the work done by the dislocation in moving a distance R_o (per unit length). For this calculation, the maximum possible interaction energy with the particle has been employed.

Using values of $E_s = 0.62$ joule/M^2 (620 ergs/cm^2) (B3) and $R_o = 100 \times 10^{-10}$ M (B4), the calculated value of τ is 6.2×10^7 N M^{-2} (9000 psi).

By way of comparison, the stress required to operate a Frank-Read source is (B5):

$$\tau = \frac{\mu b}{d} \qquad \text{(B11)}$$

where μ = shear modulus, b = Burgers vector, and d = distance between pinning points. Using values of $\mu = 5.33 \times 10^{10}$ N M^{-2} (7.72×10^{6} psi)(B6) at 1255°K (1800°F), $b = 2.50 \times 10^{-10}$ M (B7), and $d = 1505 \times 10^{-10}$ M the interparticle spacing in TD-nickel (B4), the Frank-Read stress for bowing between particles at 1255°K (1800°F) is 8.85×10^{7} N M^{-2} (12,800 psi). This comparison indicates that the dislocation-particle glide interaction is not negligible.

2. Interaction with Dislocation Climb

A. Surface Tension Climb Stress

The climb stress for the edge dislocation pictured in Figure B4 is σ_{xx}. For simplicity σ_{xx} will be calculated here as a function of X and Y only, although it is also a function of Z. Again, third dimension effects are not critical to the basic arguments.

For a triaxial stress state (B1):

$$\sigma = \sigma_1 L^2 + \sigma_2 M^2 + \sigma_3 N^2 \qquad \text{(B12)}$$

where L, M and N are the direction cosines of the normal to the plane in question with the 1, 2 and 3 principal stress axes, respectively. Let:

$$\sigma_1 = \sigma_{RR}, \quad \sigma_2 = \sigma_{\theta\theta}, \quad \sigma_3 = \sigma_{\phi\phi} \qquad \text{(B13)}$$
$$L = \cos\theta, \quad M = \cos(90^o - \theta), \quad N = \cos 90^o = 0$$

as shown in Figure B4 and Appendix A. These values of L, M and N are for Z = O. The climb stress σ_{xx} is then:

$$\sigma_{xx} = \sigma_{RR}\cos^2\theta + \sigma_{\theta\theta}\cos^2(90^o - \theta) \qquad \text{(B14)}$$

Converting to the cartesian coordinate system shown in Figure B4, σ_{xx} becomes:

$$\sigma_{xx} = E_s R_o^2 \left\{ \frac{Y^2 - 2X^2}{(X^2 + Y^2)^{5/2}} \right\} \qquad \text{(B15)}$$

The field of σ_{xx} is shown in Figure B5. The climb stress is zero for $|Y| = \sqrt{2}\,|X|$.

B. Edge Dislocation Interaction with the Surface Tension Climb Stress

The climb force per unit dislocation length, F_{yy}, is related to σ_{xx} in the following way:

$$F_{yy} = - \sigma_{xx} b \qquad \text{(B16)}$$

Therefore:

$$F_{yy} = -E_s R_o^2 b \{ \frac{Y^2 - 2X^2}{(X^2 + Y^2)^{5/2}} \} \qquad \text{(B17)}$$

The field of F_{yy} is shown in Figure B6, for the dislocation sense indicated. F_{yy} is zero for $|Y| = \sqrt{2}\ |X|$.

The interaction energy due to the presence of the surface tension climb force may be calculated in the following manner. Place the dislocation in Figure B4 at the point $(0,R_o)$. In this position, the surface tension climb force is downward, and given by:

$$F_{yy}(0,Y) = -E_s R_o^2 b (\frac{1}{Y^3}) \qquad \text{(B18)}$$

But the dislocation cannot climb downward because the particle is in the way. Work will be required for the dislocation to climb upward against the surface tension

climb force. This work is given by:

$$dW = F_{yy}(0,Y)\ dy \qquad \text{(B19)}$$

As was done previously, Equation B19 is integrated to some outer limit d_o:

$$W = \int_{R_o}^{R_o+d_o} F_{yy}(0,Y)\ dy \qquad \text{(B20)}$$

Therefore:

$$W = \frac{E_s R_o^2 b}{2}\left\{\frac{1}{(R_o + d_o)^2} - \frac{1}{R_o^2}\right\} \qquad \text{(B21)}$$

The interaction energy W is dependent on d_o and R_o. Holding d_o fixed and varying R_o:

$$\begin{aligned} d_o &<< R_o: \quad W = 0 \\ d_o &\simeq R_o: \quad W = -(0.75)E_s b/2 \\ d_o &>> R_o: \quad W = -E_s b/2 \end{aligned} \qquad \text{(B22)}$$

The interaction energy increases with decreasing R_o and has a maximum value of $-E_s b/2$.

C. Estimate of the Magnitude of Surface Tension-Dislocation Climb Interactions

The driving force for dislocation climb in pure metals is thought to be the attraction between dislocations of opposite sign (B8). For edge dislocations, such attractions produce a climb force:

$$F_{yy} = \frac{\mu b^2}{2\pi(1-\nu)L_s} \qquad \text{(B23)}$$

where L_s is the separation distance between oppositely signed dislocations. Now consider a dislocation at position $(0,R_o)$ in Figure B4 and an oppositely signed one at a distance $R_o + L_s$ along the Y axis. The dislocation at $(0,R_o)$ will experience a positive climb force due to the other dislocation given by Equation B23. It will also be acted on by a negative climb force resulting from the surface tension given by:

$$F_{yy} = \frac{E_s b}{R_o} \qquad \text{(B24)}$$

The dislocation separation distance at which these two climb forces are equal is (equating Equations B23 and B24):

$$L_s = \frac{\mu b R_o}{2\pi(1-\nu)E_s} \qquad \text{(B25)}$$

Using values in Section 1-C and $\nu = 0.3$, the dislocation separation distance for equality of climb forces is 49×10^{-10} M. This separation is extremely small as compared to those usually encountered in the climb of pure metals.

3. Implications of Appendix B

The previous analysis has shown that the presence of matrix stresses due to surface tension effects postulated in Appendix A will influence both dislocation glide and climb, and that these influences will not be negligible. Results of Appendix B indicate that an edge dislocation will experience interactions tending to "pin" it to the particle, in both the glide and climb regimes. Appendix B suggests that small, incoherent, second phase dispersed particles will not be inert with respect to dislocation interactions, because of matrix surface tension stresses.

Unlike differential thermal expansion matrix stresses at second phase particles, surface tension matrix stresses cannot be relieved at elevated temperatures by vacancy diffusion. Thus, dislocation-particle interactions of the type described in Appendix B will occur at elevated temperatures.

REFERENCES:

B1. G. E. Dieter: Mechanical Metallurgy, p. 26, McGraw-Hill, New York, 1961.

B2. Y. Imai and T. Miyazaki: Trans. JIM, 1968, vol. 9 (supplement), p. 569.

B3. P. G. Shewmon: Recrystallization, Grain Growth and Textures, p. 173, ASM, Metals Park, Ohio, 1966.

B4. B. A. Wilcox, A. H. Clauer and W. B. Hutchinson: NASA Contract NAS 3-11167 Final Report, March, 1971.

B5. J. P. Hirth and J. Lothe: Theory of Dislocations, p. 683, McGraw-Hill, New York, 1968

B6. C. Susse: Journal de Physique, 1956, vol. 17, p. 910.

B7. B. D. Cullity: X-ray Diffraction, p. 483, Addison-Wesley, Reading, Mass., 1956.

B8. J. P. Hirth and J. Lothe: Theory of Dislocations, p. 513, McGraw-Hill, New York, 1968.

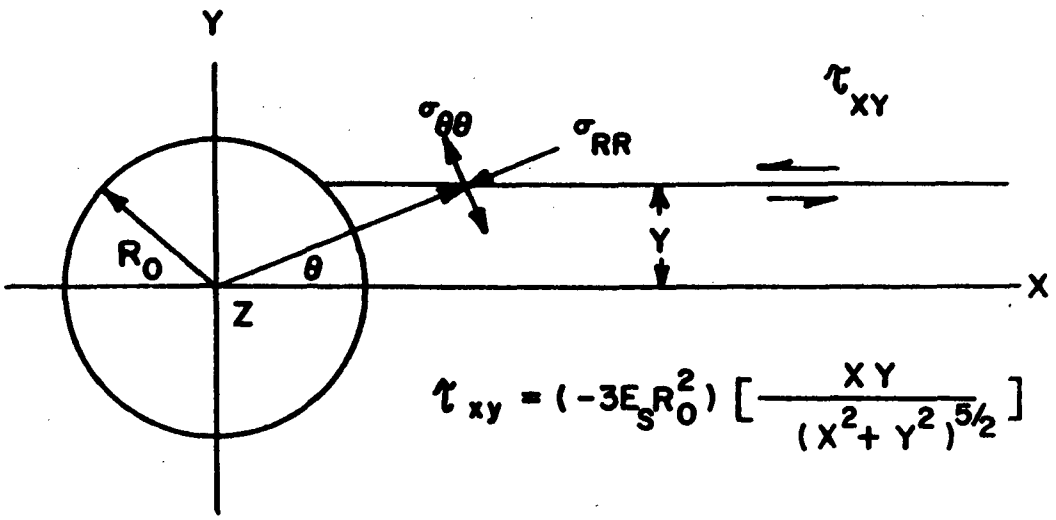

Figure B1 - Surface tension shear stress.

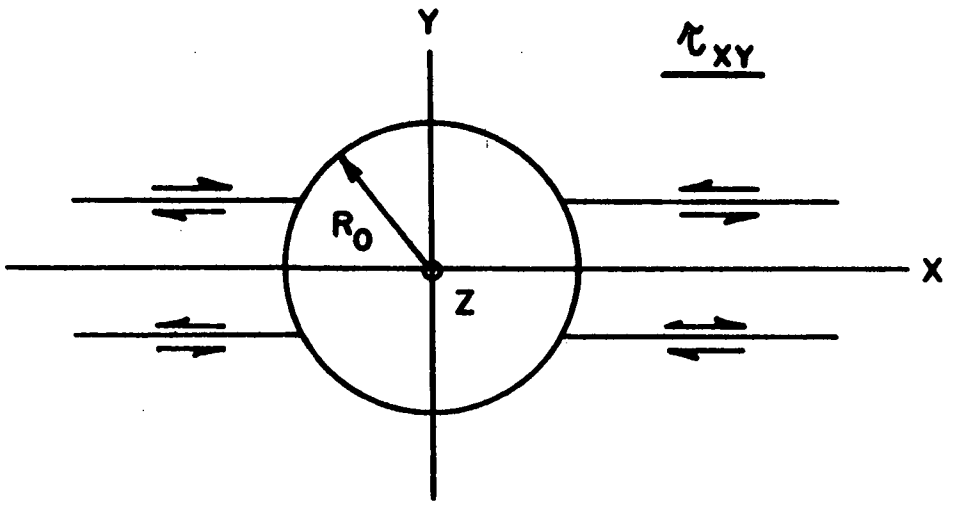

Figure B2 - Schematic description of the surface tension shear stress field.

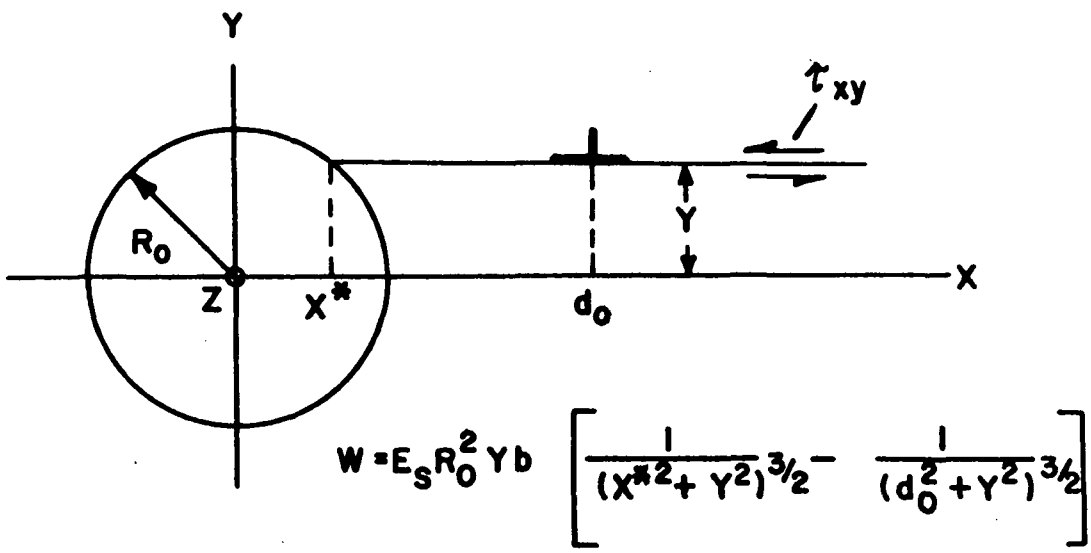

Figure B3 - Edge dislocation in the field of τ_{xy}.

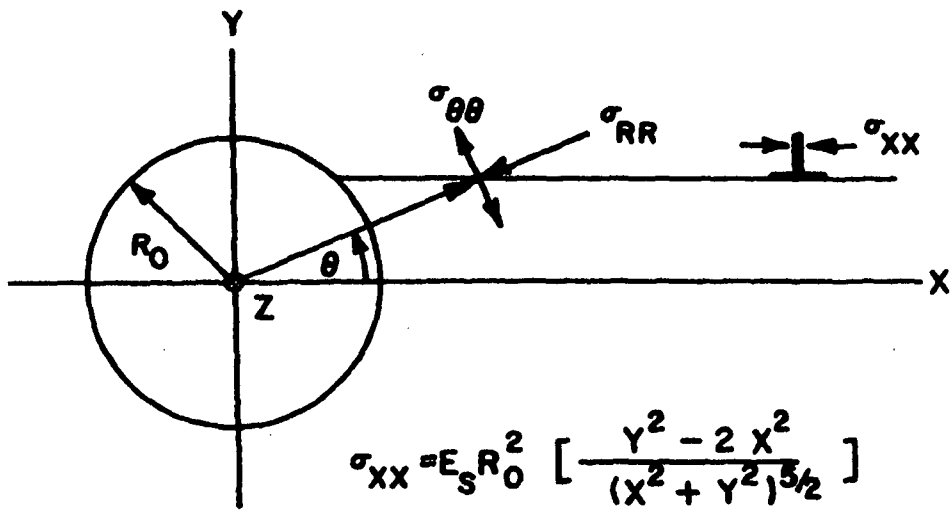

Figure B4 - Surface tension climb stress.

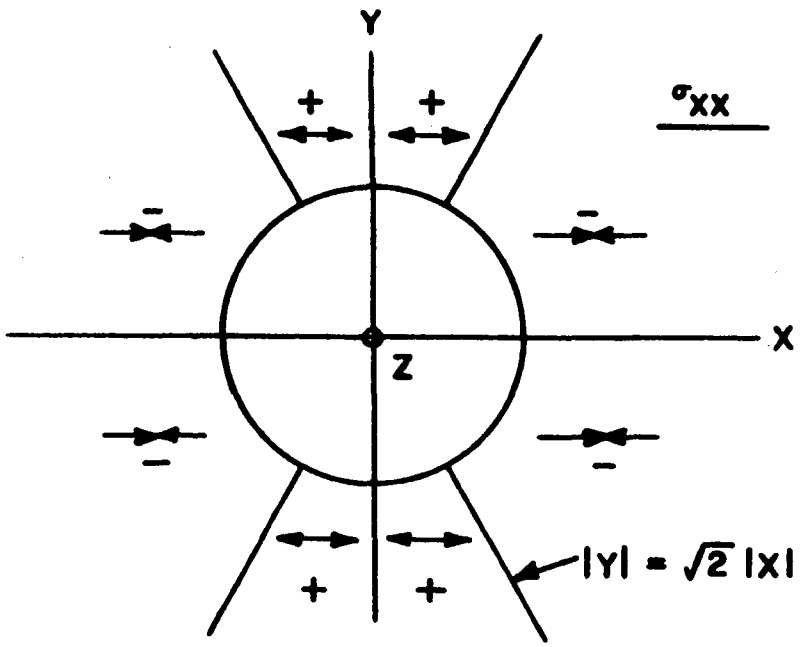

Figure B5 - Field of the surface tension climb stress (schematic).

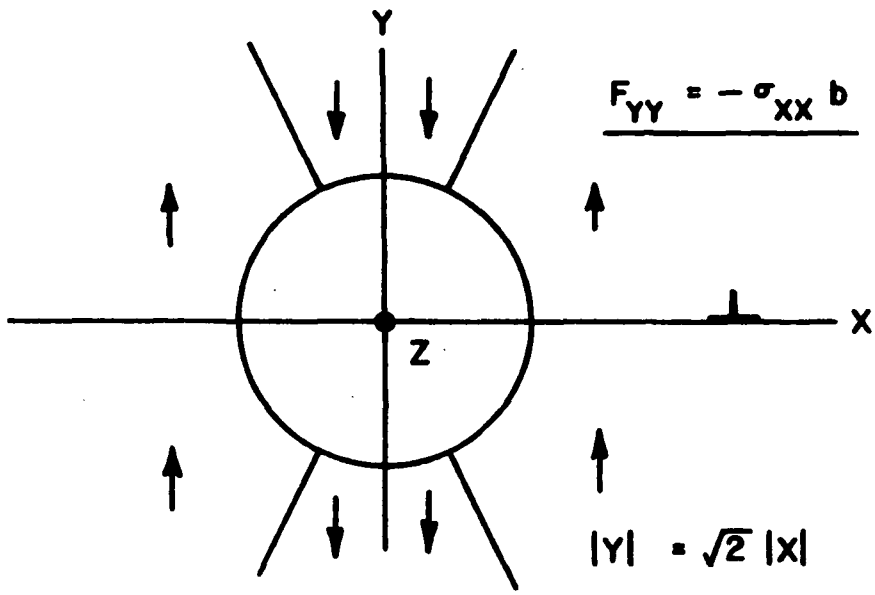

Figure B6 - Field of the surface tension climb force (schematic), for the dislocation sense shown.

APPENDIX C

THERMALLY ACTIVATED DISLOCATION MOTION IN THE PRESENCE OF DISLOCATION-PARTICLE INTERACTIONS DUE TO MATRIX SURFACE TENSION STRESSES AT SMALL, INCOHERENT, SECOND PHASE DISPERSED PARTICLES

1. Thermally Activated Edge Dislocation Glide

Consider the edge dislocation at the position shown in Figure C1. In this position it is at the point of maximum binding energy to the particle, with respect to surface tension stresses (Appendix B). The thermal activation enthalpy for dislocation glide motion is the work required to move the dislocation minus the work which the dislocation does on moving. The activation enthalpy U may be expressed as:

$$U = WL - \tau bA = U_o - \tau bA \qquad (C1)$$

where W = dislocation-particle interaction energy (Equation B8 in Appendix B), L = length of dislocation interacting with the particle, τ = applied shear stress, b = Burgers vector, and A = activation area.

The shear strain rate is given by:

$$\dot{\gamma} = \rho b V \qquad (C2)$$

where ρ = mobile dislocation density and V = average dislocation glide velocity. The dislocation velocity V is of the form:

$$V = \nu_o B C e^{-U/kT} \qquad (C3)$$

where ν_o = frequency of vibration of the dislocation involved in the thermal activation event, B = area swept out per successful thermal fluctuation, C = number of places where thermal activation can occur per unit dislocation length, k = Boltzman constant, and T = absolute temperature.

Therefore, the shear strain rate becomes:

$$\dot{\gamma} = \rho b \nu_o B C e^{-U/kT} \qquad (C4)$$

The area swept out per successful thermal fluctuation B is estimated from Figure C2 as $B \simeq \pi d^2/2$, where d is the interparticle spacing of the dispersed second phase. Also from Figure C2, the number of thermal activation

locations per unit dislocation length is taken as $C \simeq 1/d$. For a dispersed phase of spherical particles (C1):

$$d = \left(\frac{2\pi}{3}\right)^{1/2} \frac{R_o}{f^{1/2}} \qquad (C5)$$

where R_o = particle radius and f = volume fraction of dispersed particles.

With the above values, the final expression for the shear strain rate is:

$$\dot{\gamma} = \left(\frac{\pi}{6}^3\right)^{1/2} \frac{\rho b R_o \nu_o}{f^{1/2}} e^{-U/kT} \qquad (C6)$$

An estimate of the value of U_o in Equation C1 can be obtained from Appendix B. Let $W = 0.646\ E_s b$ and $L = 2R_o$. Then, using the values shown in Section 1-C of Appendix B, the calculated value for U_o is 12.5 ev.

The activation enthalpy U in Equation C1 is stress dependent, and decreases with increasing stress. It is of interest to calculate the stress required to lower U to some level, say 3 ev.

Then, from Equation C1:

$$3 \text{ ev} = 12.5 \text{ ev} - \tau bA$$

$$\tau = \frac{9.5 \text{ ev}}{bA} \qquad \text{(C7)}$$

In order to calculate τ , the activation area A must be estimated. The activation area is given by:

$$A = L\ X \qquad \text{(C8)}$$

where L = dislocation length involved in the activation event and X = distance moved by the dislocation length during the activation event. Let $L = 2R_o$ and $X = R_o$. Then from Appendix B, Section 1-C, the value of A is $2 \times 10^{-12} cm^2$. Using this value in Equation C7, the stress required to lower the activation enthalpy to 3 ev is 3.04×10^7 N M^{-2} (4410 psi).

It seems likely that because U_o has a high value, a portion of the applied stress will be required to lower the total activation enthalpy U to values such that measurable strain can be observed in finite times (the previous calculation). This suggests that the total applied stress τ in Equation C1 will be the sum of two factors:

$$\tau = \tau^* + \tau_i \qquad \text{(C9)}$$

where τ = applied stress, τ_i = stress required to lower the activation enthalpy U (i.e. in effect, an internal stress), and τ^* = effective stress in the thermal activation event.

2. Thermally Activated Edge Dislocation Climb

For edge dislocations the climb velocity V_o is given by (C2):

$$V_o = \frac{D_v \Omega F_c}{b^2 kT} \qquad (C10)$$

where D_v = volume diffusion coefficient, Ω = atomic volume, b = Burgers vector, k = Boltzman constant, T = absolute temperature, and F_c = climb force. For the attraction of dislocations of opposite sign, the climb force is given in Appendix B, Equation B23. Using this expression, the climb velocity becomes:

$$V_o = \frac{D_v \Omega \mu}{2\pi(1-\nu)kTd_c} \qquad (C11)$$

where d_c is the dislocation separation distance.

Equation C11 has been used to describe creep in a pure metal where dislocation climb is rate controlling (C3). The creep-dislocation climb situation in a dispersion hardened material is shown in Figure C3.

Dislocation sources with some separation d_c generate dislocations which glide for a distance L past dispersed particles, then climb and annihilate. This situation is analogous to that described by Weertman (C3), where creep strain is produced by glide, but climb is the rate controlling process for creep.

For the system in Figure C3, it seems possible that surface tension effects at the particles can influence climb in two ways. First, the presence of restraining climb forces discussed in Appendix B will reduce the total climb force F_c in Equation C10. Second, the surface tension stresses may cause the climb process to require double-jog nucleation (C4). These two effects give:

$$F_c' = M F_c \qquad M<1 \qquad \text{(C12)}$$

where F_c is given in Equation C11, and:

$$V = V_o e^{-2F_j/kT} \qquad \text{(C13)}$$

where F_j is the jog formation energy.

Thus, the climb velocity with these modifications becomes:

$$V = \frac{MD_v\Omega\mu}{2\pi(1-\nu)kTd_c} e^{-2F_j/kT} \qquad \text{(C14)}$$

The shear strain rate is given by Equation C2. Equation C2 contains the dislocation glide velocity. The dislocation glide velocity is related to the climb velocity by:

$$v_{glide} \simeq \frac{L}{d_c} v_{climb} \qquad L > d_c \qquad (C15)$$

where L and d_c are shown in Figure C3. If N is the dislocation source density, then $L = 1/(N\pi d_c)^{\frac{1}{2}}$. Therefore, from Equation C2:

$$\dot{\gamma} = \frac{\rho b M D_o \Omega \mu}{2N^{1/2}\pi^{3/2}(1-\nu)kTd_c^{5/2}} e^{-(\Delta H_{SD}+2F_j)/kT} \qquad (C16)$$

where D_o = diffusion coefficient pre-exponential and ΔH_{SD} = self diffusion enthalpy.

If Equations C12 and C13 are valid, Equation C16 indicates that the climb activation enthalpy will be increased by $2F_j$ and that the pre-exponential term will be reduced by the factor M, compared to the case for creep climb processes in pure metals (C3). Thus, creep controlled by climb will be slower in dispersion hardened materials than in pure metals. Equation C16 indicates that the activation enthalpy will not be stress dependent. For dispersion hardened materials,

the quantity d_c is not necessarily related to the interparticle spacing, but rather to the spacing between dislocation sources, as shown in Figure C3. From Appendix B, the value of M might be expected to decrease with decreasing particle radius R_o. The jog formation energy F_j may be calculated (C5) and has a value of 0.59 ev for nickel.

REFERENCES:

C1. B. A. Wilcox and A. H. Clauer: Trans. AIME, 1966, vol. 236, p. 570.

C2. J. P. Hirth and J. Lothe: Theory of Dislocations, p. 513, McGraw-Hill, New York, 1968.

C3. J. Weertman: Trans. ASM, 1968, vol. 61, p. 681.

C4. J. P. Hirth and J. Lothe: Theory of Dislocations, p. 527, McGraw-Hill, New York, 1968.

C5. J. P. Hirth and J. Lothe: Theory of Dislocations, p. 247, McGraw-Hill, New York, 1968.

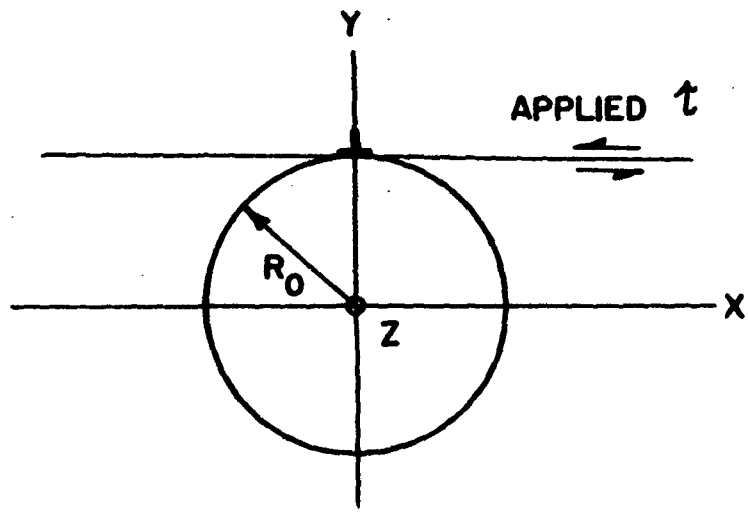

Figure C1 - Edge dislocation at a particle. The dislocation is at the position $(0,R_o)$.

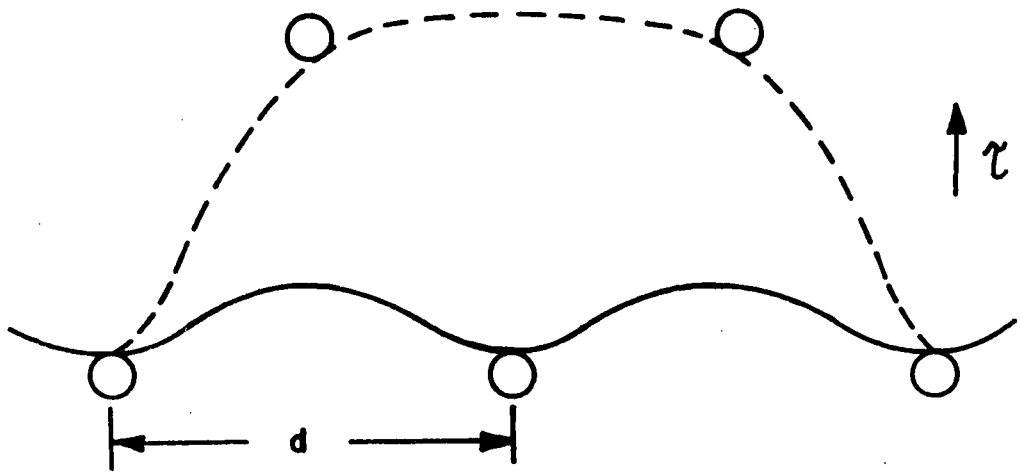

Figure C2 - Glide motion of the dislocation after a successful thermal activation event in a dispersion hardened material. Circles denote dispersed particles.

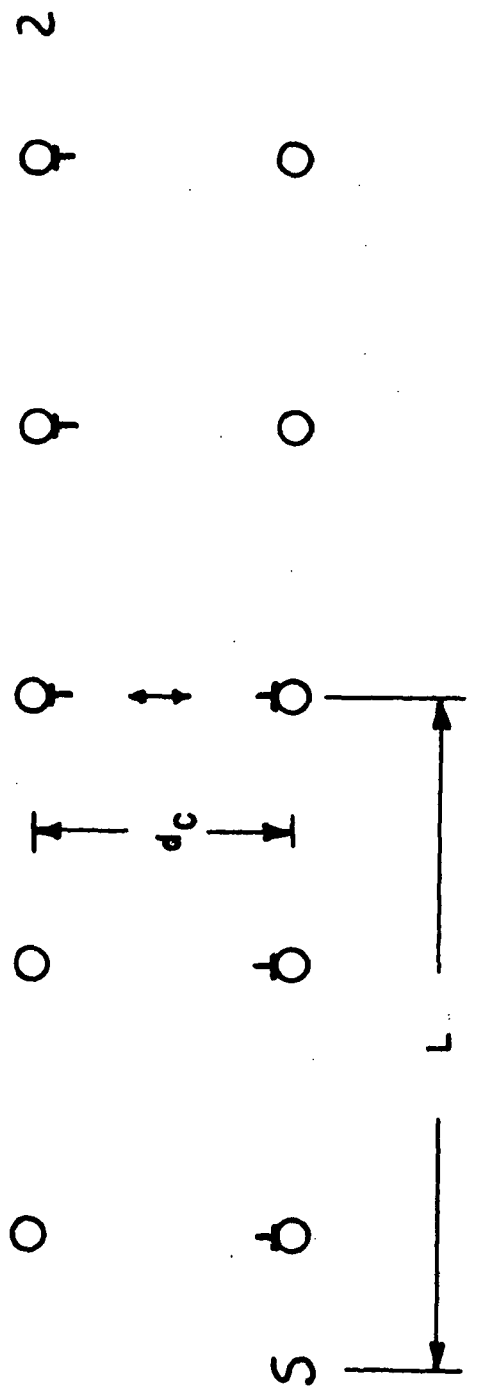

Figure C3 - Dislocation climb creep in a dispersion hardened material.

APPENDIX D

FRACTURE IN A DISPERSION HARDENED MATERIAL WHEN DEFORMATION IS BY DIFFUSION CONTROLLED GRAIN BOUNDARY SLIDING

The diffusion controlled grain boundary sliding process in a pure metal is shown schematically in Figure D1. Sliding is controlled by the diffusion of atoms from boundary locations of compressive normal stress to those of tensile normal stress (D1). For this process to occur in a dispersion hardened material, dispersed particles must collect at grain boundaries, Figure D2, since the second phase particles will act as inert markers with respect to lattice diffusion (D2,D3,D4).

It is proposed that collection sites for particles at grain boundaries may also be sites for potential cracks, as shown in Figure D3. If this is the case, then the fracture strain and fracture time may be calculated in the following manner.

The grain boundary area is assumed to become a propagating crack when the volume of dispersed particles collected there reaches a critical value V_f.

V_f is calculated for the idealized system shown in Figure D4. Consider the sliding path in Figure D4. Sliding is occurring at a rate $\dot{U}$ under the action of an applied shear stress. The volume of atoms removed from the shaded region in time dt is:

$$dV_{atoms} = (\dot{U}\ dt)(h)(Z) \qquad (D1)$$

where Z is the boundary dimension into the paper. If f is the volume fraction of second phase particles, then:

$$dV_{particles} = f\ dV_{atoms} \qquad (D2)$$

where $dV_{particles}$ is the volume of particles collected at the region shown in the time dt.

Assuming that fracture occurs when $V_{particles} = V_f$:

$$\int_{V_o}^{V_f} dV_{particles} = \int_0^{t_f} \dot{U}hZf\ dt \qquad (D3)$$

where V_o is the initial volume of particles at the boundary before sliding deformation. The fracture time is then:

$$t_f = \frac{V_f - V_o}{\dot{U}hZf} \qquad (D4)$$

The fracture displacement (Figure D4) is given by:

$$X_f = \frac{V_f - V_o}{hZf} \qquad (D5)$$

In a polycrystalline material, the shear strain rate is:

$$\dot{\gamma} = \frac{A\dot{U}}{d}, \qquad \dot{U} = \frac{dX}{dt} \qquad (D6)$$

where A = a constant and d is the grain diameter ($\dot{\gamma} = \sqrt{2}\ \dot{\epsilon}$, where $\dot{\epsilon}$ is the uniaxial strain rate). The quantity hZ is taken as a fraction of the total boundary surface area per grain:

$$hZ = Bd^2 \qquad (D7)$$

The parameter B will increase with increasing amplitude of the boundary in Figure D4. This means that B will increase with increasing L/D ratio, the grain elongation index. Using the above approximations, the final expressions are:

$$t_f = \frac{A(V_f - V_o)}{B\dot{\gamma}d^3f} \qquad (D8)$$

for the rupture time, and:

$$\gamma_f = \frac{A(V_f - V_o)}{Bd^3 f} \qquad (D9)$$

for the fracture shear strain. Equation D9 indicates that the fracture strain will decrease with increasing grain diameter and increasing L/D ratio.

REFERENCES:

D1. R. Raj and M. F. Ashby: Met. Trans., 1971, vol. 2, p. 1113.

D2. B. Burton: Metal Sci. J., 1971, vol. 5, p. 11.

D3. F. V. Lenel, G. S. Ansell and D. D. Barron: Met. Trans., 1970, vol. 1, p. 1772.

D4. F. V. Lenel, G. S. Ansell and R. C. Morris: Met. Trans., 1970, vol. 1, p. 2351.

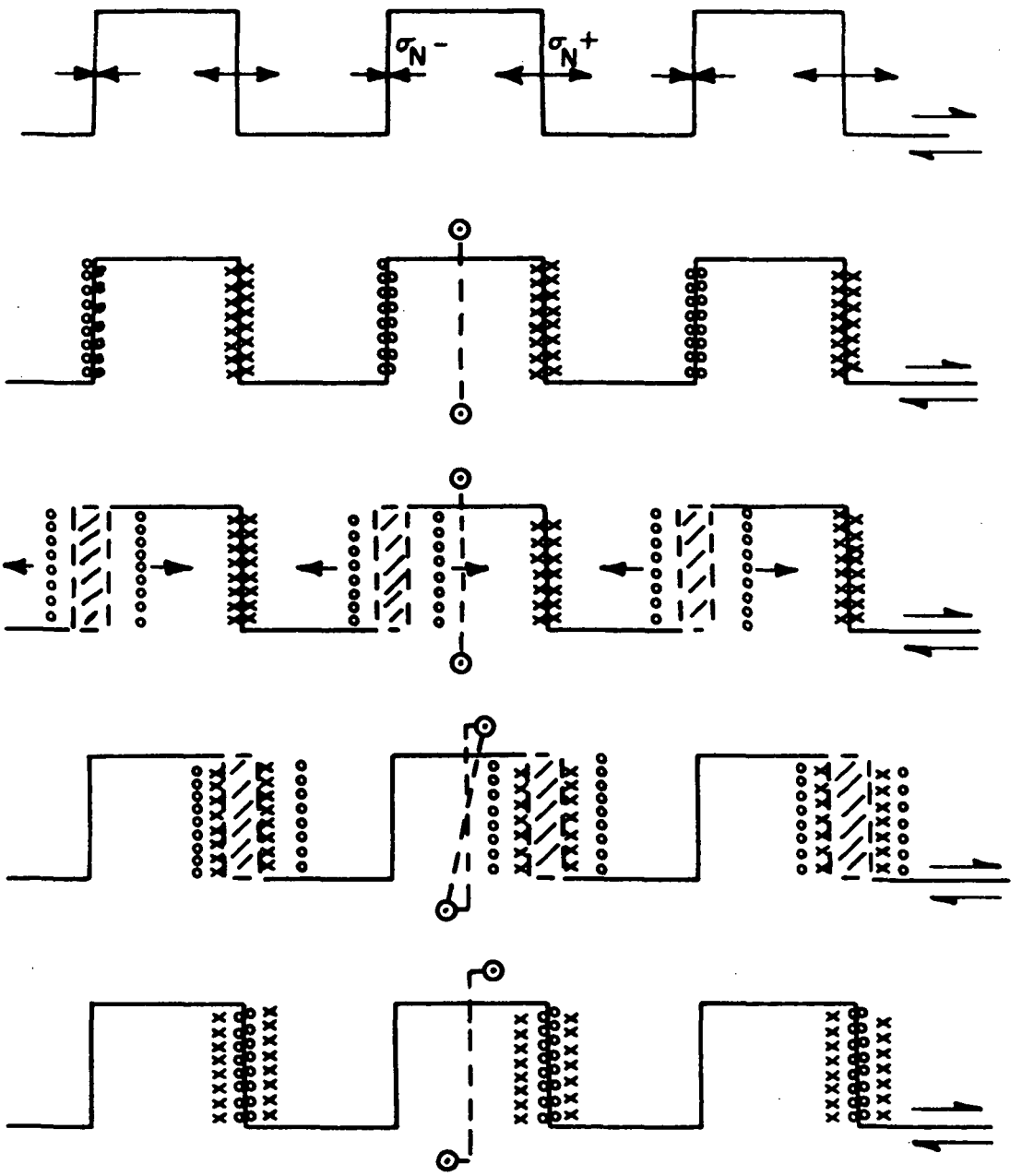

Figure D1 -- Schematic representation of diffusion controlled grain boundary sliding in a polycrystal of square grains. The sliding path is along grain boundaries. The symbols o and x represent atoms at grain boundaries.

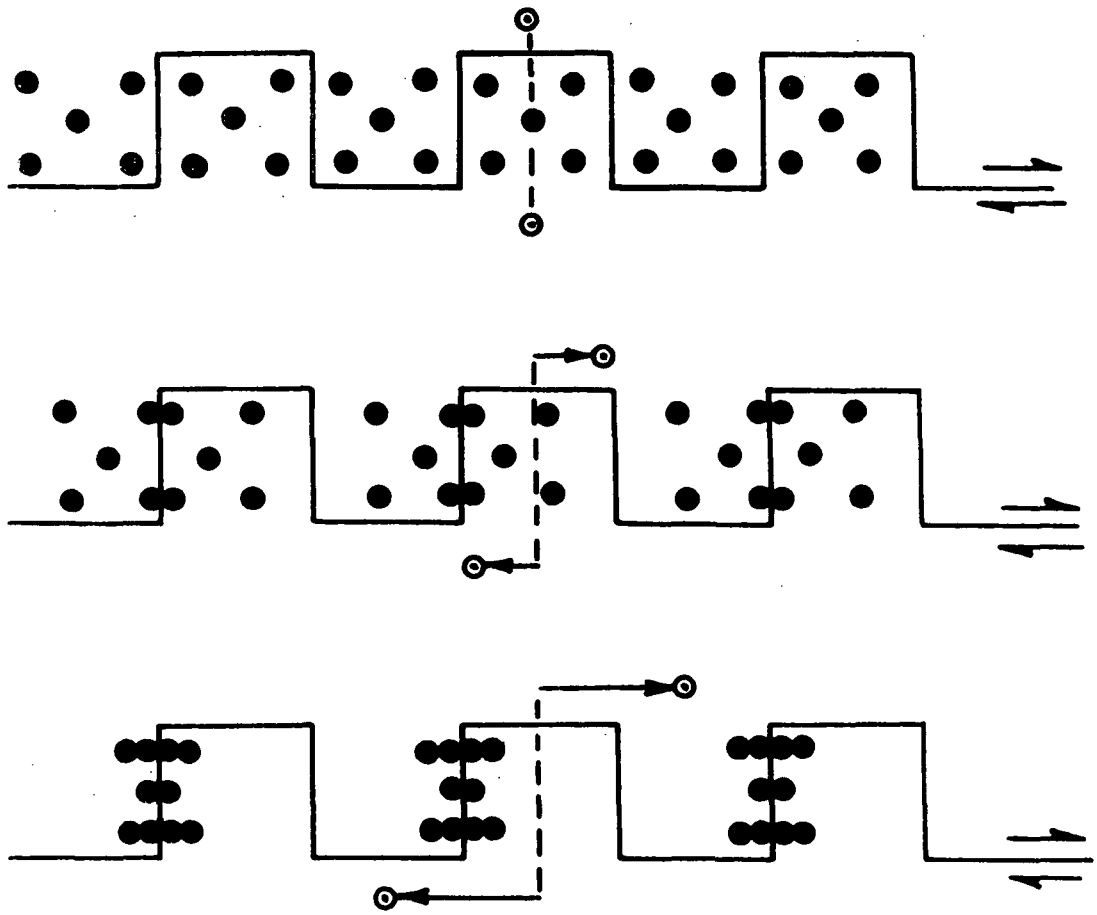

Figure D2 - Collection of dispersed particles at grain boundaries as a result of diffusion controlled grain boundary sliding. Black dots represent dispersed particles.

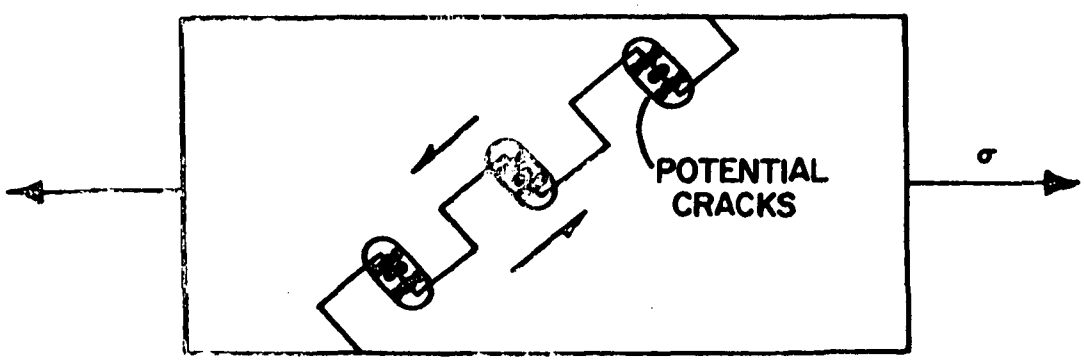

Figure D3 - Potential cracks at sites where dispersed particles have collected.

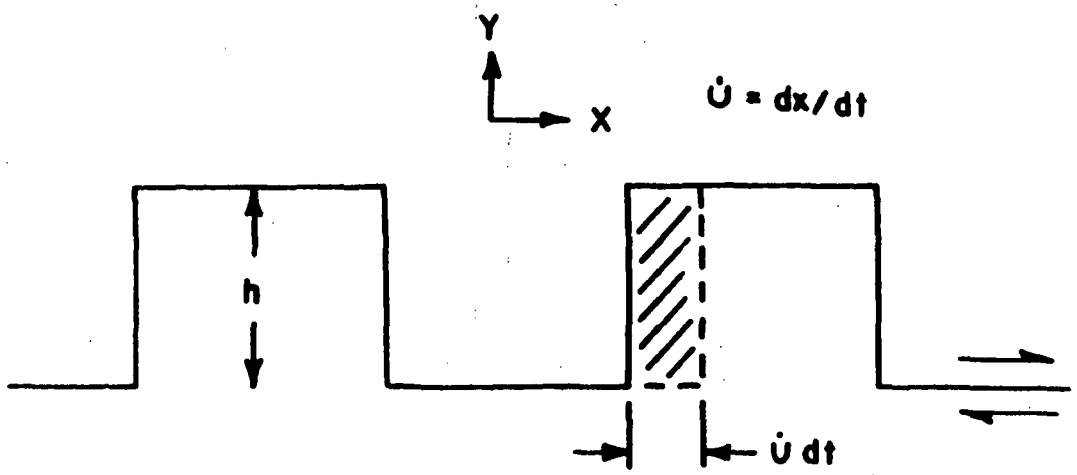

Figure D4 - Idealized grain boundary sliding system.

SECTION II

DEFORMATION AND ANNEALING RESPONSE OF TD-NICKEL-CHROMIUM

by

RUSSELL D. KANE

INTRODUCTION

The past years research included not only the completion of the mechanical testing on TD-nickel, but also the initiation of the work on thoria dispersed nickel-chromium)TD-NiCr). The major direction of the research conducted on TD-NiCr sheet material thus far have been as follows:

1. A full and complete characterization of the deformation and annealing response of TD-NiCr, starting state 0.1 inch thick sheet.
2. An evaluation of the role of grain size of TD-NiCr in determining the high temperature tensile properties of the TD-NiCr sheet material.

Previous work conducted in this program has shown that the grain size and shape in TD-nickel can be controlled by various deformation and annealing treatments*. Since the elevated temperature mechanical properties of TD-nickel have been observed to be very much dependent on grain size and shape**, the characterization of the deformation and annealing response and eventual

---

* A detailed discussion of this work can be found in the Annual Status Report for the period of January 1969 to January 1970.

** A detailed discussion of this work can be found in the first section of this Status Report, pages 1-172.

control of these parameters is of the greatest importance.

Even though it is apparent that TD-nickel is not a classical prototype of all TD-nickel base alloys, the previous work in this program has served as a basis for the research being conducted on the TD-NiCr sheet material. In turn, it is hoped that the present research will aid future investigations in TD-nickel base alloys.

The research on TD-NiCr to date is perhaps more importantly the first step in the evaluation of the high temperature flow characteristics of this material. With the completion of this segment, high temperature tensile, creep and creep rupture data will data will be collected as a function of material and testing related parameters, in order to evaluate the mechanisms of elevated temperature deformation found in TD-NiCr sheet material.

MATERIALS AND PROCEDURE

Material:

For the present investigation, TD-Nickel-Chromium (TD-NiCr) was supplied by the Fansteel Company in the form of 0.1 inch thick sheet. The material was a nickel-20 weight percent chromium, single phase matrix containing 2 volume percent thoria as a dispersion of fine particles; it was produced by the standard powder metallurgical techniques. The material used in the study was received in the fully dense, unannealed condition in the form of a 12 inch x 12 inch x 0.1 inch sheet.

Deformation and Annealing:

The deformation and annealing response of TD-NiCr 0.1 inch sheet was determined by longitudinal and transverse rolling of the material without varying the rolling plane from that of the as-received material. These rolling operations were then followed by annealing treatments. The rolling was performed in step reductions of approximately 10 percent per pass. All annealing was done in an argon atmosphere for 1 hour at 2400°F unless specified otherwise. The material was allowed to heat and cool at furnace heating and cooling rates.

The as-received, unannealed TD-NiCr, as well as the annealed material, was rolled to various reductions, annealed at 2400°F and observed in the etched condition with light-optical microscopy. Unannealed, as-received TD-NiCr was reduced 10%, 28%, and 44% by separate longitudinal and transverse rolling operations. As-received and annealed material was rolled 12%, 21%, 28%, 48% and 67% in the transverse direction and 53% longitudinally. Some of the TD-NiCr that was transversely rolled 48% was annealed and rerolled 35%.

To study the dependence of grain size on annealing temperature the as-received TD-NiCr was annealed at temperatures between 1550°F and 2400°F in argon for 2 hours. Specimens were observed with light-optical microscope in the etched condition.

Grain Size Determinations:

The grain size in the annealed materials was determined as a function of the degree and mode of deformation and of the annealing temperature. The grain sizes were determined by quantitative metallography employing line intercept measurements in three mutually perpendicular directions. The three directions were the rolling direction, rolling plane transverse direction and the thickness plane transverse direction. This procedure was necessary so that grain size, grain shape and grain

volume could be characterized accuarately. Each grain size measurement was the result of more than 25 separate observations.

The TD-NiCr specimens that were rolled to various reductions and then annealed were metallographically polished and etched in order to reveal their grain structures. The etch for TD-NiCr was an electro-etch consisting of 6 parts ethanol, 1 part H_2SO_4 and 21 parts water. The etchant delineated the grain boundaries when the etching voltage was 5 volts.

Elevated Temperature Tensile Testing:

Tensile tests were conducted on TD-NiCr sheet material over a temperature range of 1100°F to 2000°F. Four grain sizes of TD-NiCr sheet were chosen for study; the average grain dimensions ranged from 0.0037mm to 0.0515mm. These material states were produced by transverse rolling of the as-received and annealed TD-NiCr 0.1 inch sheet. All tensile specimens were in the annealed condition when tested. The tensile specimen design is shown in Figure 51.

The elevated temperature tensile tests were carried out in a vacuum of approximately 10^{-4} torr. The temperature was monitored by a thermocouple at the center of the gage section. For all specimens tested, the strain

rate was 0.01 inches per inch per minute (cross-head speed, 0.005 inches per minute).

RESULTS

Deformation and Annealing:

Upon rolling and subsequent annealing of the as-received, unannealed TD-NiCr sheet, the average grain dimension was found to decrease with increasing severity of deformation for both longitudinal and transverse rolling, as shown in Figure 52. True rolling strain has been used to indicate deformation to permit a more accurate representation of the data. Transverse rolling is observed to have a somewhat greater effect on reducing the grain size when followed by an annealing treatment than does longitudinal rolling under the same conditions.

The grain shape was that of a oblate spheroid with a tendency for the thickness dimension of the grains to be less than the other two dimensions. The transversely rolled, as-received TD-NiCr and L/D ratios between 2.2 and 1.6, showing decreasing L/D for increased rolling severity. The longitudinally rolled material had L/D values varying between 1.8 and 2.9. The ratio initially increased from 2.2 for the as-received and annealed material to 2.9 for a 28% longitudinal reduction. Further longitudinal rolling proved only to decrease the L/D ratio.

Figure 53 shows the dependence of the average grain dimension on deformation severity for longitudinal and transverse rolling of the as-received and annealed TD-NiCr sheet. The average grain dimensions decreased with increasing deformation severity. However, transverse rolling produces a somewhat smaller annealed grain size than does longitudinal rolling.

For both transverse rolling of the as-received TD-NiCr and the as-received and annealed TD-NiCr, the smallest grain size observed was 0.0036mm. This value occurred at a 44% reduction for the as-received material and at 67% for the as-received and annealed material. In both cases the limiting factor was the cracking of the material upon further reduction.

Grain shape for the as-received and annealed TD-NiCr which had been transversely rolled and reannealed was observed to be a oblate spheroid with a tendency for the thickness dimension to be less than the other two and a slight elongation in the rolling direction. The L/D ratios varied between 1.3 and 3.4. The maximum L/D occurred at approximately 12% reduction. Longitudinal rolling produced a slightly more elongated annealed grain, L/D equal to 3.5, after 53% reduction.

The TD-NiCr that was reduced 48% transversely, annealed and rerolled 35% again transversely showed

evidence of increased grain size upon annealing. After 48% reduction, the average grain dimension was 0.0037mm. With continued rolling reductions of 35% the annealed grain size increased to 0.0067mm.

Figure 54 shows the effect of the annealing temperature on the average grain dimension determined in the as-received and annealed material. The grain size is observed to increase with decreasing annealing temperature over the temperature range 1750°F to 2400°F. At 1550°F the material showed no evidence of recrystallization after a two hour anneal.

Elevated Temperature Tensile Testing:

From the tensile tests performed on various grain sizes of TD-NiCr sheet material over the temperature range 1100°F to 2000°F, the following data was recorded: 1) tensile strength, 2) 0.2% offset yield strength and 3) ductility in terms of percent elongation. Figures 55 and 56 show the tensile and yield stress, respectively, as a function of testing temperature for the four material states tested. All stress levels were observed to decrease with increasing temperature and decreasing average grain dimensions.

The dependence of the ductility on the testing temperature is shown in Figure 57. At 1100°F, all elongations are clustered around 4 percent. As the testing

temperature is increased, the ductility varies with the grain size. Between 1800°F and 2000°F, the ductility increases with decreasing grain size.

Figures 58 and 59 show the tensile and yield strength as a function of the average grain dimension. Over the range of grain sizes tested, it was observed that there is a relatively large increase in strength with increasing grain size in the smaller grain size region (average grain dimension from 0.0037mm to 0.0067mm) which then tends to level off at larger grain sizes. This initial increase in the strength properties with grain size is more pronounced at the lower temperatures, 1100°F to 1500°F.

Ductility as measured by the percent elongation tends to be largest for the fine grain TD-NiCr, especially at the higher temperatures as shown in Figure 60. The larger grain size materials appear to have a consistently low ductility between 0 and 5 percent at all temperatures between 1100°F and 2400°F.

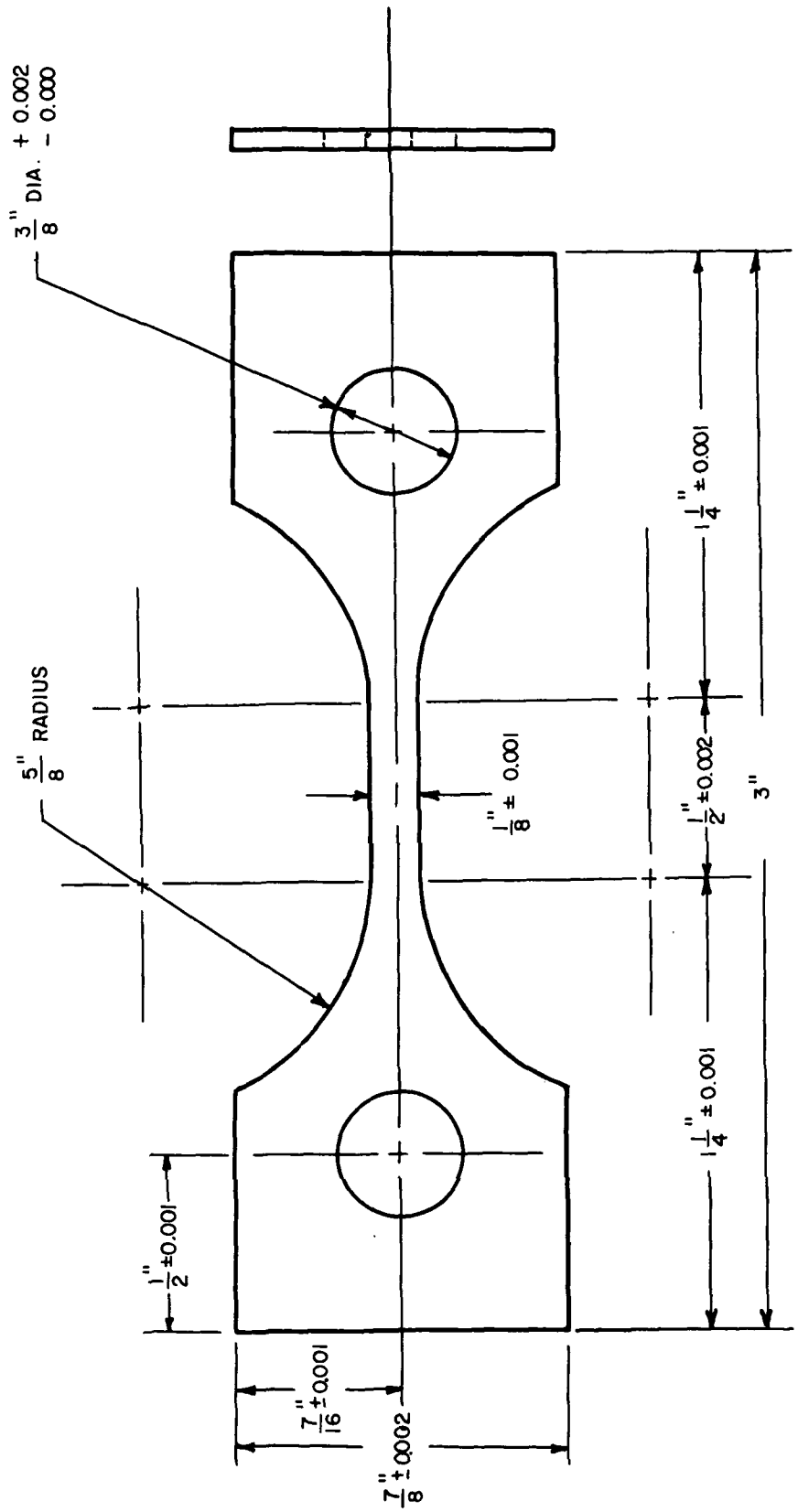

FIGURE 51: SHEET SPECIMEN GEOMETRY

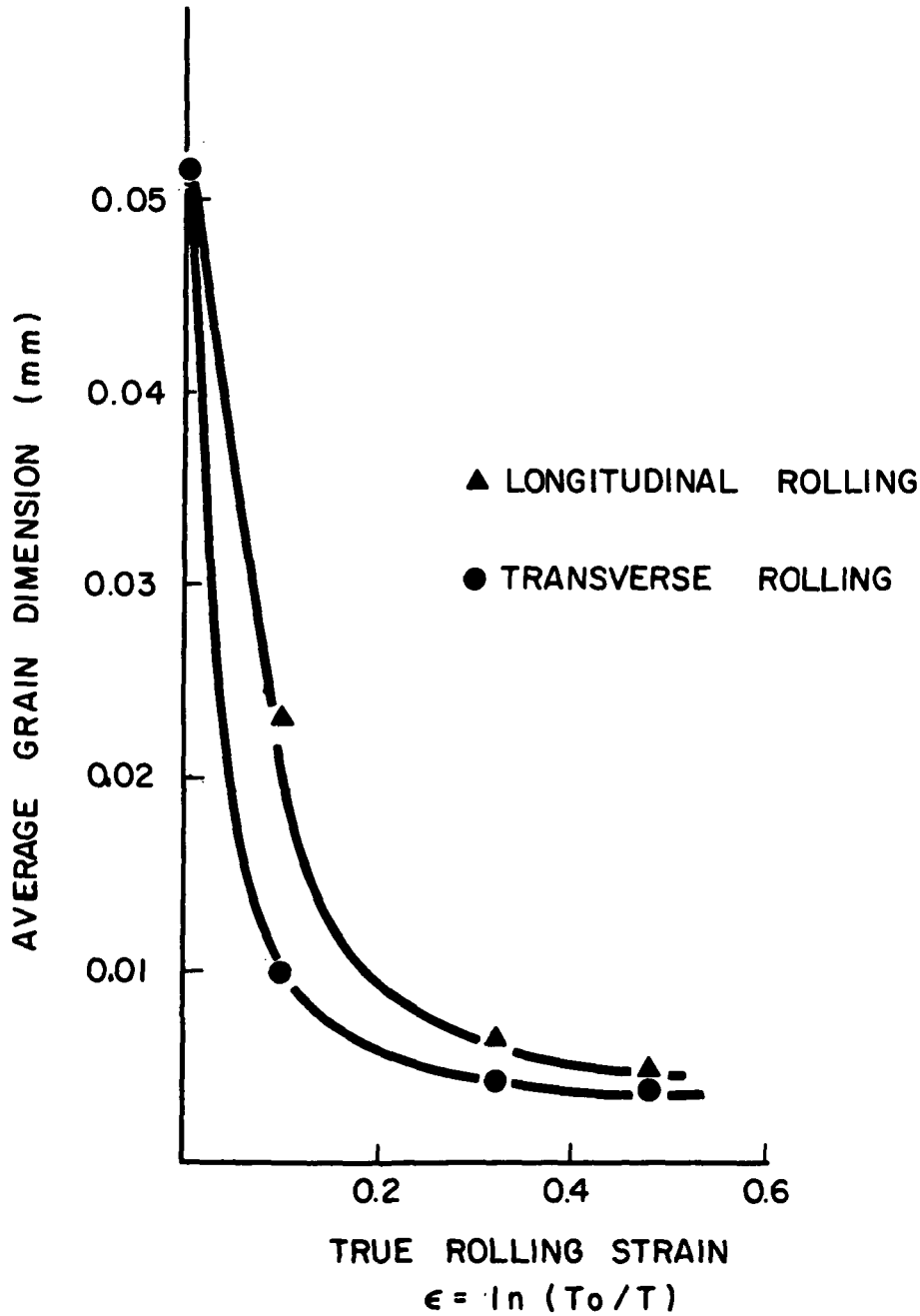

FIGURE 52: AVERAGE GRAIN DIMENSION VERSUS TRUE ROLLING STRAIN FOR ROLLING IN THE UNANNEALED CONDITION.

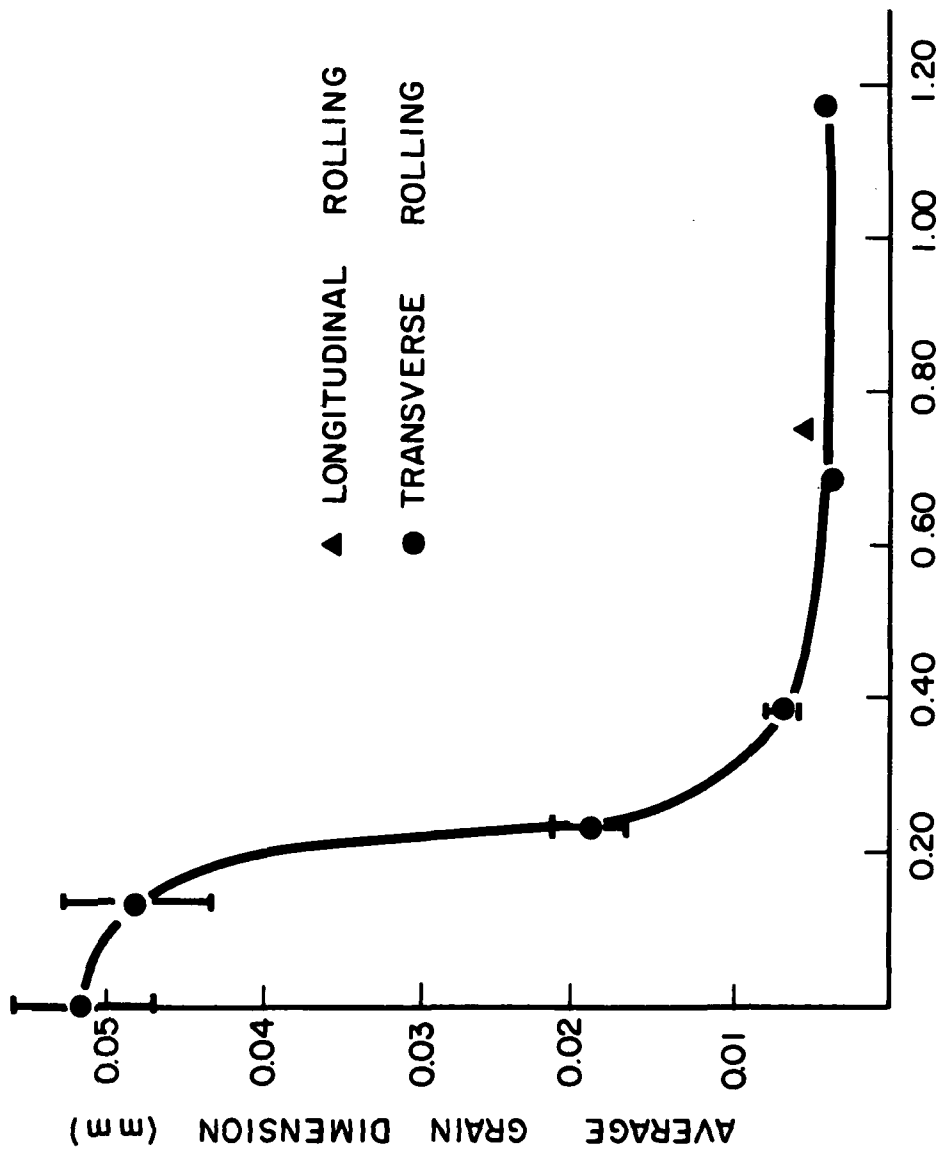

FIGURE 53: AVERAGE GRAIN DIMENSION VERSUS TRUE ROLLING STRAIN FOR ROLLING IN THE ANNEALED CONDITION.

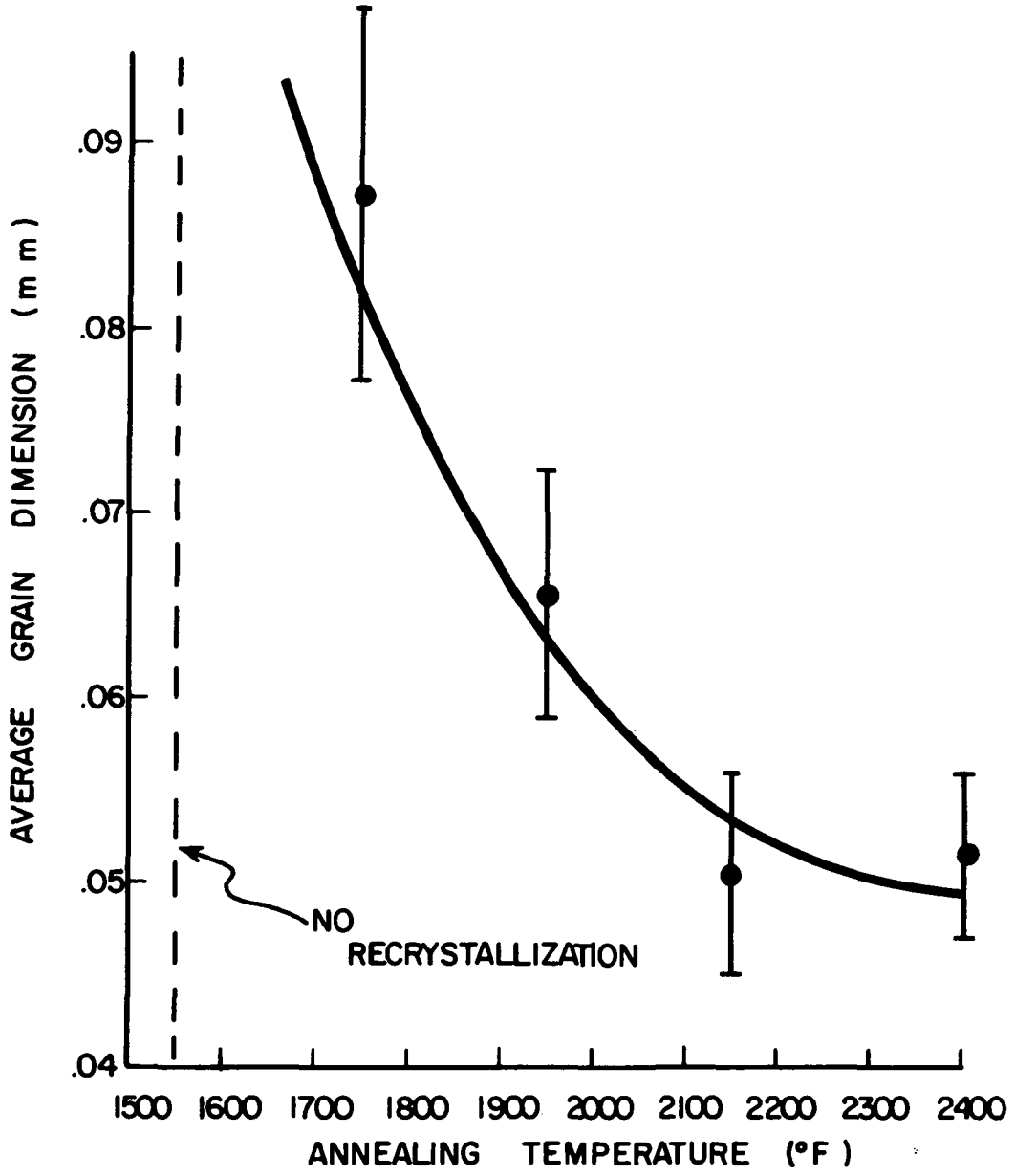

FIGURE 54: AVERAGE GRAIN DIMENSION VERSUS ANNEALING TEMPERATURE FOR THE AS-RECEIVED MATERIAL.

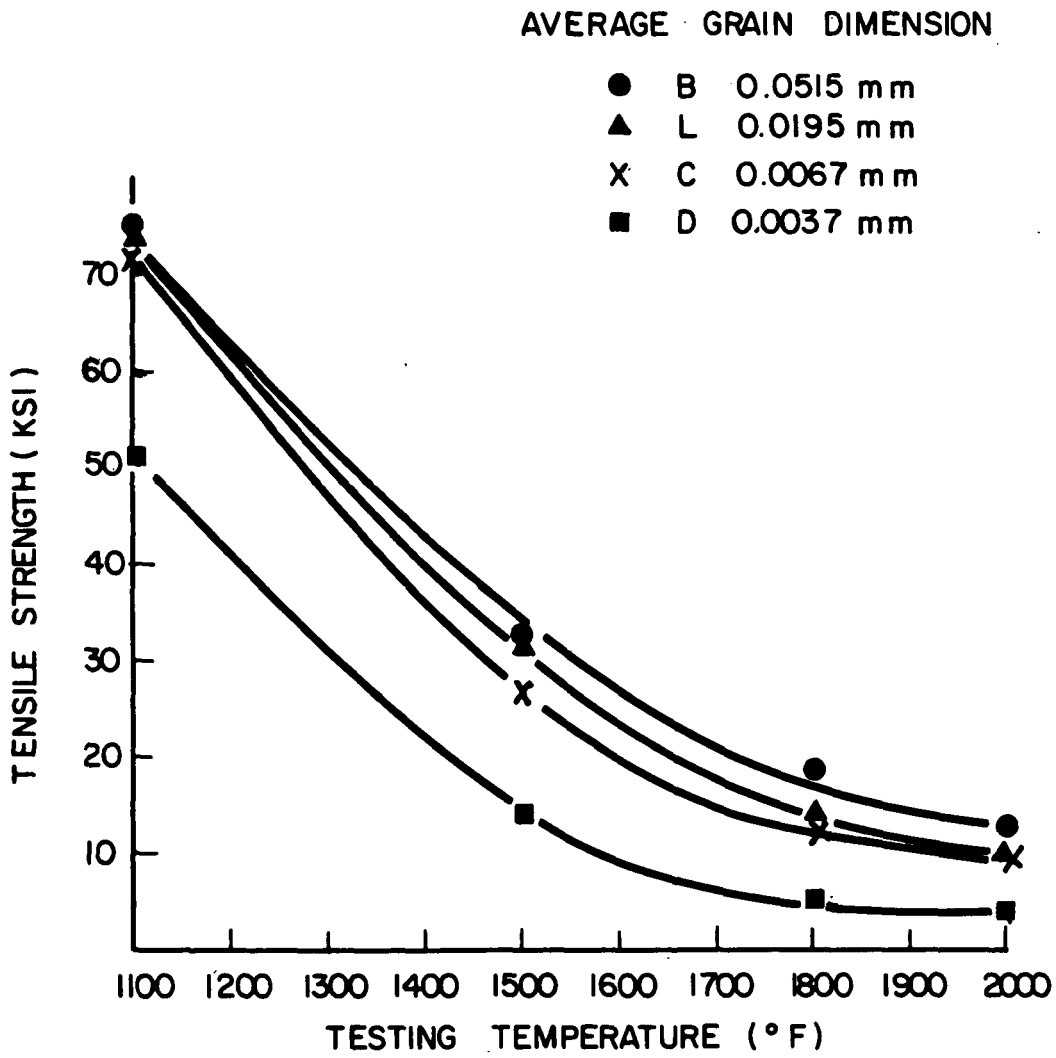

FIGURE 55: TENSILE STRENGTH VERSUS TESTING TEMPERATURE FOR VARIOUS GRAIN SIZES.

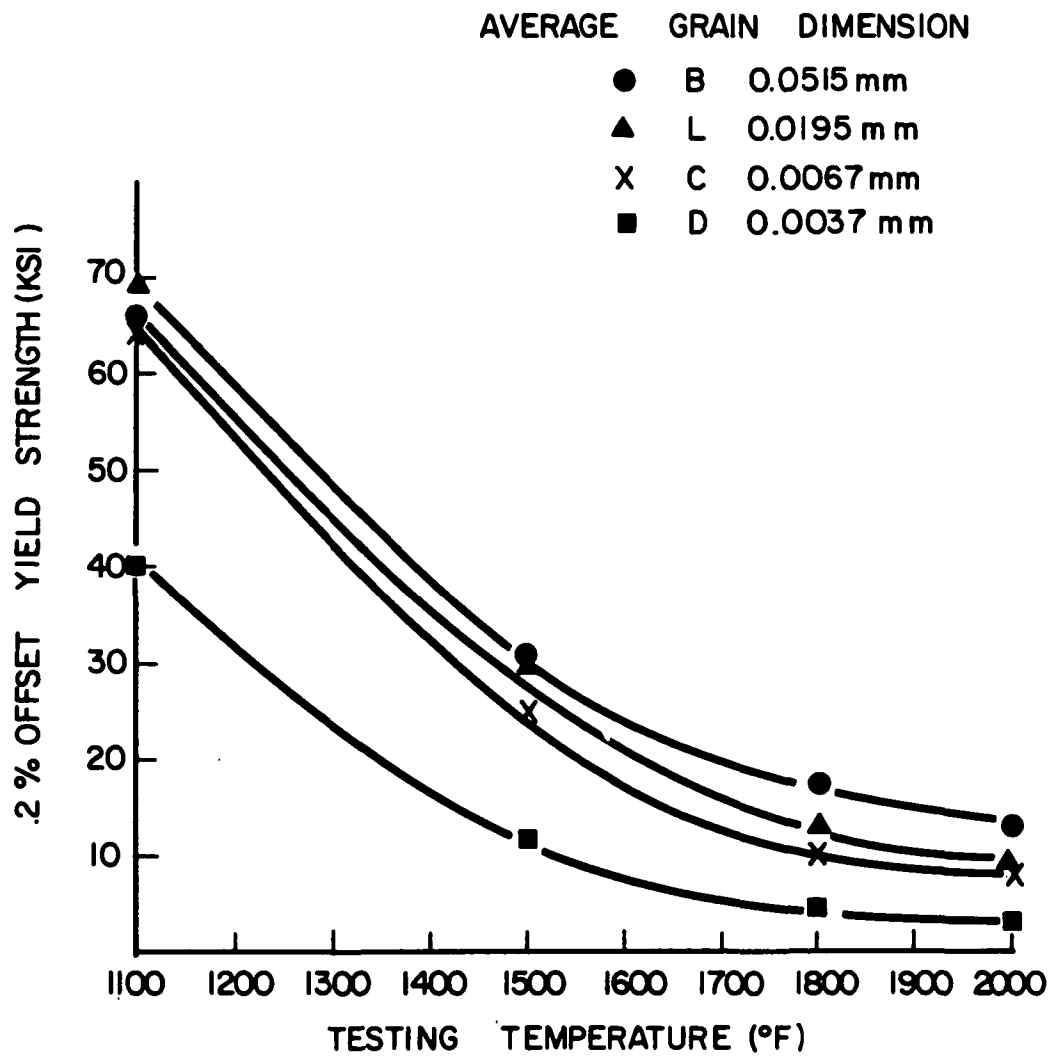

FIGURE 56: YIELD STRENGTH VERSUS TESTING TEMPERATURE FOR VARIOUS GRAIN SIZES.

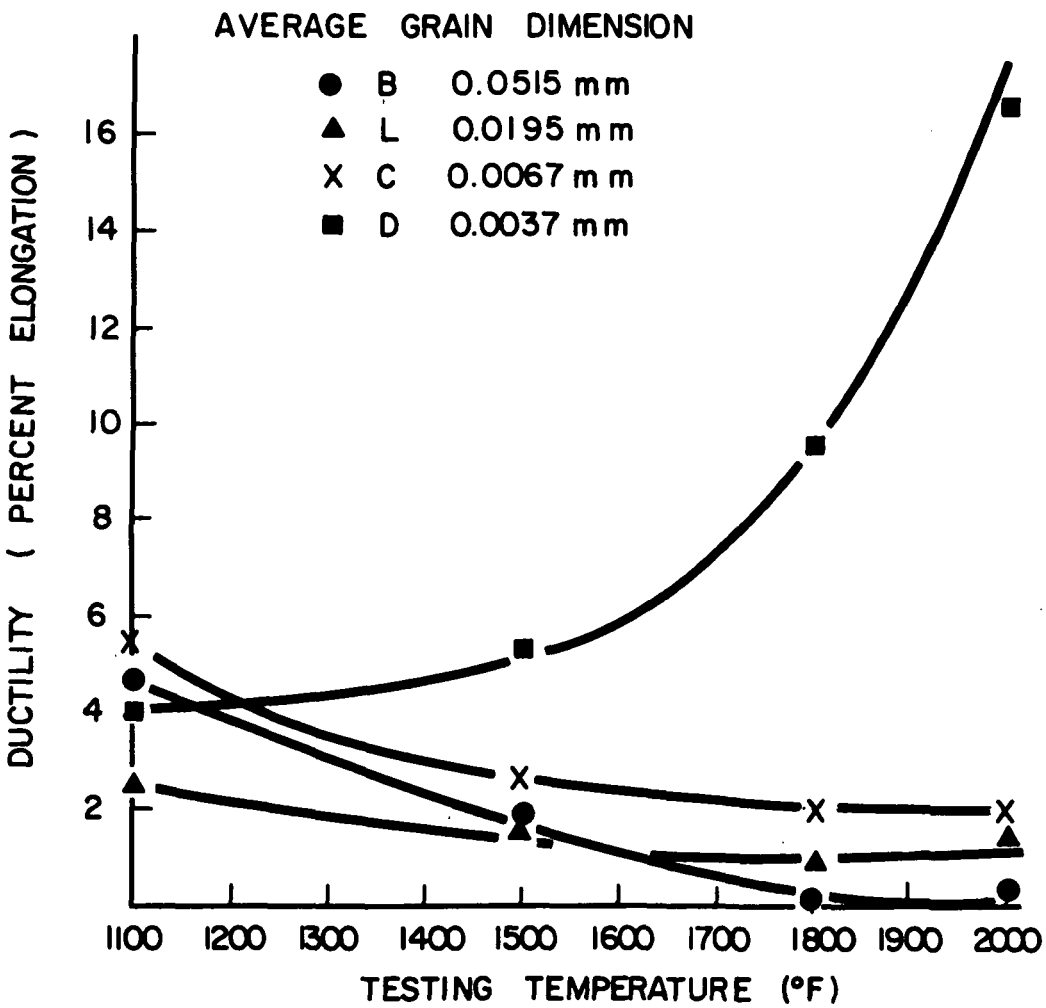

FIGURE 57: DUCTILITY VERSUS TESTING TEMPERATURE FOR VARIOUS GRAIN SIZES.

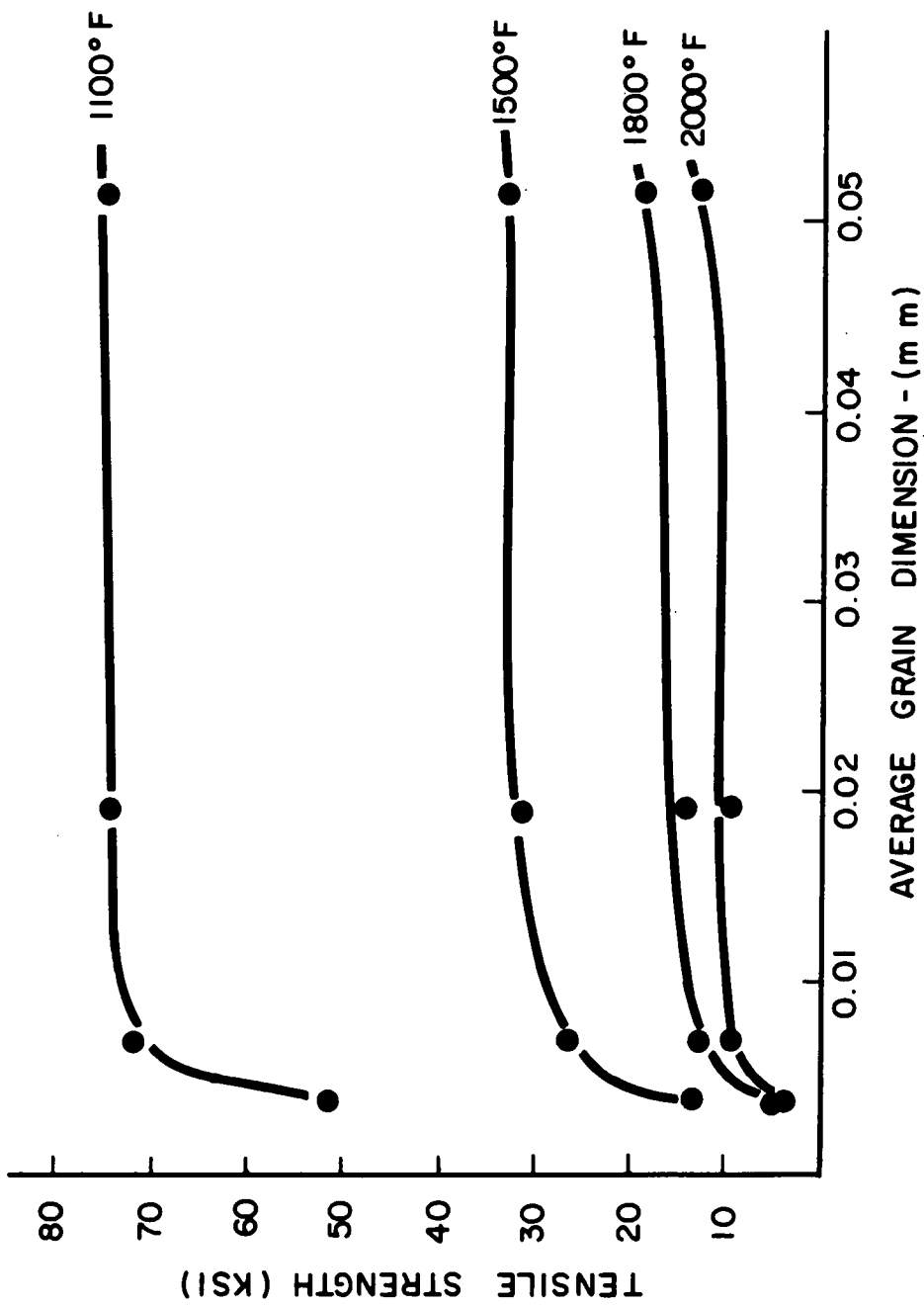

FIGURE 58: TENSILE STRENGTH VERSUS AVERAGE GRAIN DIMENSION AT VARIOUS TEMPERATURES.

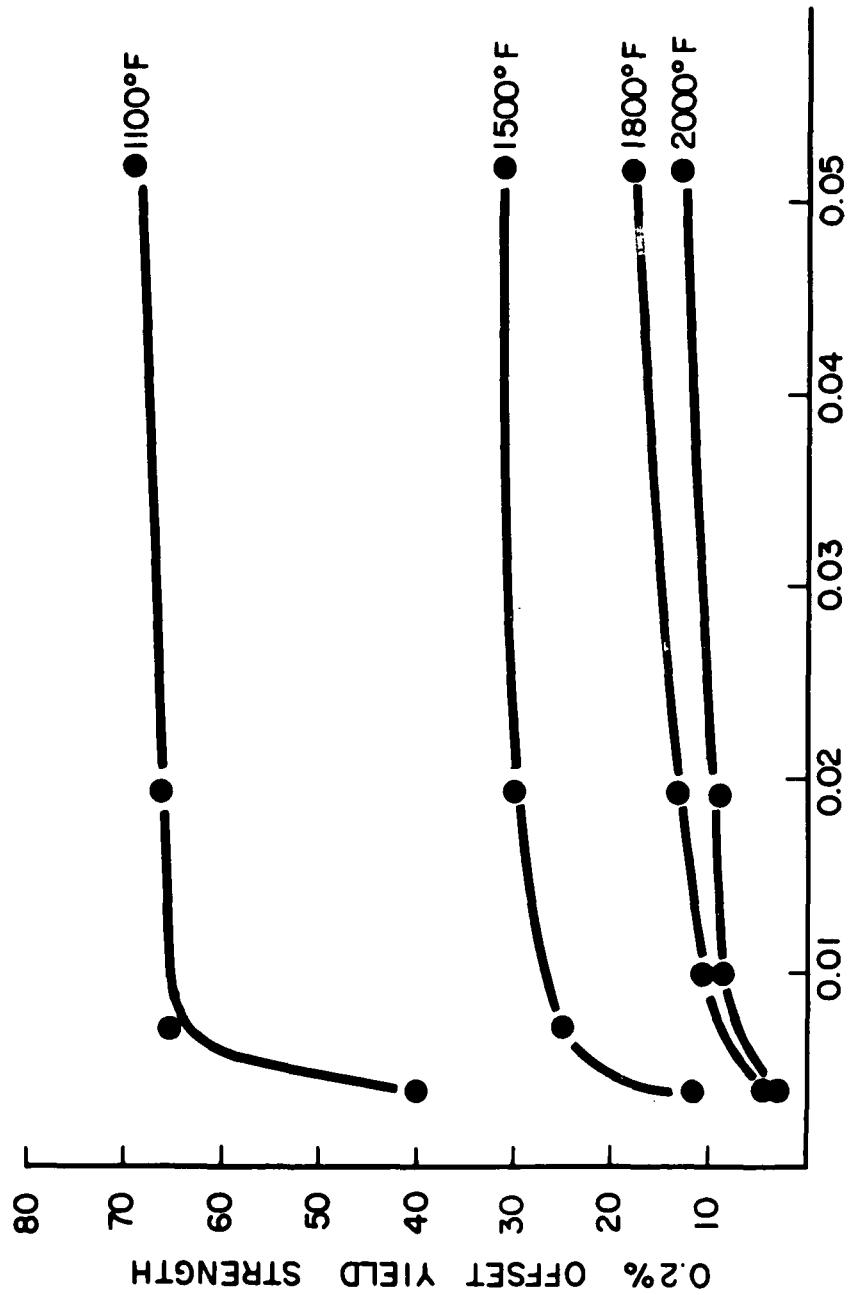

FIGURE 59: YIELD STRENGTH VERSUS AVERAGE GRAIN DIMENSION AT VARIOUS TEMPERATURES.

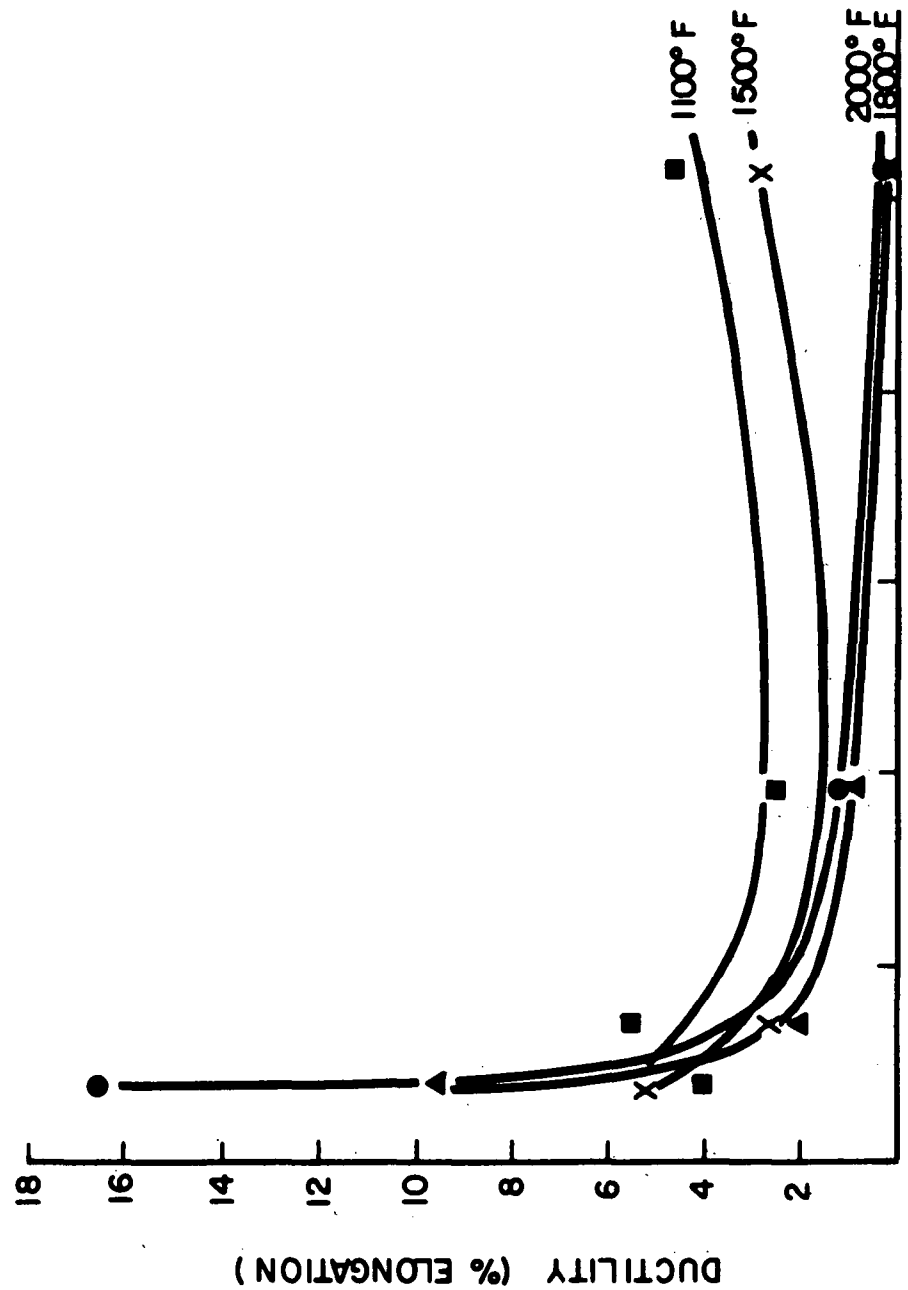

FIGURE 60: DUCTILITY VERSUS AVERAGE GRAIN DIMENSION AT VARIOUS TEMPERATURES.

SECTION III

STRESS-RUPTURE OF TD-NICKEL AT INTERMEDIATE TEMPERATURES

A very limited investigation of the stress-rupture behavior of TD-nickel was conducted at 1089°K (1500°F), to determine intermediate temperature stress-rupture properties as a function of grain size. This examination constituted the Senior Project (Spring 1972), of W.A. Johnson, an Undergraduate in the Division, and was an extension of the primary elevated temperature property investigation (Pgs. 1-172).

Experimental details were the same as outlined for the primary investigation, except that: 1) tests were run at constant load; 2) tests were run in air. Two specimen conditions, A and B, were examined (refer to Table 2, Pg. 80 for grain structure details). Tests were conducted at various stress levels, taken as fractions of the yield stress measured in tension. At 1089°K (1500°F), the yield stress for Condition A was 4.11 x 10^7 N M^{-2} (5960 psi), while the yield stress for Condition B was 11.7 x 10^7 N M^{-2} (16,900 psi). Specimen strain as well as time to rupture were recorded.

Strain-time curves for Conditions A and B are shown in Figures 61 and 62, respectively. Strain rates decreased with decreasing stress. Stress-rupture behavior is indicated in Figure 63. The 100 hour rupture

stress of Condition B was significantly greater than that of Condition A. Thus, at 1089°K (1500°F) stress-rupture properties improve with increasing grain size.

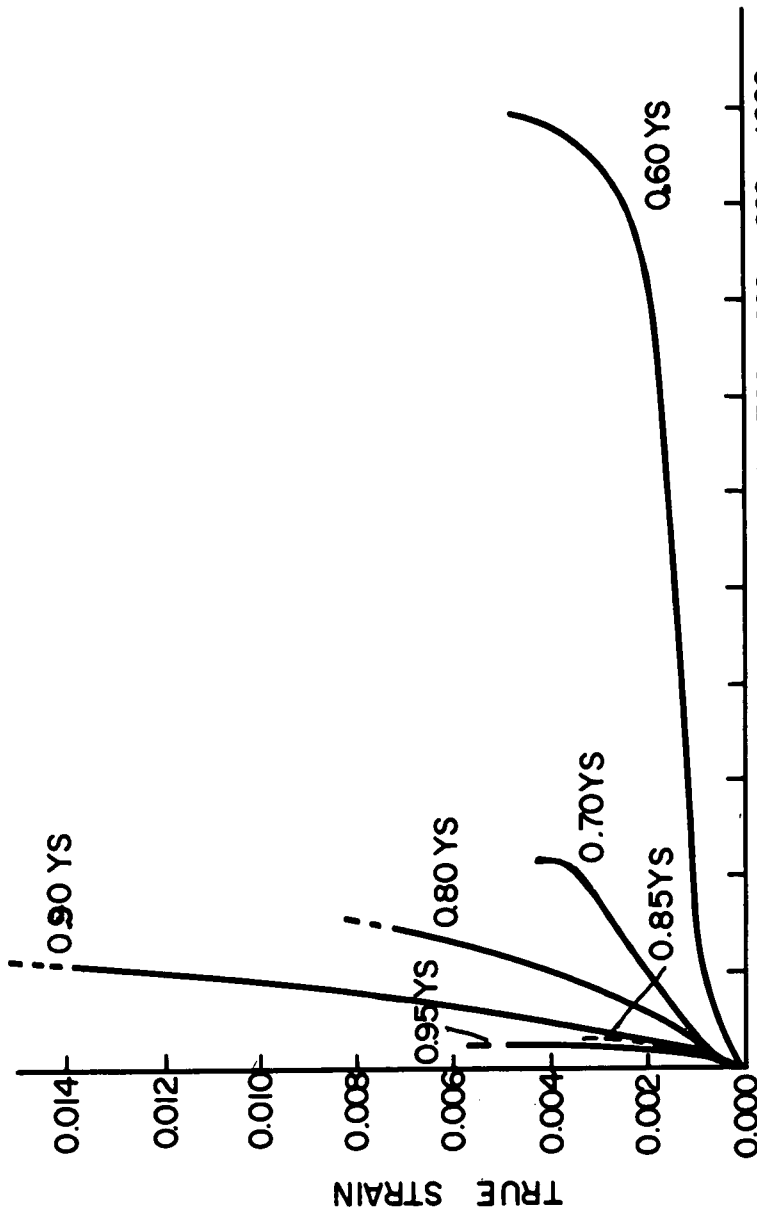

FIGURE 61: TRUE STRAIN-TIME CURVES FOR CONDITION A AT 1089°K (1500°F).

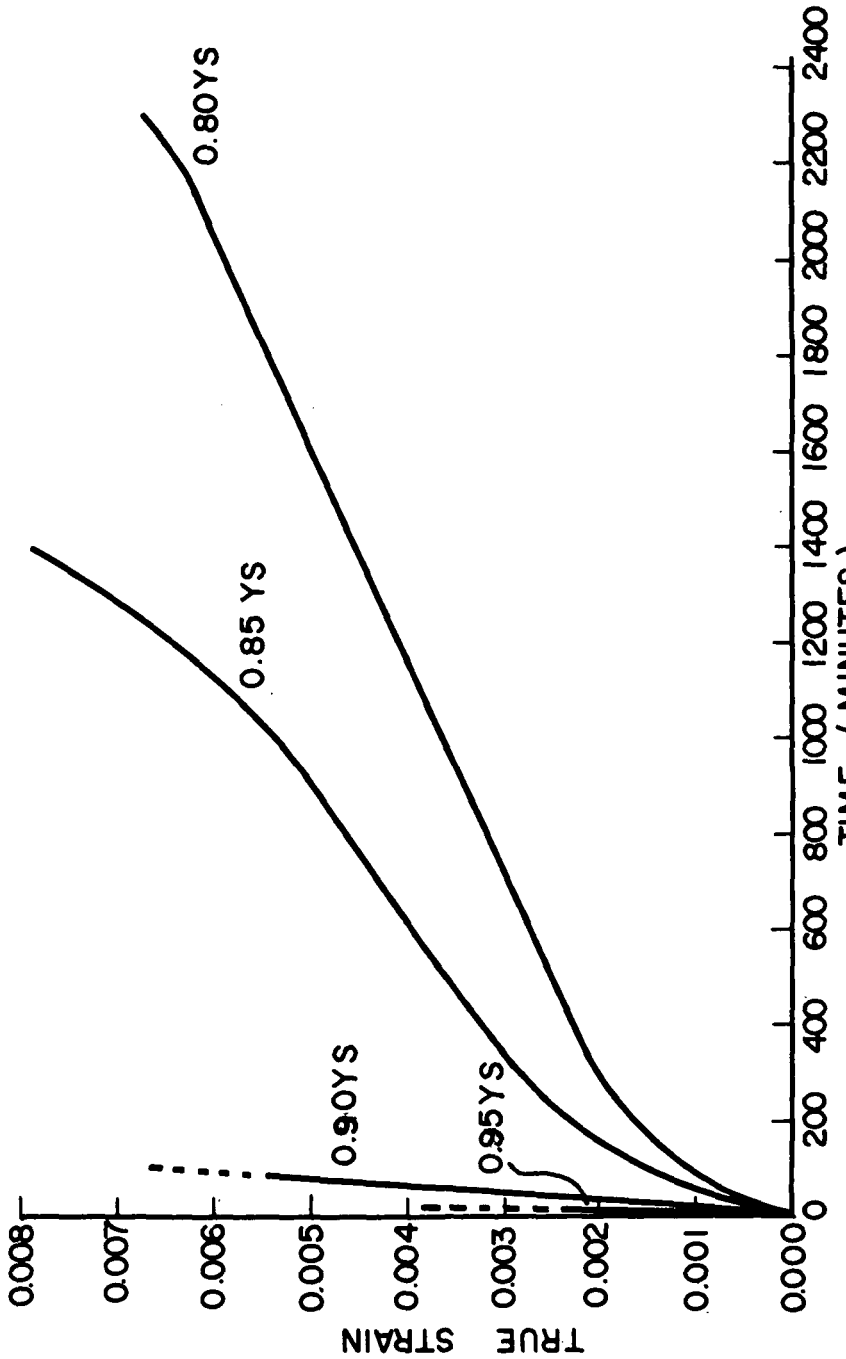

FIGURE 62: TRUE STRAIN-TIME CURVES FOR CONDITION B AT 1089°F (1500°F).

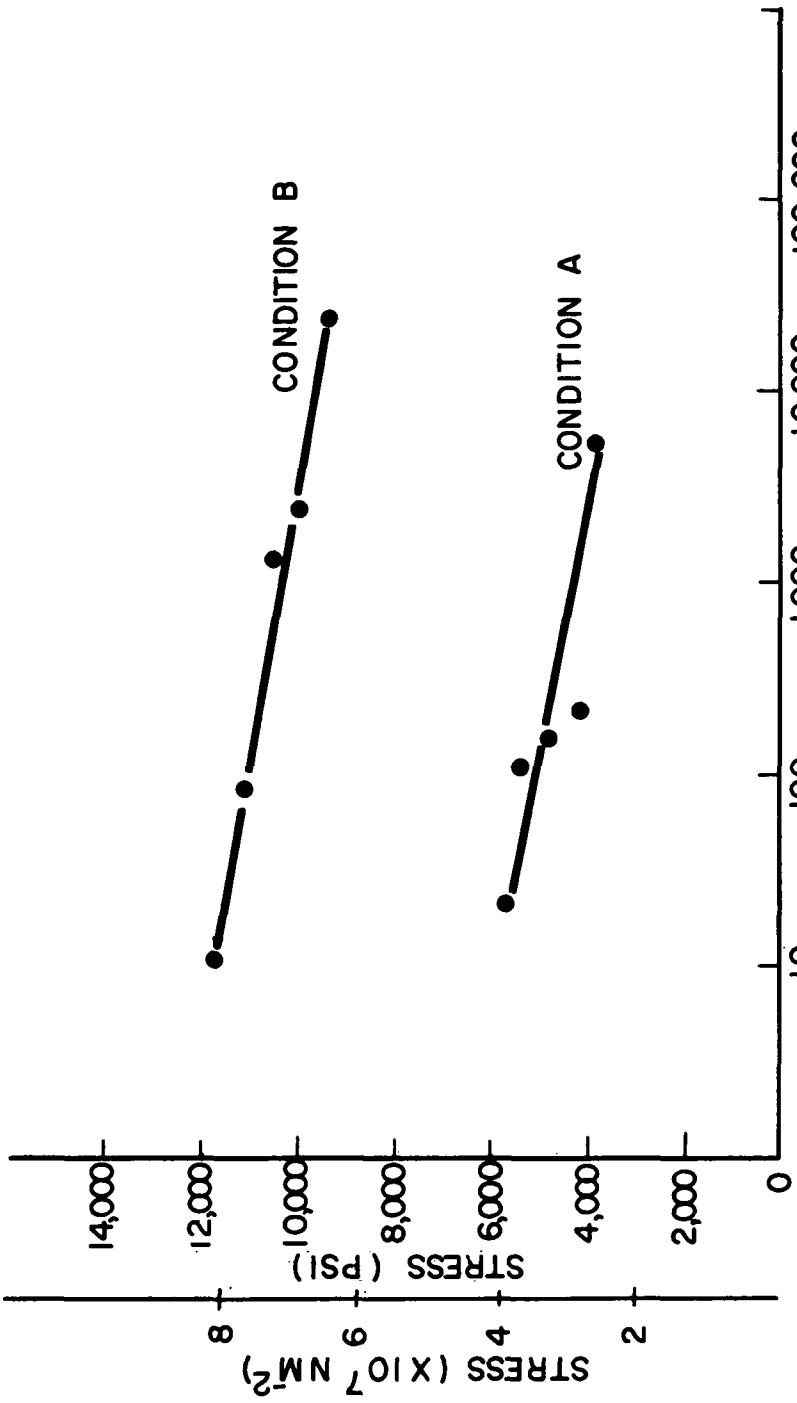

FIGURE 63: STRESS-RUPTURE PLOTS FOR CONDITIONS A AND B AT 1089°K (1500°F).

SECTION IV

TEXTURE STUDY ON TD-NICKEL AND TD-NICKEL CHROMIUM

The annealing textures of various grain sizes of TD-nickel bar starting material and TD-nickel chromium (TD-NiCr) sheet material were determined by combination X-ray transmission and back-reflection methods. This technique using existing x-ray facilities, was incorporated by R.D. Kane during the summer of 1970 as part of an undergraduate research program sponsored by the National Science Foundation. The textures of the TD-nickel and TD-NiCr materials were determined as a function of the rolling and annealing operations used to produce the various grain sizes. The texture determinations on the TD-nickel bar material constituted the Senior Project of R.D. Kane (Spring 1971). The TD-NiCr material was investigated by P.L. Flynn (Spring 1972) also in fulfillment of his Senior Project.

The three material states of TD-nickel examined were:

1) The as-received, as-extruded bar material, grain size 0.001mm.
2) The as-extruded material rolled 33% transverse to the original bar axis, and annealed 1 hour at 2400°F in argon, grain size 0.4mm.
3) Material state 2 followed by continued trans-

verse rolling to a reduction of 79% and annealed 1 hour at 2400°F in argon, grain size 0.02mm.

The pole figures for these grain states of TD-nickel are shown in Figure 64 through 66. The diffracted x-ray intensity from the (111) planes was used in both transmission and back-reflection. In transmission the first order reflections were monitored in order to determine the outer region (0°-55°) of the pole figure. The inner portion (60°-90°) was determined by monitoring the second order (111) reflections in back-reflection.

TD-NiCr was also examined in three material states:

1) The as-received, 0.1 inch sheet material annealed 1 hour at 2400°F in argon, grain size 0.0515mm.
2) The as-received sheet material, rolled 28% transverse to the original rolling direction, annealed 1 hour at 2400°F in argon, grain size 0.0067mm.
3) The as-received sheet material, rolled 48% in the transverse direction, annealed 1 hour at 2400°F in argon, grain size 0.0037mm.

The (111) pole figures for these grain states of TD-NiCr are shown in Figures 67 through 69. These pole

figures were determined by the same technique discussed previously for the TD-nickel bar material.

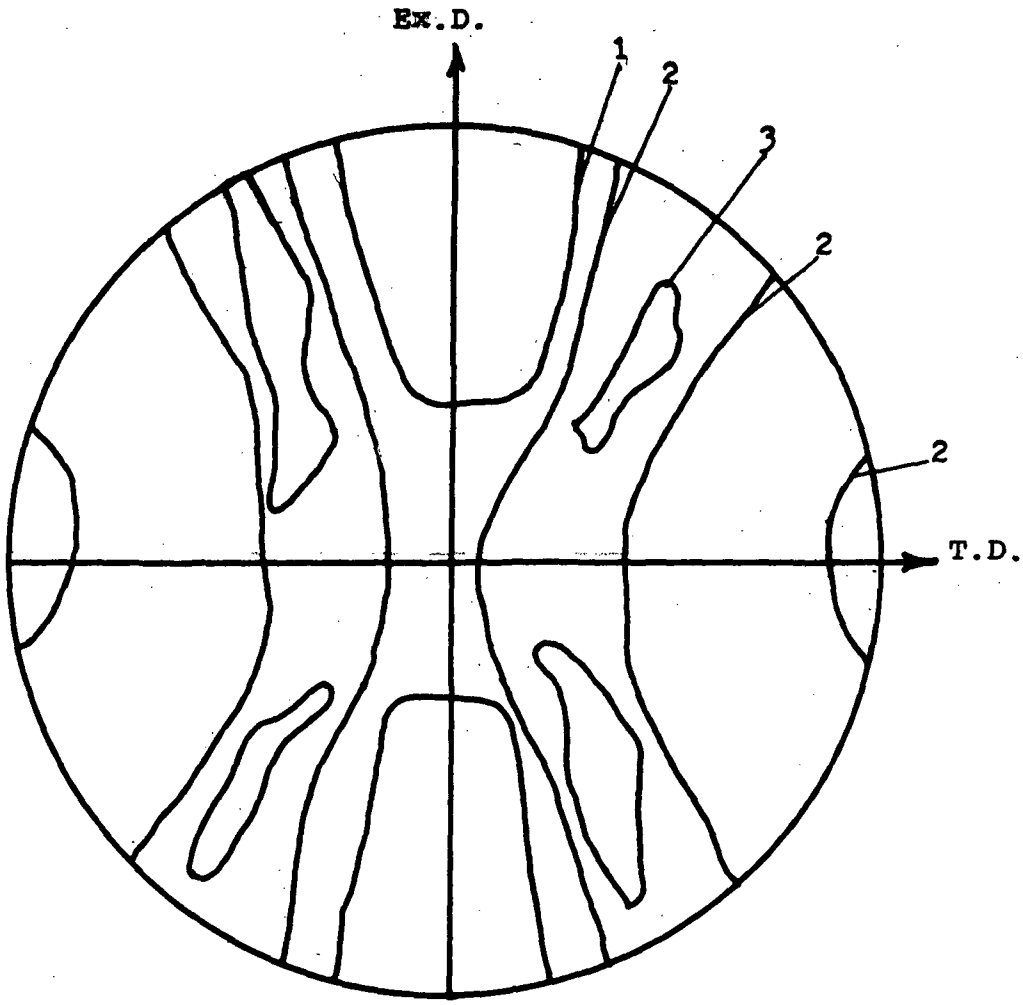

FIGURE 64: (111) POLE FIGURE FOR AS-RECEIVED, AS-EXTRUDED TD-NICKEL; GRAIN SIZE 0.001mm.

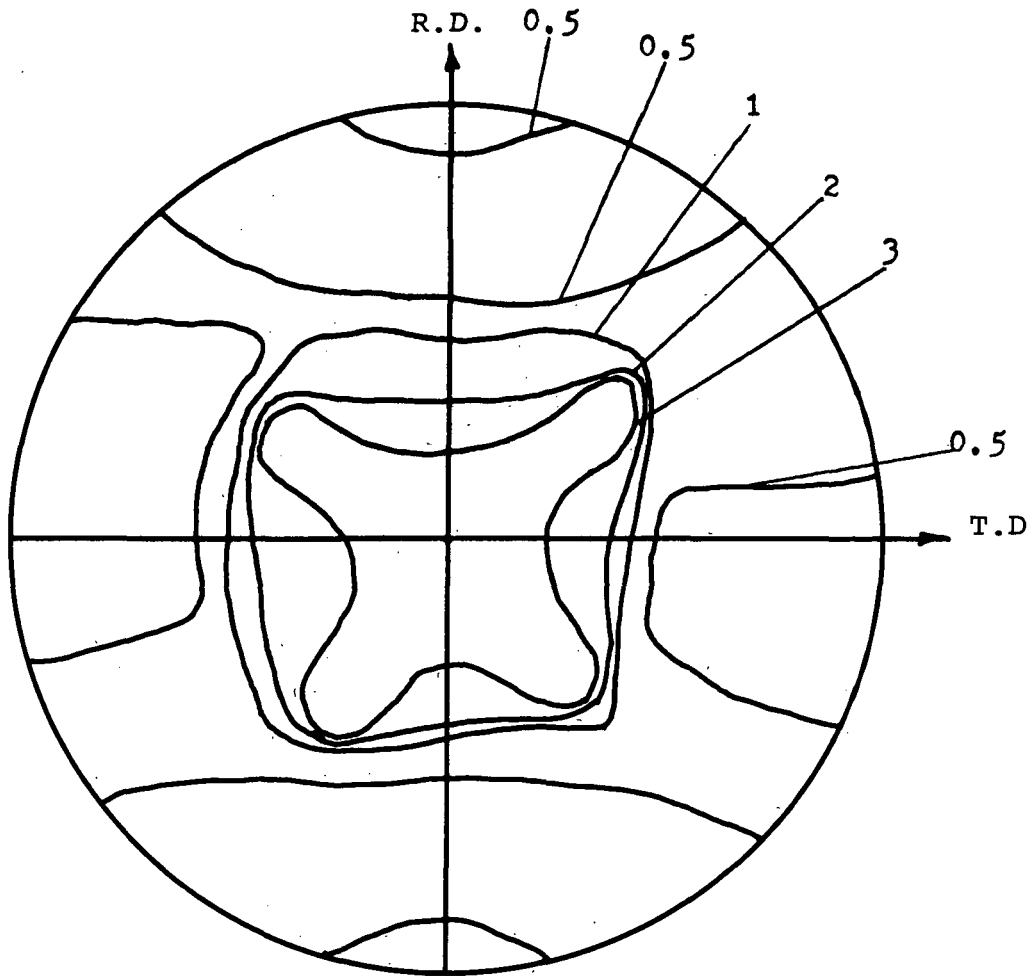

FIGURE 65: (111) POLE FIGURE FOR AS-EXTRUDED TD-NICKEL ANNEALED 1 HOUR AT 2400°F, ROLLED TRANSVERSE 33% AND ANNEALED 1 HOUR AT 2400°F; GRAIN SIZE 0.4mm.

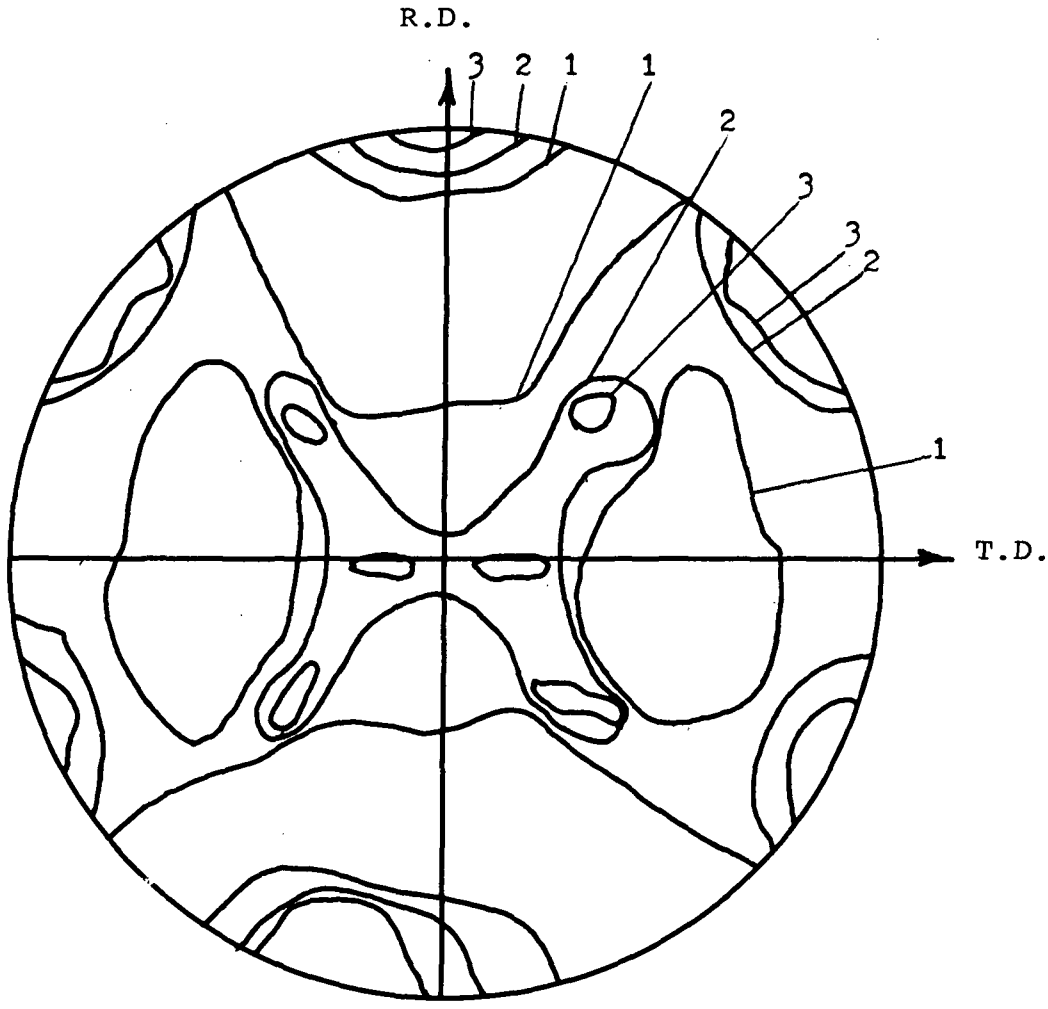

FIGURE 66: (111) POLE FIGURE FOR AS-EXTRUDED TD-NICKEL ANNEALED 1 HOUR 2400°F, TRANSVERSE ROLLED 33% ANNEALED 1 HOUR 2400°F, CONTINUED TRANSVERSE ROLLING 79%, ANNEALED 1 HOUR 2400°F; GRAIN SIZE 0.02mm.

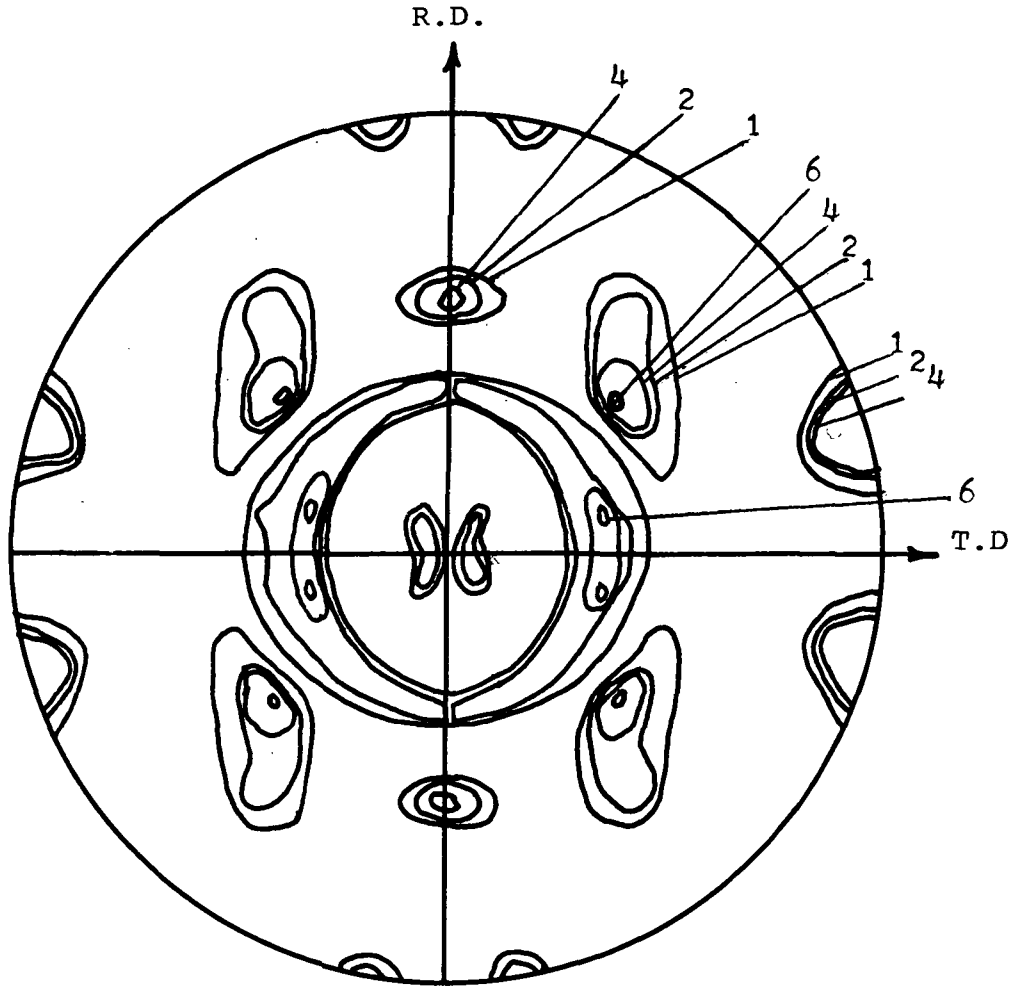

FIGURE 67: (111) POLE FIGURE FOR TD-NiCr 0.1 INCH SHEET ANNEALED 1 HOUR AT 2400°F, GRAIN SIZE 0.0515mm.

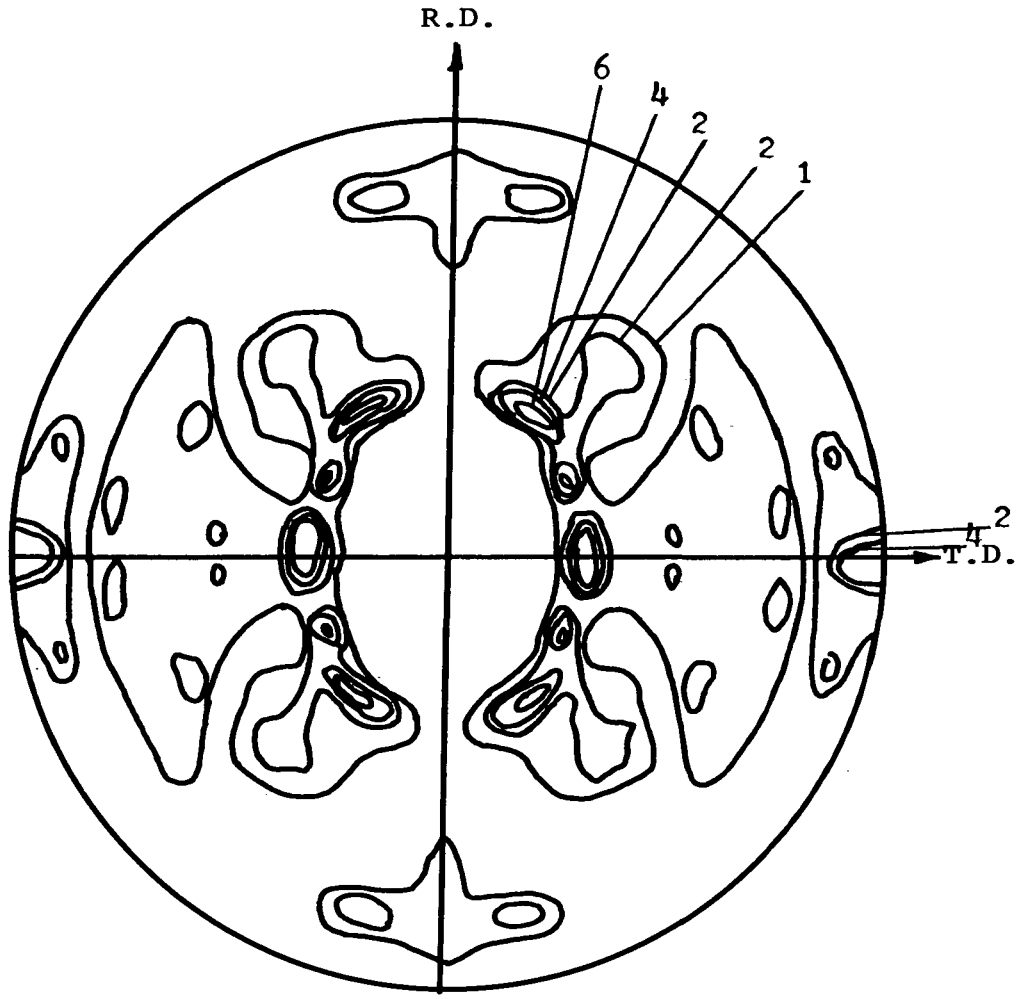

FIGURE 68: (111) POLE FIGURE FOR TD-NiCr 0.1 INCH SHEET, ANNEALED 1 HOUR 2400°F, TRANSVERSE ROLLED 28%, ANNEALED 1 HOUR 2400°F; GRAIN SIZE 0.0067mm.

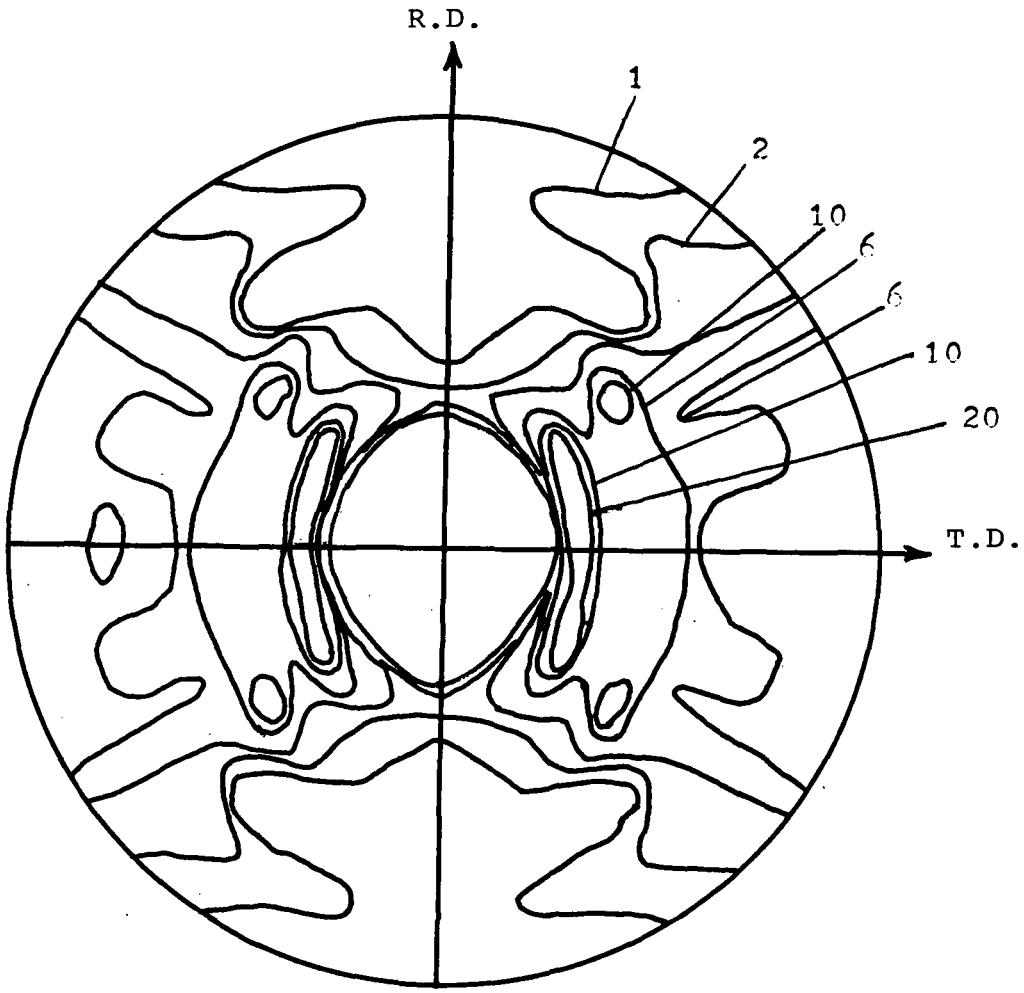

FIGURE 69; (111) POLE FIGURE FOR TD-NiCr 0.1 INCH SHEET ANNEALED 1 HOUR AT 2400°F, TRANSVERSE ROLLED 28%, ANNEALED 1 HOUR AT 2400°F; GRAIN SIZE 0.0037mm.